Resonant Two Proton Decay From $^{14}O^{*}$ Using A Radioactive Beam

Carlos Bain

Thesis submitted for the degree of Doctor of Philosophy

Department of Physics and Astronomy

University of Edinburgh

1995

Abstract

Two experiments were carried out to search for and identify the mechanism for two proton emission from the 7.77 MeV ($J^{\pi} = 2^{+}$, $\Gamma = 76 \pm 10$ keV) excited state in ^{14}O. The experiments were performed at the Radioactive Ion Beams Facility at Louvain-la-Neuve, in Belgium, using a 45 MeV beam of radioactive $^{13}N^{3+}$ ions on a $[CH_2]_n$ target to populate the state. The protons and other particles were detected using the Louvain-Edinburgh Detector Array, LEDA, a large area annular silicon strip detector. Control experiments with a ^{12}C target and with a degraded beam energy were also made.

Proton-proton coincidence measurements made in the commissioning run identified a two proton decay component. However, the large background ($\sim$90%) caused by evaporation protons from the fusion of ^{13}N with ^{12}C prevented an analysis of the decay mechanism.

The follow up experiment utilised two LEDA detectors whereby the protons of interest would be stopped in the front detector with the back detector acting as a veto for high energy protons. Comparison of data with simulations for the decay mechanisms revealed the decay to be dominantly a sequential emission of two protons via the 2.37 MeV ($J^{\pi} = 1/2^{+}$, $\Gamma = 33.7 \pm 0.9$ keV) state in ^{13}N to the ground state in ^{12}C. This decay mode has a measured partial width of 125$\pm$20 eV which represents a 0.16% branching ratio. Theoretical predictions for this value give a width of 3 ± 1 keV which gives a spectroscopic factor of $\theta^2 = 0.04$. Simulations using a model for ^{2}He or diproton emission have resulted in an upper limit of 5% being set which corresponds to $\sim$ 6 eV (95% confidence limit). Calculation for this width with a spectroscopic factor of unity give a value of 15$\pm$5 eV. Hence an upper limit for the spectroscopic factor of $\theta^2 = 0.4$ can be set which is above the value of 0.22 predicted by B.A. Brown.

Declaration

The experiments described in this thesis were carried out by myself and fellow collaborators. The data analysis and interpretation is my own work and this thesis has been written by myself.

Carlos Bain

Acknowledgements

Firstly my deepest thanks go to my supervisor, Phil Woods, for the motivation he has given over the last three years and for the enthusiasm he has shown in this project. Special thanks to Tom Davinson for all the help he has given and to my second supervisor, Alan Shotter, for his continuous support. Thanks also go to all the members of the Edinburgh Nuclear Physics group.

All the people in Belgium - Wilfried Galster, Pierre Leleux, Jean Vervier, Mark Huyse, Geert Vancraeynest, Alain Ninane, Patrick Decrock, Romuald Coszach, Carinne Michotte, Csaba Sükösd, Ils Reusen, Nico Coulier and Sonja Ternier for making me feel welcome in Louvain and making the time spent there enjoyable.

Also thanks to Robert Kryger, Alex Brown, Irena Stone, Ian Thompson, Boris Danilin and Ray Satchler for help in solving some of the theory problems that this experiment has conjured up.

The Department of Education of Northern Ireland (DENI) are specially thanked for funding this PhD course.

Thanks go to my fellow PhD students Doug, Jim, the Richards, Aamer and John who have all brought a smile into work and made the days fly by. Also Andreas Schölze for his work on the UNIMONTE code.

Big thanks to all my flatmates, ex-flatmates and other great pals.

An immeasurable amount of thanks go to my parents for all that they have done to help me over the last years. Big thanks go to my brother Mike, who is also writing a big book but has managed to make his funnier than mine.

I reserve my final thanks to Julie for all the support she has given me.

Contents

List of Figures

Chapter 1

Introduction

The most common technique used in nuclear physics research for studying reaction mechanisms or of producing exotic nuclei consists in bombarding stable targets by beams of stable ions. New domains were opened thirty years ago by developing the use of radioactive targets. Over the last decade one of the main advances in experimental nuclear physics has been the development of Radioactive Ion Beams (RIB). The study of physics with RIB has blossomed into a major research area in a very short time.

Two methods can be used to produce a RIB.
The first involves a single accelerator whose primary stable beam bombards a target to produce a secondary radioactive beam. One of these secondary beams is separated from the primary and from other secondaries to produce a RIB. This method has been used with both high energy primary beams which are fragmented by their interaction with suitable targets [Bim85] and lower energy primary beams which experience transfer reactions on targets [Bec90]. The former generally yields energies up to 100 MeV/nucleon with high intensities and the latter energies of a few MeV/nucleon with lower intensities.
The second method uses two accelerators. Beams from the first accelerator yield large quantities of the radioactive atoms of interest by a suitable nuclear reaction.

These are extracted from the target, ionised and accelerated to the desired energy by the second accelerator.
The two methods supplement each other in the scope of physics that can be done with them, but in the energy range around the Coulomb barrier the second type is superior in intensity and energy resolution. The advantages and disadvantages are described in geater detail in [Nup93].

The Acceleration of Radioactive Elements for Nuclear, Astrophysical and Solid-State Studies, ARENAS[3], facility in Louvain-la-Neuve was the first to employ this second technique of using two cyclotrons [Dar90]. The facility was developed initially to study the important astrophysical reaction rate ^{13}N(p,γ) ^{14}O [Dec93] but its characteristics have recently been extended to allow production of other beams and the study of other reactions. A description of the facility and details of available beams is given in section 3.1.

The table of isotopes reveals that there are $\sim$ 270 isotopes which are found in nature. In total, about 3000 radioactive nuclei have been synthesised in the laboratory for study. Theorists have predicted that around 6000 nuclei exist with $t_{1/2}$ >1ms [Boy94] and the use of RIB's means more of these nuclei can be accessed and have their properties studied.

A major achievement in the study of nuclei far from stability has been the observation of many new radioactive decay modes. Isotopes close to the valley of stability tend to decay by β-emission, which is energetically allowed for small differences in the binding energies of parent and daughter nuclei. Moving out towards the drip-lines other decay modes can become dominant. Initially β-delayed particle emission will occur. This is a two step process where a slow β-decay populates an excited state in the daughter nucleus which then decays by the rapid emission of one or more nucleons.

On the neutron-rich side of stability, towards the neutron drip line, decays of neutron unbound nuclei are predicted to take place on the time scale of the strong

interaction ($< 10^{-22}$ s) and for this reason and the inaccessibility of the neutron drip-line direct neutron decay has not been observed to date. Cases of $\beta 2n$ and $\beta 3n$ have been observed in ^{11}Li, (these are described in more detail in a review by P.G. Hansen and B. Jonson [Han89]).

The proton-rich side has proven to be an excellent source of exotic decay modes due to the emission of charged particles being hindered by the centrifugal and Coulomb barriers. These decays can occur with half-lives long enough to allow detection ($\leq 1\mu$s). Experiments concentrating on drip-line nuclei have been successful in measuring direct proton decay in an extensive range of nuclei up to ^{185}Bi [Dad95]. Other decay modes which have been observed are βp, $\beta 2p$ and $\beta 3p$. A summary of these experiments is given in section 1.2.2. A comprehensive overview of the field can be found in a review article by A.C. Mueller and B.M. Sherrill [Mue93].

Another exotic decay mode for proton-rich nuclei is that of ground state two proton emission, referred to as diproton or ^{2}He emission, predicted 35 years ago by Goldansky [Gol60]. Heavy nuclei which would exhibit this decay mode are inaccessible at present because of the pairing energy of the last two protons and the increased Coulomb barrier (double that seen by a proton). Thus, all experimental activity has concentrated on light nuclei in the mass region $A < 40$. A summary of these experiments is given in section 1.2.1. No convincing evidence as yet exists for the observation of diproton emission and the continued activity in this field is based primarily on the information that it will provide on the correlation between the two protons in the nucleus.

This thesis project presents a unique experiment which looked at two proton emission from ^{14}O* using a radioactive ion beam and the Louvain-Edinburgh Detector Array (LEDA). There a number of possible decay mechanisms for the emission of the two protons of which ^{2}He emission is one. These are discussed in the following section.

1.1 Phenomenon of two proton emission

Emission of two protons can proceed by means of several processes:

(a) Emission of two protons in a relative $^1S_0$ configuration which is referred to as ^{2}He or diproton emission;

(b) sequential emission via an intermediate state;

(c) uncoupled simultaneous emission.

These are shown graphically in figure 1.1 and the decay scheme in figure 1.2 shows the case for emission from an excited state in the parent nucleus. The parent nucleus is designated as having a mass A, the intermediate state for sequential $A-1$ and the final two proton daughter $A-2$.

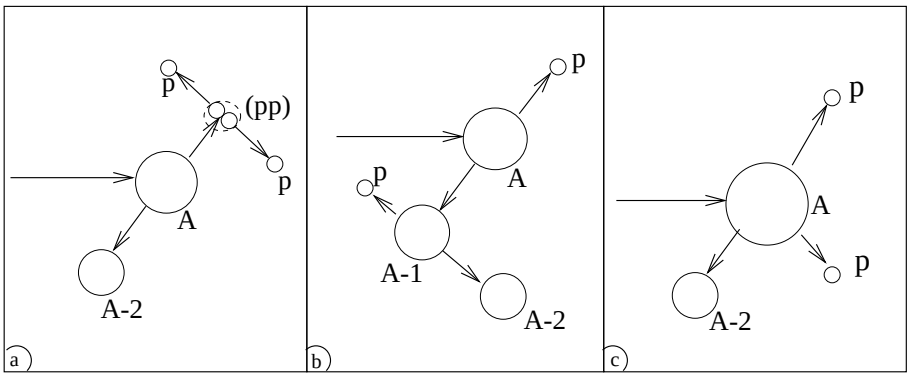

Figure 1.1: *The three possible decay mechanisms for two proton emission: (a)emission of the diproton, (b)sequential emission and (c)uncoupled simultaneous emission.*

The theoretical model for ^{2}He emission is discussed in chapter 2. The diproton sits in the potential well of the two proton daughter nucleus. Not all the energy available to the two protons is kinetic since a fraction is converted into the mass of the ^{2}He. If the ^{2}He penetrates the combined Coulomb and centrifugal barrier it breaks up into two protons with the ^{2}He mass converted into the proton-proton relative energy. Observation of ^{2}He emission would result in strong angular correlation at small relative opening angles.

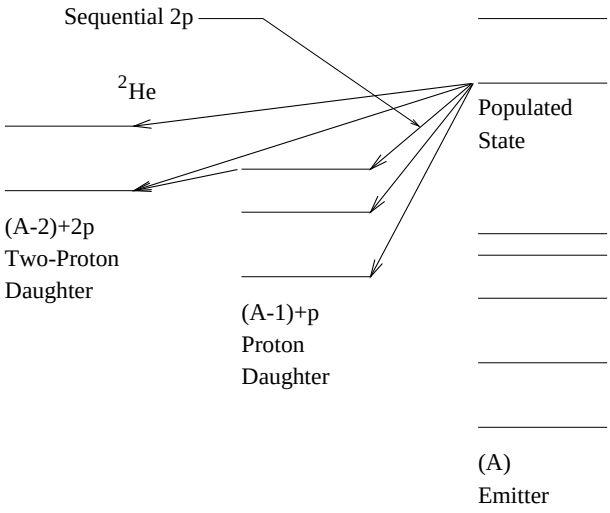

Figure 1.2: *Decay scheme highlighting cases(a) and (b). An excited state in the parent nucleus is populated and this then emits two protons.*

The sequential emission of two protons via an intermediate state in the one proton daughter would restrict the individual energy distribution of the two protons and thus, a strong energy correlation would be expected.

Simultaneous two proton emission occurs when the two protons leave the nucleus independently with a time between the first and second emission which is so small that an intermediate state is not formed. Observation of this mechanism would result in an isotropic angular distribution and an energy continuum.

1.2 Previous experiments

The study of two proton emission is a relatively virgin field which has produced a limited number of experiments and results. This section is intended as a review of this work. The following summary has been divided into two parts. The first part discuses experiments where solely ground state two proton emission was investigated. The second part contains the cases of β-delayed two proton emission which have been observed.

1.2.1 Ground state two proton emission

Goldansky predicted the existence of ground state two proton emission in particle unbound (proton rich), even Z, light nuclei where the pairing energy between the last two protons causes the one proton decay channel to be energetically forbidden [Gol60]. Goldansky, and later, Jänecke [Jän65] suggested a list of candidates which could decay by this mode. The list included ^{6}Be, ^{8}C, ^{12}O and ^{16}Ne. The widths of the ground states are very large and are therefore expected to decay very rapidly ($\leq 10^{-20}$sec).

The first experiment to investigate ground state two proton emission was performed by Geesaman *et al.* at Stony Brook [Gee77]. They populated the $^{6}\mathrm{Be}_{\mathrm{gs}}$ via the ^{6}Li(^{3}He,t)^{6}Be$\longrightarrow \alpha$+2p reaction with 24 MeV ^{3}He ions. The level diagram for ^{6}Be is shown in figure 1.3a. The ^{6}Be ground state is bound by only 0.59 MeV to decay to ^{5}Li +p and the ground state of ^{5}Li has a very large width ($\sim$ 1.5 MeV). They concluded that neither final state interaction between the two protons nor sequential decay through the tail were consistent with the data.

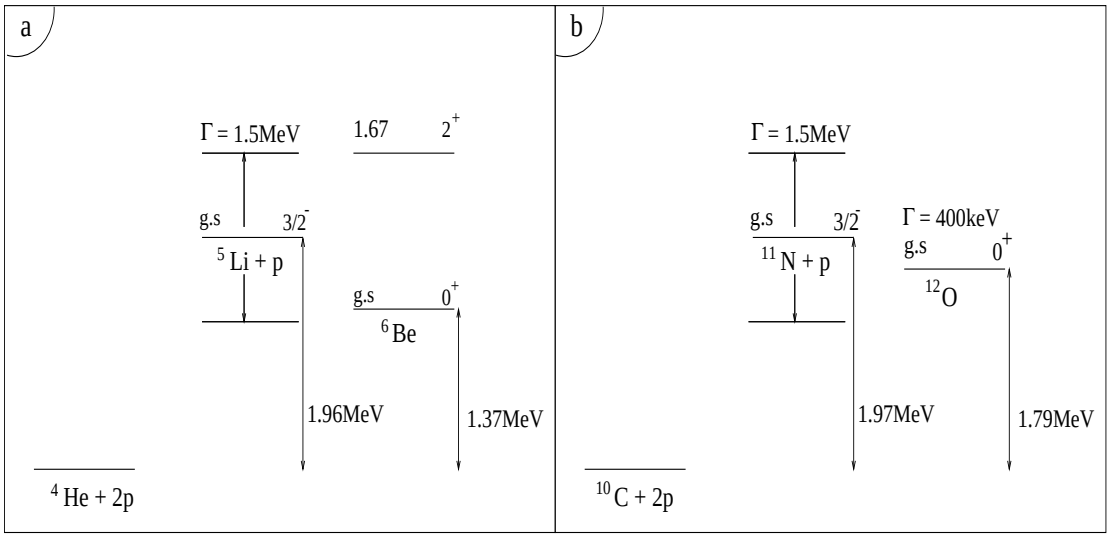

Figure 1.3: *Level diagrams for the two nuclei which have been investigated for ground state proton radioactivity, (a) ^{6}Be and (b) ^{12}O.*

A series of experiments by Bochkarev *et al.* [Boc84, Boc87, Boc89, Boc92] continued to study the decay of the ground state ^{6}Be(0^+) and, in addition, the first excited state ^{6}Be*(2^+). In their latest studies [Boc92], performed at the isochronous cyclotron at I.V. Kurchatov IAE, ^{6}Be levels were populated in the ^{5}Li(^{3}He,t)^{6}Be(0^+,2^+) reaction with a beam energy of 40 MeV. In the kinematically complete experiment the ^{3}H, α-particles and protons were detected.

The conclusion drawn was that the R-matrix approximation, which assumes that the three-body decay can be described in terms of successive binary decays, was not valid for these $2p$ decay processes. They found that sequential emission through the very broad ^{5}Li ground state was not distinguishable from three body breakup because of the short lifetime of the intermediate states. They termed this type of decay as *'democratic'* defining it as occurring when the energy transition between states is less than or equal to the widths of the intermediate states. The measured energy and angular correlations for ^{6}Be have all been understood in terms of a direct decay process using a three body cluster model developed by Danilin *et al.* and summarised in [Dan93]. The decay modes appear to correspond to a 'kinematic focusing' of the $\alpha + p + p$ particles, similar to that in two body. In this case it is difficult to imagine this as two proton emission from a host system.

The most recent experiment has been an investigation into two proton emission from the ground state of ^{12}O by Kryger *et al.* [Kry95]. The use of a radioactive beam makes this experiment particularly relevant to this thesis.

The level diagram is shown in figure 1.3b. The decay Q value for two protons is Q_{2p} = 1.79(04) MeV. The width of the first excited state in ^{11}N is known to be 740$\pm$100 keV and a very rough approximation for the ground state gives a width of 1.5$\pm$0.7 MeV [Kek78]. Thus sequential emission was expected to be suppressed occurring only through the tail of the ground state.

The experiment was performed at the National Superconducting Cyclotron Laboratory using an exotic ^{13}O beam and the ^{9}Be(^{13}O,^{12}O) single neutron stripping

reaction to populate the ^{12}O parent nucleus. The radioactive ^{13}O beam was produced in the fragmentation of 80 MeV/nucleon ^{16}O on a 100mg/cm^2 Be production target. The ^{13}O beam intensity averaged 2400 counts per second. Isotope identification was performed using a $\Delta E - E$ system made up of a double sided silicon strip detector (5cm by 5cm) and four 3mm thick Si(Li) detectors positioned on the beam axis. Protons were detected in the Washington Miniwall detector array. The detector array was composed of 112 CsI detectors arranged in 5 rings around the beam axis covering laboratory angles between 3^o and 12^o. Each ring contained between 16 and 24 detectors. The detector was similar to that used by Stracener *et al.* [Str90].

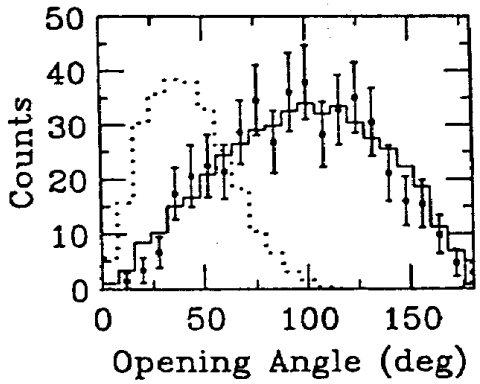

Figure 1.4: *Opening angle spectrum evaluated in the three-particle centre of mass for protons arising from the decay of the ^{12}O ground state from experiments by Kryger et al.. The dotted histogram shows the results of a calculation based upon ^{2}He emission, and the solid histogram shows the results based upon sequential emission through the tail of a broad ^{11}N state.*

A 7% upper limit for the ^{2}He branching ratio was extracted based upon deviation from isotropic emission of the two proton opening angle data shown in figure 1.4. Predictions for the partial diproton width of this state, discussed in section 2.4, gave a 2.7% branching ratio. The conclusions drawn from this experiment were that a similar argument could be made for the democratic decay in the ^{12}O system because of the small ^{2}He branch and the broad expected width of the ^{13}N ground

state. It was also speculated that the good agreement between the ^{12}O data and the sequential emission decay model through the tail of the ^{11}N ground state (see figure 1.4) was because this model approximated a direct three-body decay.

1.2.2 β-delayed two proton emission

β-delayed two proton radioactivity is a relatively new decay process first predicted by Goldansky in 1980 [Gol80]. The process involves the relatively slow β-decay of an isotope to an excited state of its daughter which will subsequently decay by rapid emission of two protons. If this state is the isobaric analog state (IAS) then the decay is β super allowed and the majority of decays populate this state.

Goldansky predicted that odd-odd, $A = 4n + 2$, $T_z = -2$ nuclides would be good candidates for this decay process. Two of the isotopes in this series ^{22}Al and ^{26}P were shown to decay by β-delayed one proton emission in experiments by Cable *et al.* [Cab82,Cab83]. The experiments, performed at the cyclotron at Berkeley, used a 110 MeV ^{3}He^{+2} beam to study the ^{24}Mg(^{3}He,$p4n$)^{22}Al and ^{28}Si(^{3}He,$p4n$)^{26}P reactions. A helium jet transported the recoil nuclei to a counting chamber and deposited them on an aluminium catcher foil. Their decay was recorded using a standard ΔE-E-Veto silicon telescope. The results provided a measurement of the masses of the lowest $T = 2$ analog state in the corresponding β-decay daughters of ^{22}Al and ^{26}P (^{22}Mg and ^{26}Si respectively), which are fed by super allowed β-decay. These states were shown to be unbound to the emission of two protons.

The experiments were repeated using a modified setup shown in figure 1.6. The major difference was the use of a high geometry three element particle telescope capable of identifying and observing two protons simultaneously. The stationary catcher foil was replaced with a slowly rotating aluminium catcher wheel to remove the long lived β activity. These experiments detected the first known cases of β-delayed two proton emission from ^{22}Al and ^{26}P [Cab83b, Hon83]. The conclusions

drawn were that the decay was predominantly sequential in both cases. Figure 1.5 shows an example of the results obtained by [Cab83b] for ^{22}Al demonstrating the energy correlation which results from sequential emission. Figure 1.5a shows two groupings corresponding to transitions involving the ^{20}Ne first excited state and ground state. It is important to note the low level of statistics obtained. The following decay schemes were proposed (see figures 1.8 and 1.9).

The most interesting difference between the two decay schemes is that ^{2}He emission is spin parity forbidden from the β daughter of ^{26}P ($3^{+} \longrightarrow 2^{+}$, 0^{+}: disallowed) but allowed from the β daughter of ^{22}Al. Due to this and the increasing interest behind observing ^{2}He emission the decay of ^{22}Al was remeasured by Jahn *et al.* [Jah85] using position-sensitive detectors and two separate detector setups. The small angle setup was the same as that described previously and, in addition, the large angle setup (see figure 1.7) measured angles ranging from 70^{o} to 164^{o}. The results for the wide angle setup were consistent with an isotropic emission but with the narrow angle setup a 15% admixture of ^{2}He emission could not be excluded. This observed minor enhancement, shown in figure 1.10, at small relative opening angles between the two protons cannot be interpreted as positive evidence for ^{2}He emission due to the large errors arising from the poor statistics of this low yield reaction.

A series of four exotic nuclei with $Z \leq 20$ and $T_z = -\frac{5}{2}$ were predicted by Kelson-Garvey charge symmetry approach [Kel66, Wap85] to be bound to ground state proton emission: ^{23}Si, ^{27}S, ^{31}Ar and ^{35}Ca. All four were expected to have relatively strong decay branches to the $T = \frac{5}{2}$ isobaric analog states in daughter nuclei; with decay from these analog states by both single proton and two proton emission energetically allowed.

J. Äystö *et al.* found that ^{35}Ca was a β-delayed sequential two proton emitter [Äys85] in an experiment using the small angle setup of figure 1.6.

The isotope ^{31}Ar was first observed in a fragmentation reaction experiment per-

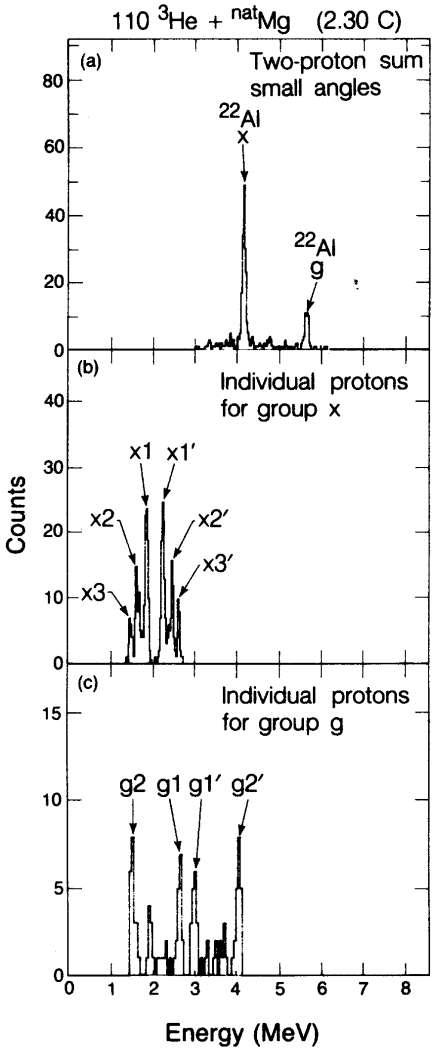

Figure 1.5: *Proton-proton coincidence spectra obtained with the narrow-angle detector system following the decay of ^{22}Al [Cab83b]. (a) Two-proton summed energy spectrum. Groups x and g correspond to transitions invoving the ^{20}Ne first excited state and ground state, respectively. (b) Primed peaks probably correspond to the first emitted proton. (c) Individual proton energy spectrum for protons forming group g in part (a). In this case, $g1$ and $g2'$ correspond to the first emitted protons.*

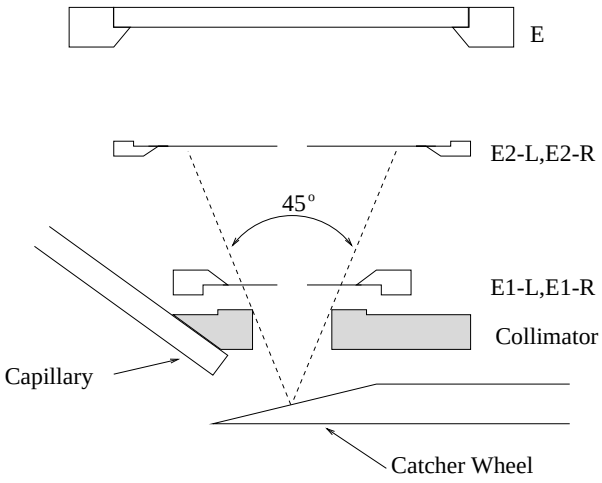

Figure 1.6: *Schematic diagram of the narrow angle detector system as used by [Cab83b, Hon83]. The helium-jet transports the activity to the chamber via the capillary to the rotating catcher wheel.*

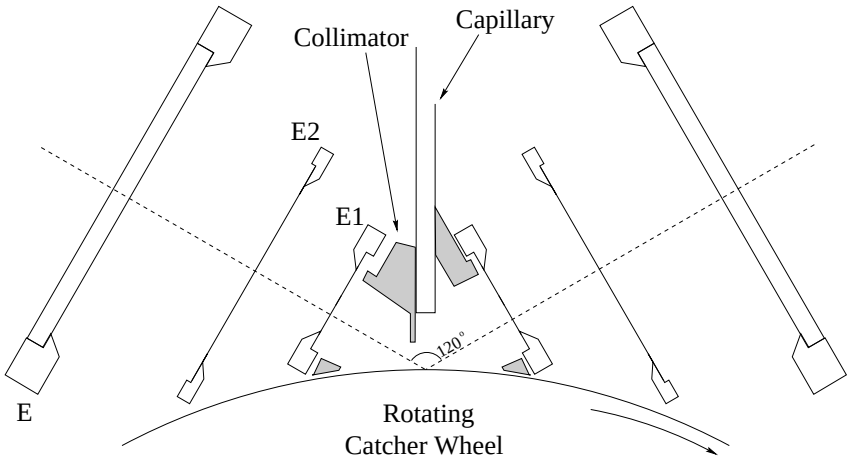

Figure 1.7: *Schematic diagram of the wide angle detector system as used by Jahn et al. [Jah85].*

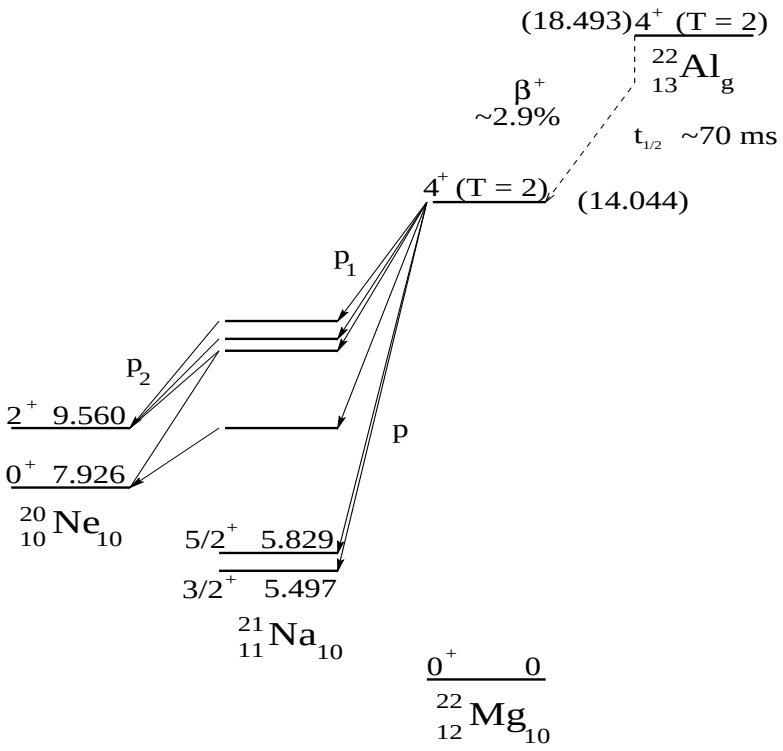

Figure 1.8: *Partial decay scheme for ^{22}Al given in [Cab84].*

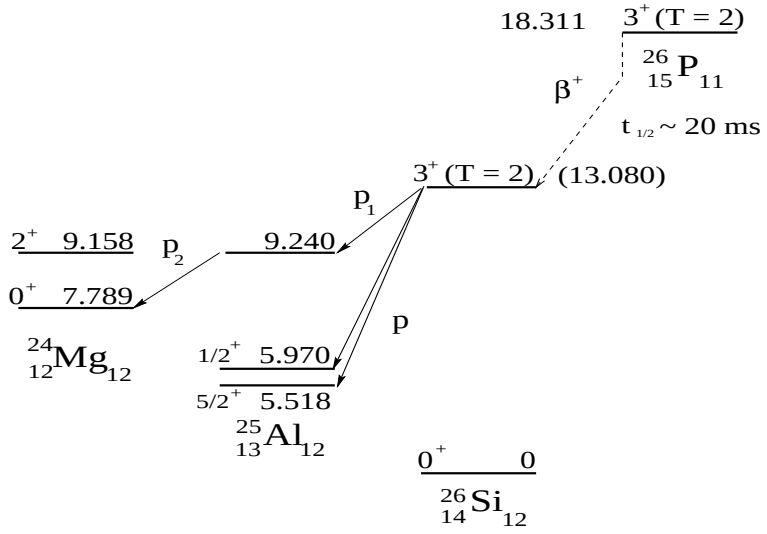

Figure 1.9: *Partial decay scheme for ^{26}P given in [Cab84].*

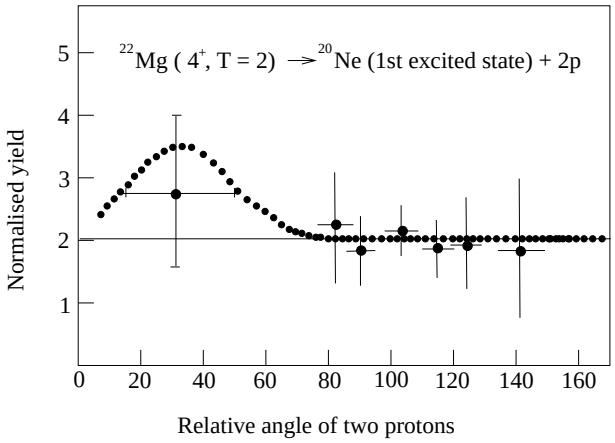

Figure 1.10: *Dotted line corresponds to a 15% admixture of ^{2}He emission to an otherwise isotropic distribution.*

formed at GANIL using the LISE spectrometer by Borrel *et al.*[Bor87]. The heavy ions were implanted and identified in a five member solid-state telescope located at the focal point of LISE as shown in figure 1.11. The ^{31}Ar measured half-life was found to be $t_{1/2}$=15±3ms consistent with that expected for β-decay. The experiment also saw a signal for β-delayed one proton emission.

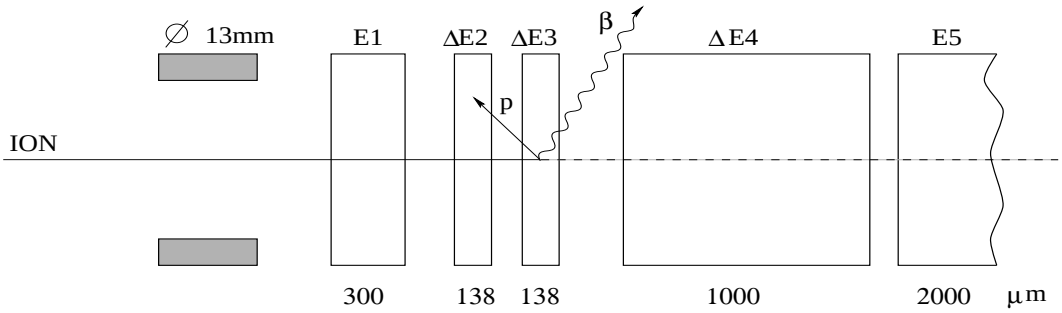

Figure 1.11: *The solid state telescope used by Borrel et al. [Bor87] Heavy ions are implanted in detectors $\Delta E2$ or $\Delta E3$ and the protons are detected in detectors $\Delta E1$ to $\Delta E4$. E5 is used as a veto to reject high energy protons.*

Further experiments by Reiff *et al.* and Borge *et al.* [Rei89, Bog90] verified the existence of β-delayed two proton emission via several intermediate states in ^{31}Cl. The second of these experiments observed no evidence for ground state two

proton emission giving the branching ratio an upper limit of 5%. The conclusions drawn were that the energy available to the two protons ($\sim$ 70 keV) was too small to allow transmission through the combined Coulomb and centrifugal barriers to compete with β-decay.

More recently Bazin *et al.* [Baz92], using a more sophisticated silicon-detector telescope than [Bor87], observed β-delayed three proton emission from ^{31}Ar for the first time.

The isotope ^{39}Ti found on the proton drip line was investigated by Détraz *et al.* and Moltz *et al.* [Dét90, Mol92]. The latter observed sequential β-delayed two proton emission and predicted a ^{39}Ti mass with a two proton separation value of S_{2p} = -530$\pm$65 keV. Although higher than the 70 keV measured for ^{31}Ar it was predicted to be too low for ground state two proton emission to compete with the 28ms β-decay.

The other isotopes which have been observed to undergo $\beta 2p$ are ^{27}S [Bor91], ^{43}Cr [Bor92] and ^{46}Mn [Bor92].

The point to emphasise about these experiments is the low level of statistics obtained in each one because they rely on an initial β-decay to populate the state which is of interest. This low level of statistics makes a thorough investigation into the strength of a ^{2}He component very difficult as seen in the data shown previously in figure 1.10.

This has been overcome in the experiment described in this thesis by using a radioactive beam to directly populate the state which we wish to investigate. An overview of the present experiment and its aims is given in the next section.

1.3 The present experiments

In the experiments described in this thesis project the 7.77 MeV excited state in ^{14}O was populated using 45 MeV $^{13}N^{3+}$ radioactive ion beam.

Figure 1.12 shows where the proton and two proton daughters lie. The state has a measured width of 76±10 keV, $J^{\pi} = 2^{+}$ and decays by proton emission [Ajz91]. It is unbound to two proton emission by 1.2 MeV. This is lower than the $Q_{2p} = 1.79$ MeV for the ^{12}O case [Kry95] but larger than those for ^{39}Ti and ^{31}Ar reported previously. The solid line in figure 1.12 shows the path taken by emission of a ^{2}He cluster. Sequential emission is shown by the dashed line. It is energetically only possible for the sequential decay mechanism to proceed via a single intermediate state in ^{13}N. This is a $1/2^{+}$ state with a width of 33.7±0.9 keV [Ajz91]. The details for the other levels in ^{14}O are given in table 1.1.

E_x (MeV± keV)	$J^{\pi};T$	$\tau_{1/2}$ or $\Gamma_{\mathrm{c.m.}}$ (s) (keV)	Decay
g.s.	$0^{+};1$	$\tau_{1/2} = 70.606\pm$ 0.018 s	β^{+}
5.173±10	$1^{-};1$	$\Gamma = 38.1 \pm 1.8$ keV	
5.920±10	$0^{+};1$	≤50	p
6.272±10	$3^{-};1$	103±6	p
6.590±10	$2^{+};1$	≤60	p
(6.790±30)	$\pi = -$		
7.768±10	$2^{+};1$	76±10	p
(8.72±40)			
9.715±20	$(2^{+});1$		
9.915±20	$4^{+};1$	100±50	

Table 1.1: *Energy levels in ^{14}O [Ajz91].*

The 7.77 MeV state in ^{14}O also forms an isospin $T = 1$ triad with states in ^{14}N and ^{14}C shown in figure 1.13. Thus, since $^{12}C_{gs}$ has isospin $T = 0$ and ^{2}He has isospin $T = 1$, emission to the ground state in ^{12}C is isospin allowed.

The ^{14}O states have been observed by the ^{12}C(^{3}He,n) transfer reaction by Feng *et al.* [Fen78]. The excited states are described by a ^{12}C core plus two protons moving in the s, p and d shells. For the 7.77 MeV state the dominant shell model configuration is known to be made up of equal amplitudes of $[sd]$ and $[p_{3/2}p_{1/2}]^{-1}$ [Bal67, Bal69]. The excited state is 2^+, thus, the protons must be spin coupled in antiparallel.

The search for diproton emission from the 7.77 MeV excited state in ^{14}O was initially planned as a two step process. A first experiment to attempt to observe a signal for $2p$ emission and if successful to follow up with a second which would attempt to identify the decay mechanism.

Chapter 2 offers a discussion on the theoretical background for ^{2}He emission and proton emission showing how the widths can be calculated.

Chapter 3 contains all the details of the experimental technique as well as a discussion of the results obtained from the commissioning run and the conclusions which led to the redesign of the detection system. The setup of the second run and a preliminary analysis of the data are then presented.

The decay mechanisms have been simulated using a Monte Carlo program. These simulations are discussed fully in chapter 4.

The final chapter concentrates on the analysis of the follow-up run and compares the data obtained with the different simulations.

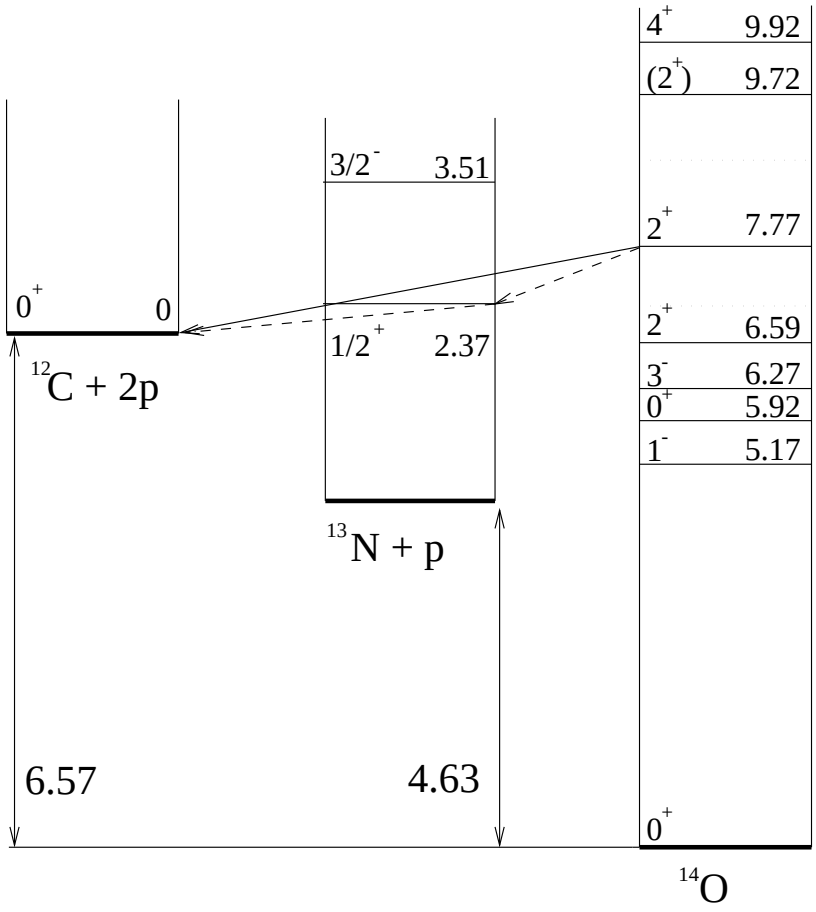

Figure 1.12: *Level scheme for ^{14}O, proton daughter and two proton daughter. The dashed line shows the sequential emission of two protons through an intermediate state and the solid line emission of semi-bound ^{2}He cluster.*

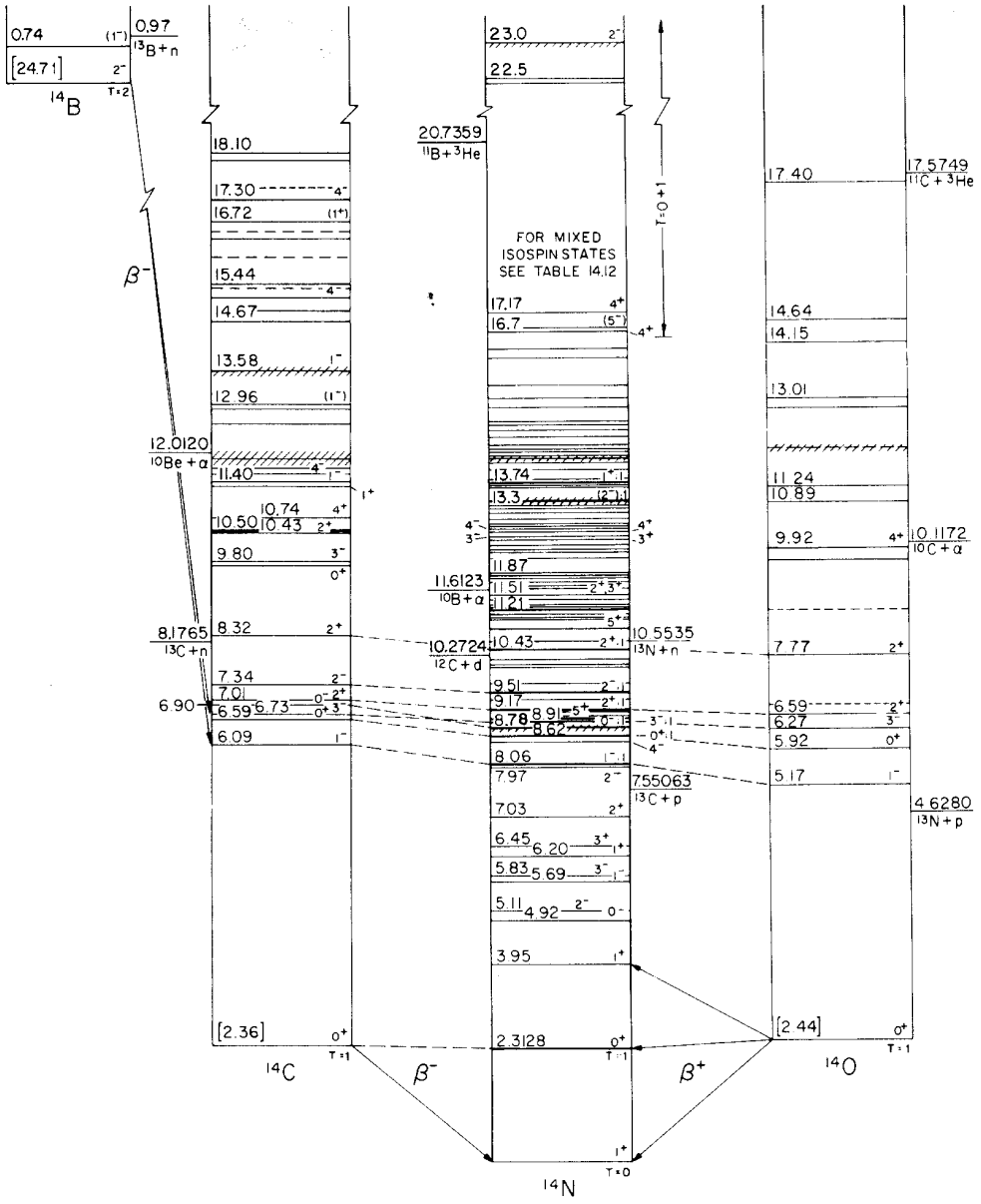

Figure 1.13: *Isobar diagram for $A = 14$ [Ajz91].*

Chapter 2

Theory

Two proton emission can be driven by a number of mechanisms as discussed in section 1.1.

The diproton or ^{2}He is considered as a semi-bound particle moving in the field of the two proton daughter nucleus from which it may escape by quantum tunneling through the potential barrier. The barrier penetrability and the interaction between the two protons will determine the likelihood of diproton emission.

Two proton emission can also proceed by the sequential emission of two protons. Sequential emission is modelled using proton decay with the same basic model as that for diproton decay.

This chapter presents the theoretical background required to model both diproton and proton decay and to predict the widths and half-lives. To begin, a general summary of the kinematics involved in a three body reaction is given.

2.1 Three body kinematics

The approach taken here is based on that by G.C.Ohlsen [Ohl65]. The following notation is used for a reaction which is in the form

$$m_p + m_t \longrightarrow m_1 + m_2 + m_3$$

where subscripts p and t refer to the projectile and target respectively and $1, 2$ and 3 refer to the three final particles. Superscripts l and c refer to the laboratory and the centre of mass frames of reference. The following treatment is non-relativistic.

The relationship between the energy and angle in l and c is shown in the velocity diagrams in figure 2.1a. V is the magnitude of the velocity of the centre of mass and is given by

$$V = (2m_p E_p^l)^{\frac{1}{2}}/(m_p + m_t) \tag{2.1}$$

Using the cosine rule on the equivalent energy diagram figure 2.1b, where $a_1 =$

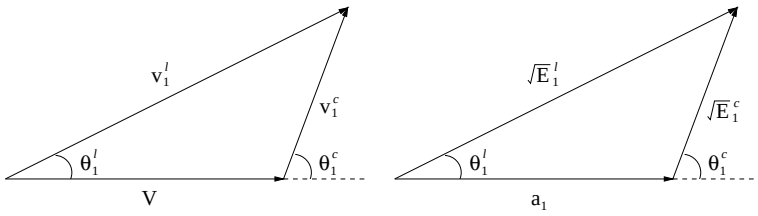

Figure 2.1: *Velocity diagram comparing l and c reference frames*

$(\frac{1}{2}m_1V^2)^{\frac{1}{2}}$ is introduced to simplify the equations, we obtain relationships between l and c frames of reference

$$E_1^c = E_1^l - 2a_1(E_1^l)^{\frac{1}{2}}\cos\theta_1^l + (a_1)^2 \tag{2.2}$$

$$\cos\theta_1^c = \frac{(E_1^l)^{\frac{1}{2}}\cos\theta_1^l - a_1}{(E_1^l - 2a_1(E_1^l)^{\frac{1}{2}}\cos\theta_1^l + (a_1)^2)^{\frac{1}{2}}} \tag{2.3}$$

$$\phi_1^c = \phi_1^l \tag{2.4}$$

where ϕ is the azimuthal angle. The inverse relations are given by

$$E_1^l = E_1^c + 2a_1(E_1^c)^{\frac{1}{2}}\cos\theta_1^c + (a_1)^2 \tag{2.5}$$

$$\cos\theta_1^l = \frac{(E_1^c)^{\frac{1}{2}}\cos\theta_1^c + a_1}{(E_1^c + 2a_1(E_1^c)^{\frac{1}{2}}\cos\theta_1^c + (a_1)^2)^{\frac{1}{2}}} \tag{2.6}$$

$$\phi_1^l = \phi_1^c \tag{2.7}$$

The total energy available to the three particles in the c system is given by

$$E_{tot}^c = Q + m_t E_p^l/(m_p + m_t). \tag{2.8}$$

Q is the 'Q value' of the ground state reaction, i.e. $Q = (m_t + m_p - m_1 - m_2 - m_3)c^2$, and E_p^l is the projectile energy in the laboratory.

When two of the three final particles are detected (1, 2) in coincidence at a particular pair of angles then from momentum and energy conservation the allowed energies must satisfy the following expression derived by Ohlsen,

$$\begin{aligned}\tfrac{1}{m_3}[E_1^l(m_1+m_3) + E_2^l(m_2+m_3) - 2(m_p m_1 E_p^l E_1^l)^{\frac{1}{2}}\cos\theta_1^l \\ -2(m_p m_2 E_p^l E_2^l)^{\frac{1}{2}}\cos\theta_2^l + 2(m_1 m_2 E_1^l E_2^l)^{\frac{1}{2}}\cos\theta_{12}^l] \\ = E_p^l(1 - \tfrac{m_p}{m_3}) + Q\end{aligned} \tag{2.9}$$

where

$$\cos\theta_{12}^l = \cos\theta_1^l\cos\theta_2^l + \sin\theta_1^l\sin\theta_2^l\cos(\phi_1^l - \phi_2^l). \tag{2.10}$$

Equation(2.9) describes an ellipse in $(E_1^l)^{\frac{1}{2}} - (E_2^l)^{\frac{1}{2}}$ space. The relative energy between the detected particles can be obtained from its definition,

$$\epsilon = \frac{1}{2}\mu_{12}v_{12}^2 \tag{2.11}$$

where $\mu_{12} = m_1 m_2/(m_1 + m_2)$ and v_{12}^2 is the relative velocity as depicted in figure 2.2. Using the cosine rule we obtain

$$\epsilon = \frac{1}{m_1 + m_2}[m_2 E_1^l + m_1 E_2^l - 2(m_1 m_2 E_2^l E_1^l)^{\frac{1}{2}}\cos\theta_{12}^l] \tag{2.12}$$

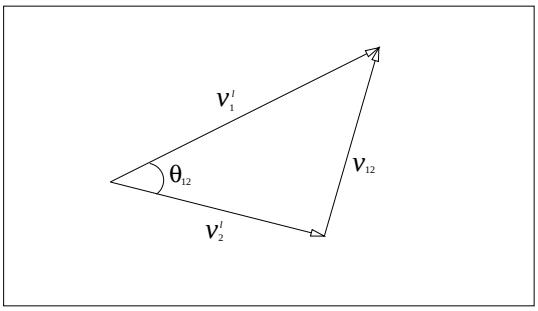

Figure 2.2: *Velocity diagram for two detected particles showing relative angle and relative velocity.*

2.2 Model for diproton emission

The semi-classical picture used for ^{2}He or diproton decay is analogous to that of α-decay developed by Gamow [Gam28] and that of proton decay (references summarised in [Hof89]).

The accepted model used by Brown *et al.* and Kryger *et al.*, [Bro91, Kry95] treats the diproton as a preformed particle in the potential well of the two proton daughter nucleus. It differs from proton decay in that the diproton is in a relative $^1S_0$ state with spin zero and thus no spin-orbit term is included in the total potential. The total amount of energy available to the two protons is given by Q_{2p}. A fraction of this energy, which we call ϵ, is converted into the mass of the ^{2}He. The remainder, $E_{2p} = Q_{2p} - \epsilon$, is the energy available for the diproton to tunnel through the barrier. When the cluster penetrates the barrier it breaks up into two protons with ϵ converted into the relative energy of the pp pair. The relative energy is given by equation(2.12) with $m_1 = m_2 =$ mass of proton

$$\epsilon = \frac{1}{2}[E_1^l + E_2^l - 2(E_2^l E_1^l)^{\frac{1}{2}} \cos\theta_{12}^l] \tag{2.13}$$

In the reaction studied in this thesis $Q_{2p} = 1.2$ MeV as can be seen from the level diagram in figure 1.12.

Figure 2.3 shows the commonly used case of a constant square nuclear potential of $-V_o$ up to the nuclear radius R_n and also shows the outer turning point R_{outer} for a diproton with energy E_{2p}. The nuclear radius is defined as

$$R_n = R_o \times (A^{1/3} + 2^{1/3}) \tag{2.14}$$

where A is the mass of the daughter nucleus and R_o can vary from 1.20 - 1.40fm depending on the literature.

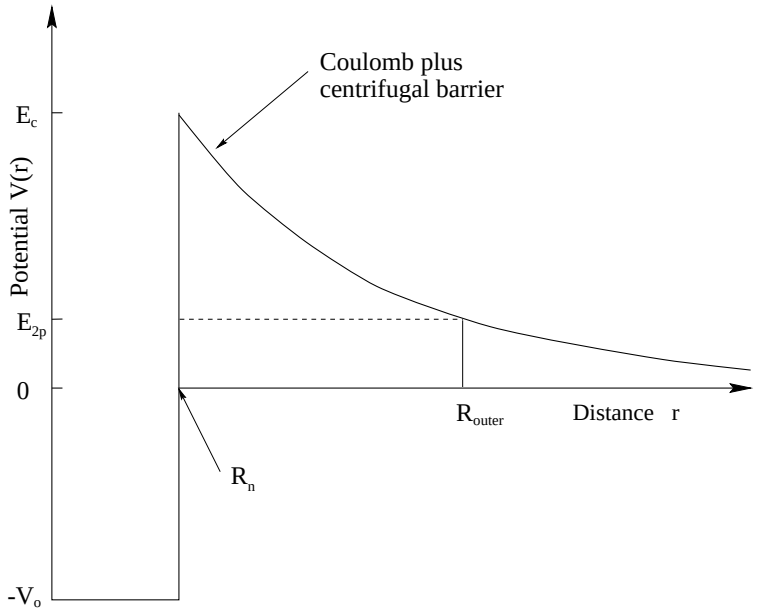

Figure 2.3: *Potential barrier seen by a diproton with energy E_{2p} showing the turning point at the nuclear radius R_n and the outer turning point R_{outer}.*

Angular momentum and parity conservation rules apply;

$$\vec{J_i} = \vec{J_f} + \vec{l} \tag{2.15}$$

$$\pi_i = \pi_f(-1)^l \tag{2.16}$$

where $\vec{J_i}, \vec{J_f}$ and π_i, π_f are the total spins and parities of the parent and daughter nuclei and l is the angular momentum carried by the diproton. The transition which we consider is $2^+ \longrightarrow 0^+$ (see figure 1.12), hence, the diproton will carry two units of angular momentum.

Lane *et al.* and MacFarlane *et al.* give an expression for the partial width [Lan58,

Mfr60]. This has been modified for the case of diproton decay and is given by

$$\Gamma_{\text{part}} = 2\theta_1^2\gamma_1^2 P(E_{2p}) \tag{2.17}$$

where $P(E_{2p})$ is the penetrability or probability of transmission through the barrier and γ_1^2 the Wigner single particle width (also called the reduced width) defined as

$$\gamma_1^2 = \frac{3\hbar^2 c^2}{2\mu R_n^2}, \tag{2.18}$$

where $\mu(= [2 \times A/(A+2)] \times 931.501$ MeV/c^2) is the reduced mass. θ_1^2 is the spectroscopic factor defined as the probability of finding the excited state in the correct configuration for diproton emission, i.e. a ^{12}C core + a ^{2}He with $l = 2$. This dimensionless number contains the nuclear structure information.

The penetrability P is found by applying the WKB (Wentzel, Kramers & Brillouin) approximation

$$P = e^{-2G} \tag{2.19}$$

The Gamow factor G is the integral between the points R_n and R_{outer} (see figure 2.3):

$$G = \sqrt{2\mu/\hbar^2} \int_{R_n}^{R_{outer}} (V(r) - E_{2p})^{\frac{1}{2}} dr \tag{2.20}$$

The potential in this equation is the superposition of the Coulomb potential $V_C(r)$ and the centrifugal potential $V_l(r)$.

$$V(r) = V_C(r) + V_l(r) \tag{2.21}$$

The Coulomb potential is given by

$$V_C(r) = \frac{zZe^2}{4\pi\epsilon_\circ r} \tag{2.22}$$

where z, Z are the charge of the diproton ($z = 2$) and daughter nucleus respectively.

The centrifugal term $V_l(r)$ depends on the angular momentum of the diproton:

$$V_l(r) = \frac{l(l+1)\hbar^2}{2\mu r^2} \tag{2.23}$$

Figure 2.4 shows how the different terms in the potential vary with radial distance r. The dotted line is $V_C(r)$, dashed line $V_l(r)$ and solid line is the sum of the two terms. Figure 2.5 shows the dependence of the penetrability P with the relative energy ϵ of the pp pair. For low ϵ the ^{2}He has less mass and hence the diproton has more kinetic energy and is more likely to tunnel through the barrier. The probability of penetration becomes less likely as the kinetic energy decreases, i.e. as ϵ increases.

The total width for diproton decay depends on the interaction between the two protons which is considered in the next section.

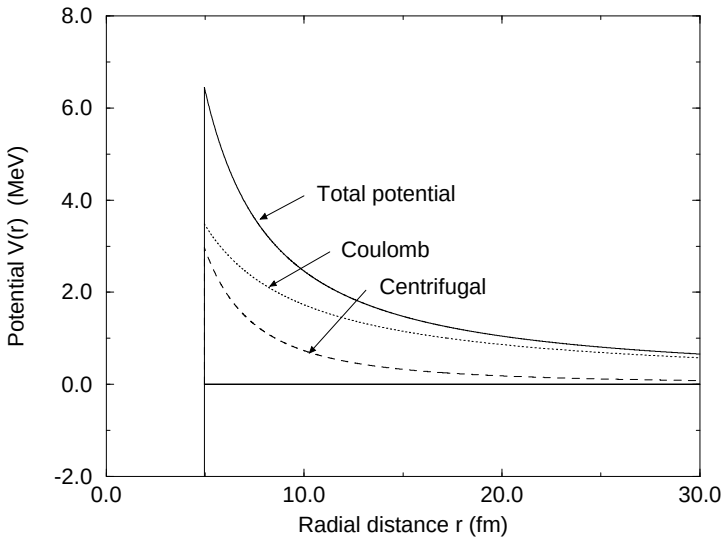

Figure 2.4: *$V_C(r)$ (dotted line), $V_l(r)$ (dashed line) and the sum of the two (solid line) for a diproton with angular momentum $l = 2$ in the potential well of a ^{12}C nuclei using $R_o = 1.4$fm in equation(2.14).*

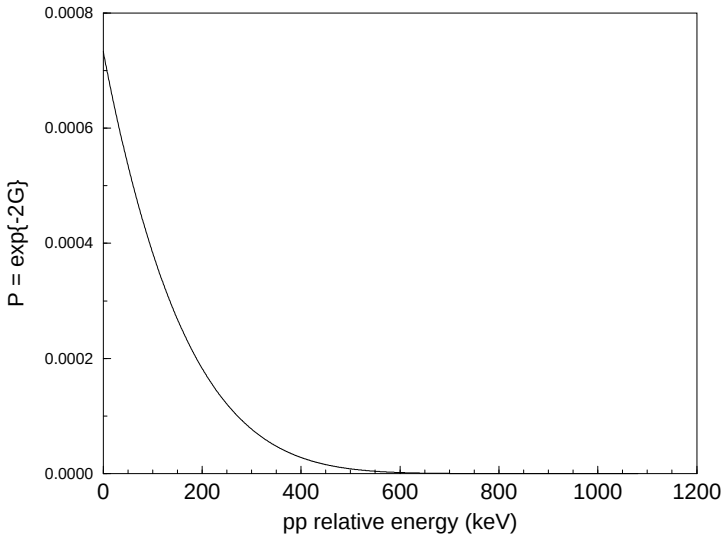

Figure 2.5: *Penetrability $P = e^{-2G}$ for a diproton with $l = 2$ in the potential well of a ^{12}C nuclei plotted against ϵ the relative pp energy.*

2.3 Final State Interaction (FSI)

When particles are produced in a nuclear reaction some of them interact among themselves so strongly that they influence appreciably the properties of the reaction cross section. These processes are known as final state interactions.

A very important aspect of the role played by this interaction is that it may greatly modify the angular distributions and the energy spectra of the particles which have been produced and yet will play no important role in the primary mechanism. It is as if the reaction first takes place as if there were no final state interaction and is then distorted by the short-range nuclear interactions before the produced particles can escape the range of their mutual forces.

2.3.1 Experimental evidence for two proton FSI

It is well known that ^{2}He or the diproton does not have any bound states. In many reactions, which produce ^{2}He as a residual nucleus, an enhancement of the

cross section at small relative pp energies ϵ, has been observed. Reactions in the form $A + B \longrightarrow X + p + p$ experiments which have detected ^{2}He can be divided into two sets; those that detect X and those that detect the two protons.

The first group studied the reactions ^{3}He(d,t)2p [Con64], ^{2}H(p,n)2p [Slo68, Dai73]. Enhancements in triton and neutron spectra at high energies, corresponding to low pp energies, were observed. This enhancement was attributed to the pp final state interaction of the the relative unbound $^1S_0$ state of ^{2}He.

Figure 2.6 shows the triton spectrum from the work of Conzett *et al.* [Con64]. The spectrum is fitted with final state interaction theoretical curves of Watson-Migdal, which are described in the next section.

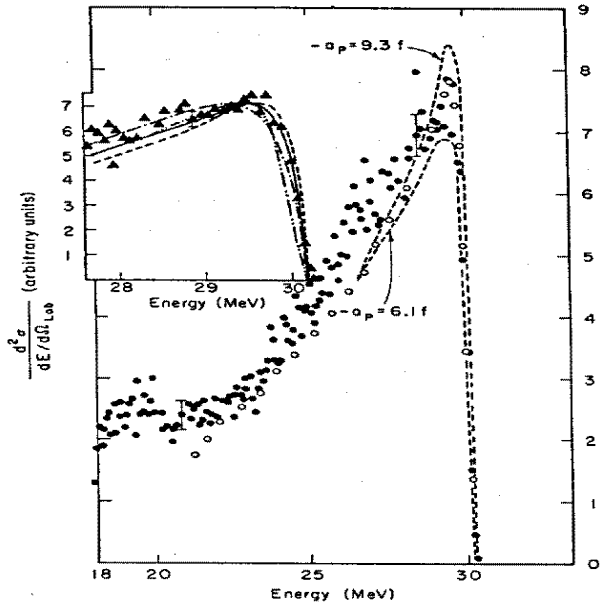

Figure 2.6: *Triton energy spectrum from Conzett et al. for the reaction ^{3}He(d,t)2p with E_d=33.4 MeV. Solid circles are data points and the fitted lines use different values of scattering length a_p for Watson-Migdal fits.*

The second category of experiments require the experimentally more complicated detection of two low relative energy protons. This has been investigated by a number of authors [Jah78, Sta79, Cog80, Dri80, Ohn93]. The conclusions drawn

are that the distribution of the relative energy ϵ of the two protons originating from ^{2}He is rather broad. It peaks at $\sim$ 400 keV and falls off slowly for higher relative energies.

In a recent experiment by Ohnuma *et al.* a high energy beam of deuterons was used to bombard light nuclei to study (d,^{2}He) reactions [Ohn93]. The relative energy spectra for two protons detected in coincidence is shown in figure 2.7. Good agreement is obtained with the solid line representing the Watson-Migdal FSI approximation which is explained in the next section.

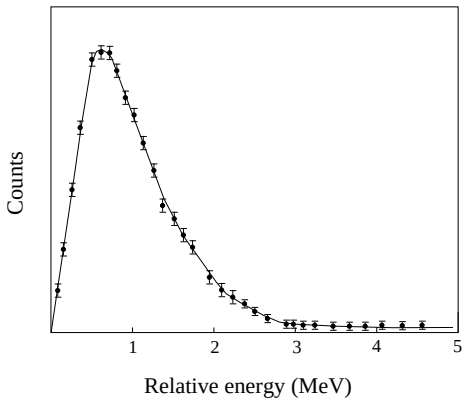

Figure 2.7: *Proton relative energy spectrum from Ohnuma et al. with solid line showing Monte Carlo calculations based on the Watson-Migdal final state interaction approximation.*

2.3.2 Theoretical framework for FSI

The theory of final state interaction has been treated by Watson and Migdal [Wat52, Mig55]. What follows is a concise description of FSI theory based on the work of R.J.N. Phillips [Phi64]. This closely follows Watson's approach and requires that three general conditions are fulfilled;

1) Mechanism of the reaction cross section must be short range,

2) Effect of FSI is to be considered only for low relative energies of the particles.

3) FSI must be strong and attractive.

Suppose that the interaction operator in the Schrödinger equation is separated into two terms $\nu + V$, where ν is the two nucleon final state interaction which vanishes except when operating on the designated set. Watson shows that the transition amplitude may be written

$$T_{fi} = \langle \phi_f^{(-)} | V | \psi_i^{(+)} \rangle, \tag{2.24}$$

where $\psi_i^{(+)}$ is the complete scattering eigenfunction for the initial state (with outgoing wave boundary conditions); $\phi_f^{(-)}$ is the eigenfunction for the final state under interaction ν alone (with ingoing wave boundary conditions). When a Coulomb force acts, as in the case for two protons, the outer wave function is

$$\begin{aligned} \phi_f^{(-)} &= e^{-i\delta}(F\cos\delta + G\sin\delta)/(kr) \\ &\approx e^{-i\delta}\sin\delta(1 - \frac{r}{a})/(Ckr), \end{aligned} \tag{2.25}$$

where r and k are the separation and the relative momentum of the proton pair respectively. The approximation neglects terms of order k^2r^2, k^2rr_o and r/R. $R = \hbar^2/(e^2m_p) = 28.8$fm, the Bohr radius of a proton bound to a fixed unit charge; F and G are the regular and irregular S-wave Coulomb wave function; C is the Coulomb penetration factor; δ is the pp phase shift, related to the pp scattering length a_{pp} and effective range r_{pp} by

$$C^2k\cot\delta + h(\eta)/R = -1/a_{pp} + \frac{1}{2}r_{pp}k^2. \tag{2.26}$$

To complete all the definitions a_{pp} = -7.69fm and r_{pp} = 2.66fm. Sommerfield parameter $\eta = e^2/\hbar u$, u is the pp relative velocity; $e^2/\hbar c$ is the fine structure constant; $C^2 = 2\pi\eta/(\exp(2\pi\eta) - 1)$ and $h(\eta) = -\ln\eta + Re\frac{\Gamma'(1+i\eta)}{\Gamma(1+i\eta)}$ which can be written in the form [Jac50]

$$h(\eta) = -\ln\eta - 0.5572 + \eta^2 \sum_{n=1}^{\infty} \frac{1}{n(n^2+\eta^2)}. \tag{2.27}$$

The shape of the relative energy distribution for the two protons is given by Bernstein *et al.* [Ber84] in their statistical model for the emission of particle unstable resonances from compound nuclei. Using experimental data by van Driel *et al.* [Dri80], which suggests that FSI formalism is valid up to relative energies of at least 2 MeV, they propose that the density of states $\rho(\epsilon)$ is described by

$$\begin{aligned} \rho(\epsilon) &= a\left(\frac{\exp(2\pi\eta)-1)}{\eta}\right)\left(\frac{\sin^2\delta(k)}{k}\right) \qquad \epsilon \leq 2.0\text{MeV} \\ &= b\exp(-c\epsilon) \qquad\qquad\qquad\qquad\qquad\quad \epsilon > 2.0\text{MeV} \end{aligned} \tag{2.28}$$

where $\delta(k)$ is obtained from equation(2.26), a and b are chosen so that $\rho(\epsilon)$ is both normalised and continuous at ϵ = 2.0 MeV and c is a free parameter.

Figure 2.8 illustrates the plot produced using expression (2.28) with a cut off at 1.2 MeV which is the maximum for ^{2}He emission from the 7.77 MeV excited state in ^{14}O.

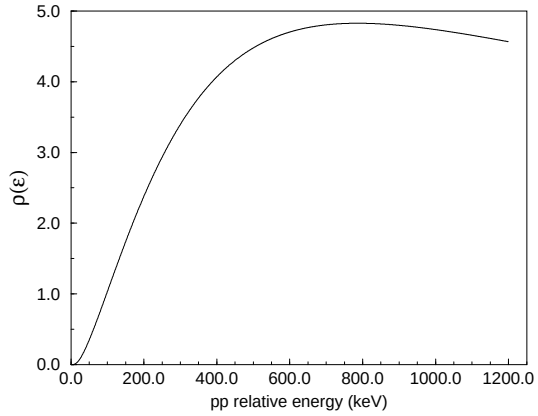

Figure 2.8: $\rho(\epsilon)$ *according to FSI theory of Watson-Migdal.*

^{2}He emission depends on this final state interaction and on the penetrability. These two elements are combined in section 4.3 to give a probability distribution which is used in the Monte Carlo simulations for ^{2}He emission.

2.4 Width predictions

The total diproton width is defined as

$$\Gamma_{\rm dip}(=\hbar \ln 2/t_{\frac{1}{2}}) = \int \Gamma_{\rm part}\rho(\epsilon)dE_{2p} \tag{2.29}$$

where the diproton partial width, $\Gamma_{\rm part}$, is given in expression (2.17), $\rho(\epsilon)$ is the density of states of the ^{2}He and $t_{\frac{1}{2}}$ is the half-life for diproton emission. Two methods can be used to calculate this total diproton width.

The first is called the R-matrix formalism which is suitable for the emission of a very long-lived particle. It is obtained by replacing the density of states $\rho(\epsilon)$ in the expression for the total width by a delta function, $\delta(\epsilon)$.
The second method uses the final state interaction expression for $\rho(\epsilon)$ given by equation(2.28) and normalises the density of states by $\int_o^\infty \rho(\epsilon)d\epsilon = \frac{1}{3}$. This normalisation of the density of states follows because the pp singlet state is a virtual state which corresponds to a scattering density of states of approximately $\frac{1}{3}$ [Php60, Kry95].

The first method gives a much larger value for the total width than the second because of the assumption that the particle is long lived. In the work of Kryger *et al.*, which has been discussed in section 1.2.1, they found that the first method predicted a width of 225 keV corresponding to a 40% branching ratio for a delta function at $\epsilon = 150$ keV and $l = 0$. The final state interaction method gave a total width of only 16 keV well within their measured branching ratio limit for ^{2}He emission of 7%, thus leading to the conclusion that the latter was the better model.

These two methods have been used to calculate the widths for diproton emission from the excited state in ^{14}O and the results will be discussed in chapter 5. The program used for these calculations was tested by reproducing the predictions obtained by Kryger *et al.* [Kry95b].

2.5 Proton emission

The same model that describes diproton emission is used for proton emission. In this case all the available energy is kinetic, i.e. $Q_p = E_p$, and a term for the spin-orbit potential must be included in the total potential given in equation(2.21). This spin-orbit potential has a strength and a sign which is dependent on the product of the proton spin σ and proton angular momentum l, and is written,

$$V_{so}(r) = \vec{\sigma}.\vec{l}\lambda_\pi^2 \frac{1}{r}(\frac{d}{dr}(f(r, R_{so}, a_{so}))) \tag{2.30}$$

where $f(r, R, a)$ is the Woods Saxon form factor;

$$f(r, R, a) = [1 + \exp((r - R)/a)]^{-1} \tag{2.31}$$

and

$$\vec{\sigma}.\vec{l} = l \qquad \text{for} \quad j = l + \frac{1}{2} \tag{2.32}$$

$$\vec{\sigma}.\vec{l} = -(l+1) \qquad \text{for} \quad j = l - \frac{1}{2}(l > 0) \tag{2.33}$$

$$R_{so} = 1.01fm \times A^{\frac{1}{3}} \tag{2.34}$$

$$a_{so} = 0.75fm \tag{2.35}$$

and λ_π is the pion Compton wavelength ($\simeq \sqrt{2}$fm). The definitions are taken from Hofmann [Hof89].

The widths for proton decay are calculated using the same equation as that for diproton, i.e. equation(2.17) with all variables corrected for the case of a proton and one proton daughter system. The main difference between the two being that in the case of proton emission no density of state function needs to be considered.

The results of width predictions using this model will be discussed in chapter 5. Previous attempts to predict proton widths and half-lives using different optical model nuclear potentials from which both the inner and outer turning points can be calculated [Pag90] will also be discussed.

Chapter 3

Experimental system

The problems which face experimentalists using radioactive beams have been outlined earlier as being very low beam currents and large backgrounds from the decay of the beam. When the Edinburgh Nuclear Physics group began its collaboration at Louvain-la-Neuve in mid-1992 it proposed to build up a general detection system which could extract data under these conditions. As the first PhD student involved in this work a major part of the initial work was the installation and testing of such a system.

This chapter contains a general description of the detection system and electronics that were used in the two experiments, i.e. commissioning and follow-up. The results of the first experiment are discussed in some detail so that the experimental modifications in the second can be understood. The end of the chapter contains some initial results relating to the overall performance for the detection system of the second experiment.

The chapter begins with a description of the Radioactive Ion Beams Facility (RIBF) at Louvain-la-Neuve and production of a $^{13}N^{3+}$ RIB.

3.1 The ARENAS^3 facility at Louvain-La-Neuve

The ARENAS^3 facility is based on the post acceleration of mass-separated radioactive ion beams. The short-lived radioactive species are produced in the bombardment of a target, located in the shielding between the two cyclotrons, with a 150μA 30 MeV proton beam from the CYCLONE 30 cyclotron. They diffuse out of the hot target, which is heated by the proton beam alone, and are pumped towards an ECR source. Before going to the ion source the gas passes different traps in order to reduce the gas load, consisting mainly of H_2O, N_2, CO_2 and hydrocarbons. The dedicated ECR ion source has been designed to optimise the yields for low charge states (1^+ to 3^+) [Dec91]. These ions are extracted out of the ECR source (extraction voltage ≤ 7 kV), separated by a 90^o analysing magnet, transported to the second accelerator using two lenses and are axially injected into CYCLONE through a 90^o bending magnet. This K=110 ($E \leq 110q^2/A$) cyclotron accelerates the ions to the desired energy. Figure 3.1 shows the layout of the two cyclotrons with figure 3.2 showing the layout of the entire facility.

CYCLONE has been modified in the central region to allow its operation in the sixth harmonic mode which is required to obtain the low energies required for astrophysics experiments [Jon89]. The accessible energy range goes up to 0.6 and 9 MeV/nucleon in the sixth and third harmonic modes respectively. An overview of the beams available at the facility in Louvain-la-Neuve is given in table 3.1.

The radioactive ion beam intensity is obtained from the equation;

$$Y = \sigma \Phi N \epsilon_{extr} \epsilon_{ion} \epsilon_{acc} \tag{3.1}$$

where σ is the formation cross section, Φ the primary beam intensity and N is the thickness of the target. ϵ_{extr} is the efficiency with which the ions are extracted from the target. ϵ_{ion} is the ionisation efficiency. ϵ_{acc} is the acceleration efficiency of the second cyclotron. The next section details the production of ^{13}N and values for these efficiencies are given.

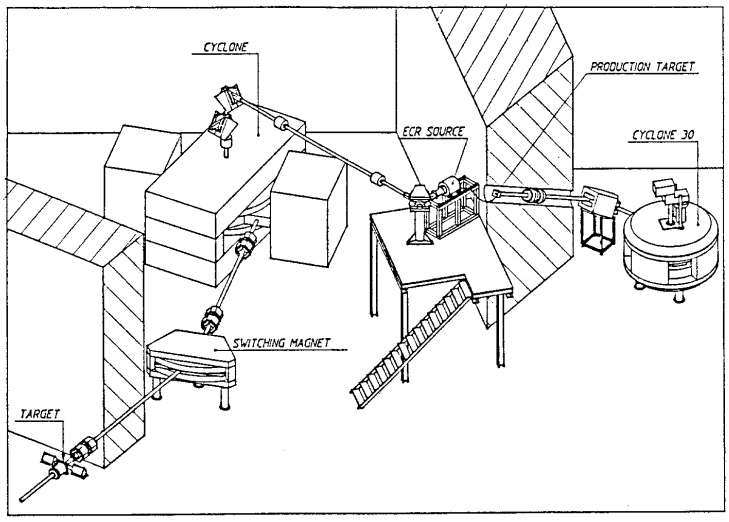

Figure 3.1: *Layout of the two cyclotrons at the Louvain-la-Neuve Radioactive Ion Beams Facility.*

Isotope	$T_{1/2}$ (s)	Production Target	E_{max} (MeV)	Intensity (pps)
$^{6}He^{+}$	0.8	LiF	18	3×10^{6}
$^{11}C^{+}$	1200	BN	10	1×10^{7}
$^{13}N^{+}$	600	^{13}C	8.5	2×10^{8}
$^{13}N^{2+}$	600	^{13}C	34	1×10^{8}
$^{13}N^{3+}$	600	^{13}C	76	3×10^{7}
$^{18}Ne^{3+}$	1.7	LiF	55	4×10^{5}
$^{19}Ne^{2+}$	17	LiF	23	5×10^{8}
$^{19}Ne^{4+}$	17	LiF	93	2×10^{8}
$^{35}Ar^{5+}$	1.8	NaCl	79	1×10^{5}

Table 3.1: *Characteristics of the accelerated ion beams available at the ARENAS[3] facility.*

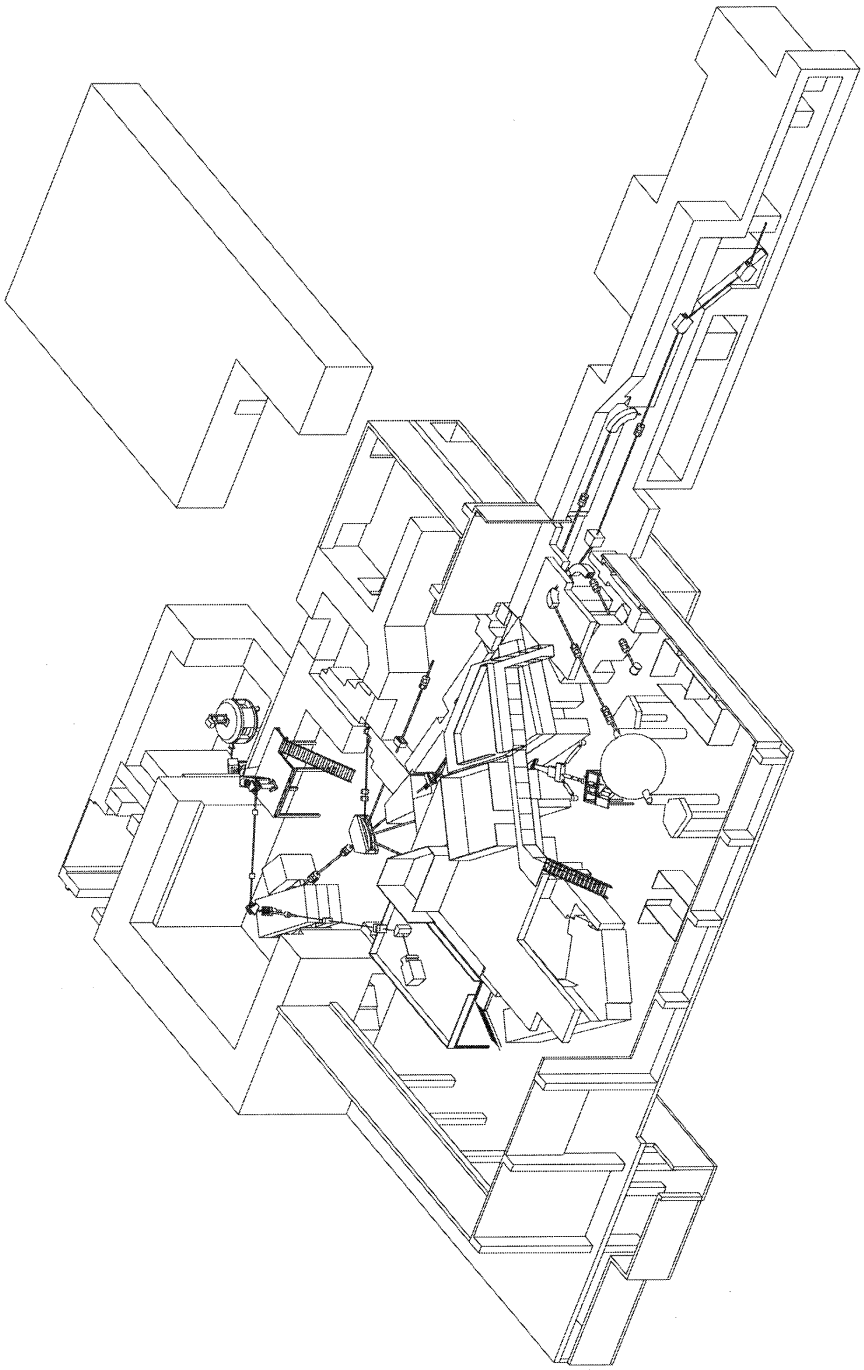

Figure 3.2: *General layout of the Louvain-la-Neuve Radioactive Ion Beams Facility.*

3.1.1 Production of ^{13}N RIB

The 30 MeV protons bombard a target made of ^{13}C pellets, obtained from 99% enriched ^{13}C powder graphitised under high temperatures and pressures, and embedded into a natural graphite rod in good thermal contact with a water cooled copper cylinder [Dec92]. Large amounts of ^{13}N are produced through the ^{13}C(p,n)^{13}N reaction. For 30 MeV protons impinging on a thick ^{13}C target ($\sim$1g/cm^2) the yield is $Y = 1.6 \times 10^{-3}$ ^{13}N nuclei per incident proton [Dar90]. The ^{13}N activity is extracted from these targets as ^{13}N-^{14}N molecules using a small nitrogen gas flow. The ^{13}N-^{14}N molecules are transferred to a single stage electron cyclotron resonance (ECR) ion source.

The experiment described in this thesis required a 45 MeV beam. To achieve such a high energy the 3^+ charge state was required (see table 3.1). This represented the first time such a high charge state had been used in a nuclear physics experiment and could thus be seen as part of the beam development project at the laboratory [Gal95].

The extraction efficiency of ^{13}N from the ^{13}C production target is independent of the charge state with an efficiency normally of ϵ_{extr} = 20-30%. Ionisation efficiency ϵ_{ion} for 3^+ is $< 3\%$ as compared to $< 20\%$ for 1^+ charge state. Acceleration efficiency ϵ_{acc} is $< 3\%$ and slightly better for 3^+ than for 1^+ due to the higher injection energy of the former.

3.2 Detection system

3.2.1 Introduction

Silicon p-n junction diodes have been used for more than thirty years to detect ionising radiation. The advantages of silicon as a detection medium are the low

band gap at room temperatures (∼1.1 eV) and very high charge carrier life times and mobilities of electrons and holes. This means that silicon detectors have excellent noise and timing characteristics and exhibit very uniform response with respect to the amount and type of radiation [Hal94].

Over the last few years techniques developed by the semiconductor industry have meant that it is now possible to create large numbers of p-n junction diodes on a single silicon wafer. These detectors have become known as silicon strip detectors. Figure 3.3 shows the outline of a typical p^+-n junction detector with a

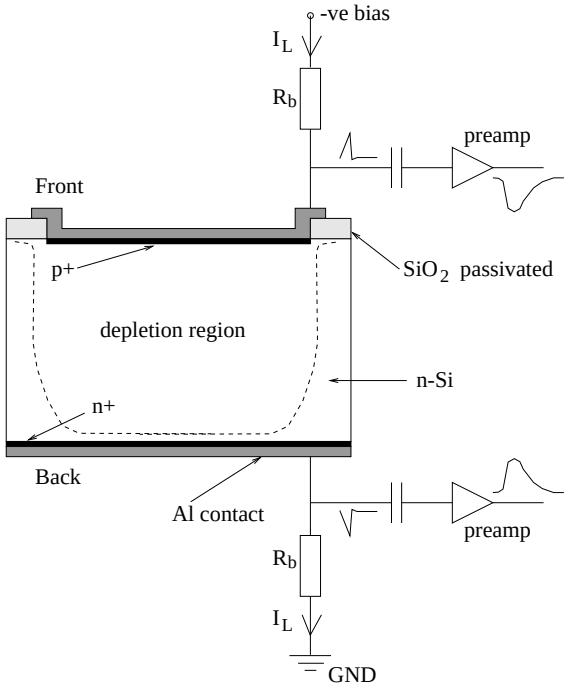

Figure 3.3: *Details of a basic p^+-n junction silicon detector*

layer of p^+ donor boron ions implanted onto the front surface region of the n-type silicon. Negative bias is applied to each p^+ region via the aluminium contacts which produces a depletion region in the bulk of the silicon. Detectors are often operated at several times the depletion bias voltage to effectively deplete the entire volume of silicon. The small inter-strip separation minimises the dead area on the detector surface. This dead area is passivated, i.e. it has been oxidised at very

high temperatures which minimises the leakage current between strips.

The Edinburgh group has been at the forefront of silicon strip detector applications in nuclear physics experiments. In proton radioactivity experiments 96 channel silicon strip detectors, providing pixel information on the scale of 0.30μm$\times 0.30\mu$m, have been used [Sel92, Liv93]. As a continuation of this work the Louvain-Edinburgh Detector Array was developed for work with radioactive beams.

3.2.2 Louvain Edinburgh Detector Array, LEDA

The Louvain-Edinburgh Detector Array, LEDA, is an annular silicon strip detector fabricated by Micron Semiconductor Ltd. [Mic]. It consists of 128 p^+ silicon strips on the front face, divided into eight sectors of sixteen strips, as shown in the schematic in figure 3.4 and the photograph in figure 3.5. For every sector

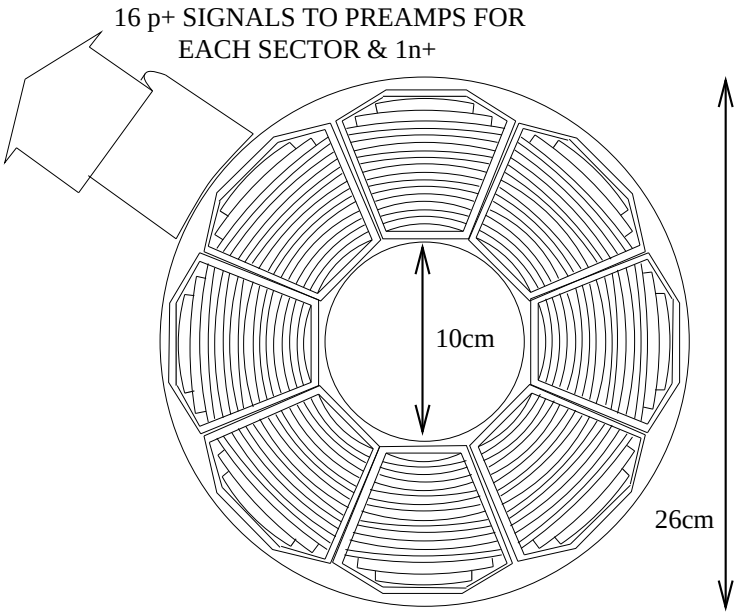

Figure 3.4: *Schematic of the Louvain-Edinburgh Detector Array, LEDA.*

there is a single large area n^+ pad on the back face. LEDA has an inner radius of 5cm and an outer radius of 13cm.

LEDA was designed so that it would cover a large solid angle to compensate for the low beam currents available from RIB. For a detector to target distance of 20cm LEDA covers ~9% of the total solid angle. As will be shown later in this chapter β particles from the natural decay of the beam deposit a maximum of ~ 1 MeV in the the 300μm of silicon. Thus the background is away from the region of interest which is discused in chapter 4. With the high degree of segmentation events of interest will be distinguished from the large background. The properties of LEDA are summarised in tables 3.2 and 3.3.

Active area	$\sim$ 56cm^2
Thickness	300μm
Front face	16 p$^+$ strips
Back face	1 n$^+$ pad
Strip width	5mm
Inter-strip distance	100μm
$\delta\theta$ for target-LEDA distance of 20cm	1^o
$\delta\phi$	see table 3.3
Energy resolution	$\sim$ 27 keV for alphas (see fig 3.6)

Table 3.2: *Summary of properties for a single LEDA sector.*

strip	$\delta\phi$
strip0 (outermost)	18^o
strip1	24^o
strip2	32^o
strips3-15	38^o

Table 3.3: *Azimuthal angle subtended by each strip from the beam axis. Strip0 has the largest radius and strip15 the smallest.*

Figure 3.6 shows an α-energy spectrum for the sum of all working strips gain-matched and offset corrected taken during the experiment with a three line α-

Figure 3.5: *Photograph of the Louvain-Edinburgh Detector Array.*

source revealing an alpha resolution of 27 keV. This is consistent with the expected value, σ_{exp}, given by the equation [Kem80];

$$\sigma_{exp} = \sqrt{\sigma_e^2 + (\Delta E_s)^2}$$

where σ_e is the electronic noise typically $\sim$23 keV, obtained from pulser spectra (see figure 3.7), and ΔE_s is the straggling of the α particles, given by $\Delta E_s = 25\sqrt{\Delta x}$, in the aluminium window of thickness Δx (μm) [Kem80].

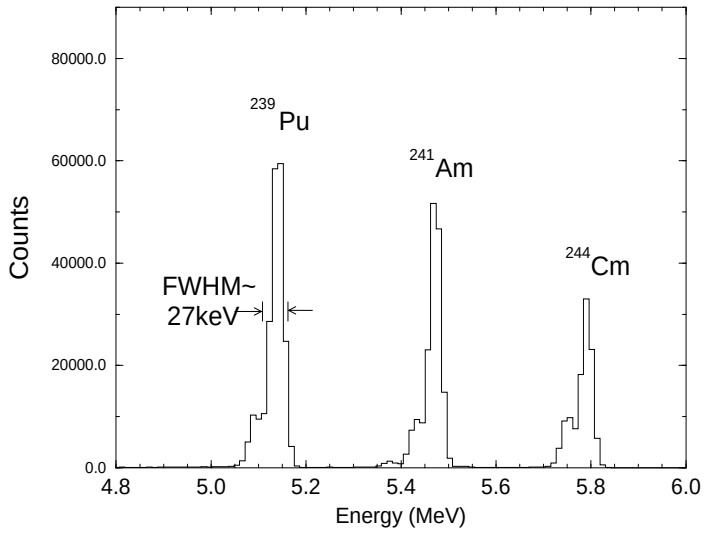

Figure 3.6: *Sum of gain-matched and offset corrected α energy spectra for all working LEDA strips using a three line α-source (^{239}Pu, ^{241}Am, ^{244}Cm).*

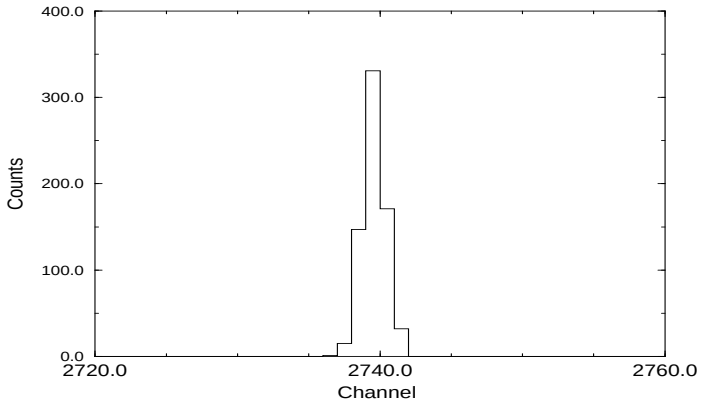

Figure 3.7: *Typical pulser spectrum for a single channel using a BNC PB-4 precision pulser. FWHM is* $\sim$ *2 channels which is equivalent to 23 keV.*

3.3 The commissioning experiment

The experiments described in this thesis were all performed at the Radioactive Ion Beams Facility in Louvain-la-Neuve, Belgium. This section describes the experimental setup for commissioning run which took place in February 1994.

It is essential to describe the results and conclusions which were obtained in order to understand the experimental changes made for the follow-up experiment, described in section 3.4.

3.3.1 General setup for commissioning experiment

A side view of the the experimental vacuum chamber is shown in figure 3.8. The LEDA detector was held on mounts attached to the inside of the chamber door. The target wheel was 16.5cm in diameter and could hold up to 12 different targets. The target to detector distance was adjusted from outside the chamber. During the run this was kept at 22.4cm thus covering an angular range of θ=13-30^o.

During the run an aluminium foil of 11.7mg/cm^2 protected the detector by stopping the heavy ions. It worked over a range of different target-detector distances.

The mount which housed this foil was designed, as part of this thesis project, to function over the range of target-detector distances of 20-30cm The foil could be replaced by a thick aluminium plate for additional protection whenever the beam was being tuned.

A 1.45mg/cm^2 CH_2 foil could be inserted externally into the beam line .9m from the target to degrade the beam energy.

The chamber was aligned using a laser placed several metres up the beam line.

The ^{13}N radioactive beam had a diameter of $\sim$7mm which was collimated using the system shown in figure 3.9. For this experiment C1, C2 and C3 were 17, 7 and 10mm respectively. C4 was the collimator on the target wheel from which current could be read and was used for beam optimisation.

A total of seventeen signals were taken from each sector; sixteen p^+ and one from the n^+ pad. These signals were connected by short 34-way cables and vacuum feed-throughs to the preamplifiers on the outside of the chamber door.

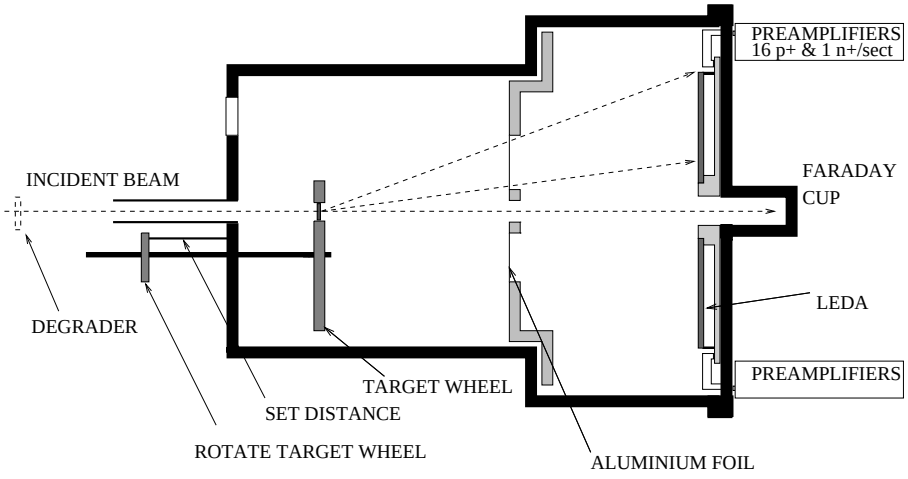

Figure 3.8: *Schematic side view of experimental chamber used in the commissioning run.*

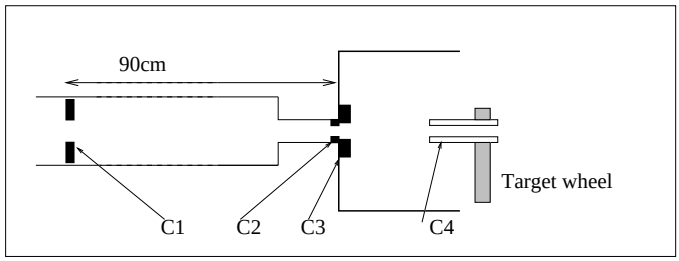

Figure 3.9: *Layout of the different collimators along the beam line.*

3.3.2 Preamplifiers

The preamplifier is the first stage in the chain of data processing electronics connected to the detector. In general the physical event in the detector will release an amount of charge proportional to the deposited energy of the particle. The preamplifiers used in this experiment were designed by the Edinburgh group in collaboration with Rutherford Appleton Laboratory (RAL) specifically for strip detector applications [Dav90]. They are charge sensitive and have a compact modular design which can be fitted onto a motherboard making extremely compact multi-channel preamplifier units.

For this experiment the preamplifiers were mounted onto the back of the chamber door in aluminium boxes, shown in figure 3.10 with lids removed. Each of the total of eight boxes contained a single motherboard which provided preamplification for the 16 p^+ and 1 n^+ signals of a sector. These signals were fed along 8×34 way twisted pair cables (15 metres long and doubly shielded) up to the junction boards in the electronics cabin that sat above the experimental area. The junction boards split the 34-way cables into 2×16-way which were fed into the amplifiers.

Figure 3.10: *Photograph showing the eight preamplifier boxes attached to the back of the experimental chamber door.*

3.3.3 Shaping amplifiers

The shaping amplifiers modules were also designed by Edinburgh/RAL [Tho90]. A single module contains eight high density cards each bearing a shaping amplifier and discriminator circuit, and each with its own pole-zero and offset adjustment. Shaping times are preset at 0.5μs; the common discriminator thresholds are determined by a single potentiometer for all eight channels and the gains are set by selecting the appropriate resistor pack. The full range for the amplifiers was set at 20 MeV using 22Ω resistor packs. Analogue and logic outputs were provided on sets of 16-way IDC headers for connection to ribbon cables.

3.3.4 Edinburgh Coincidence Unit (ECU)

Particles are identified using time-of-flight versus energy spectra as described in section 3.3.8 and 3.5. For particle-particle coincidence experiments it is necessary to have timing information for each detector in order to identify particles and to measure the time difference between hits. LEDA consists of 128 strips and at the time of the original proposal [Woo93] it was impossible to instrument such a large number with TDC's. The solution was to have one TDC per sector and one for each ring making a total of 24 channels. Thus for every ADC hit two TDC's would fire giving co-ordinates in the form $(sector, strip)$. The signal for the sector TDC's was trivial to set up but the ring TDC required the design of a new electronic module.

As part of this thesis project it was necessary to design, build and test such a module. The basic function of the ECU is shown in figure 3.11 and figure 3.12 shows a photograph of the module. It takes the 128 logic signals from the amplifiers and routes the signals to produce a wire OR of each ring. It consists of two boards connected by a 34-way cable. ECU was designed to be CAMAC

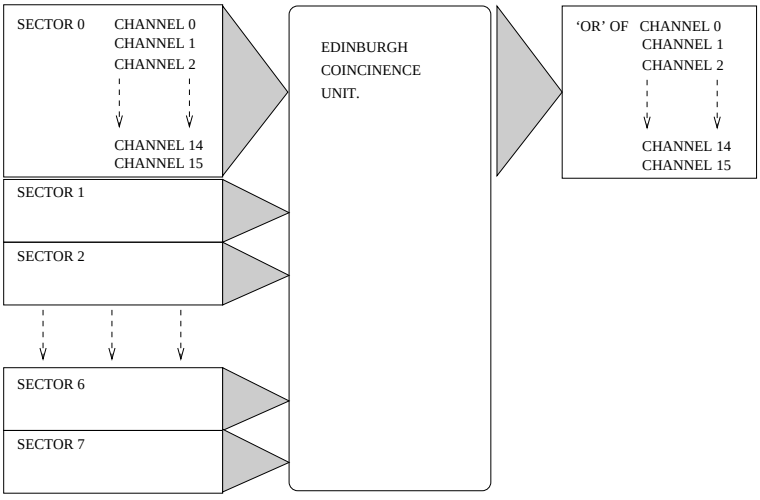

Figure 3.11: *Schematic diagram of the Edinburgh Coincidence Unit.*

compatible so that it could easily be incorporated alongside the standard logic

configuration.

The printed circuit board layout was designed using a commercial computer aided design package called P-CAD. This package allows the user to position copper traces, pads and holes on the screen. It can handle multi-layer boards, design of special components, insertion of text along with many other features. The final design can be plotted out for visual checking. The disk file containing the details of all the layers is then supplied to the manufacturing subcontractor, who uses a computer driven photoplotter to directly generate the photo masks for the board.

The ECU used two copper layers, front and back, and gold contacts for the power supplies. Manufacture was carried out by a local company, Zot Engineering Ltd. [Zot]. Initially a prototype was ordered and fully constructed, small faults were detected in the design which were corrected for the second module. The second module worked well and has been used for the two runs. Technical details of the ECU are given in appendix A.

The next section describes how the unit was integrated into the logic configuration.

3.3.5 Configuration of electronics

Figure 3.15 shows a block diagram of the electronics used in the commissioning experiment.

Analog signals from the amplifiers for the 128 p^+ strips and 8 n^+ pads were sent directly to the ADC's in the CAMAC crate. The 24 TDC channels were divided up into 3 LeCroy CAMAC TDC modules. The ECL logic from the amplifiers was split into three. One set of signals was delayed by 300ns and sent into the ECU resulting in an OR of the rings (as described in secton 3.3.4). These were then connected to the inputs of two LeCroy TDC's. The second set of signals

Figure 3.12: *Photograph of the Edinburgh Coincidence Unit.*

was delayed by 200ns and connected to the MALU's (Majority Logic Units). The MALU's produce a charge for each logic pulse and, thus, the discriminator could be used as hardware multiplicity selector. The final set of signals went into two LeCroy 4564 logic units which OR each sector. These were again fanned out with one set for the sector TDC's and the other an OR of all strips used as the gate for the MALU's.

The trigger for the ADC's was the coincidence between the MALU discriminator output (any p^+ hit for multiplicity equal to one) and the high frequency (HF) signal from the cyclotron. For a $^{13}N^{3+}$ beam of 45 MeV this HF has a period of 75ns. The AND condition selects every other pulse. The trigger was delayed and stretched using quad timers (QT) so that the ADC gate was 2μs wide as shown in figure 3.13.

Figure 3.14 shows how the timing information was read. An output register in the CAMAC crate resets the latch when the event has been read.

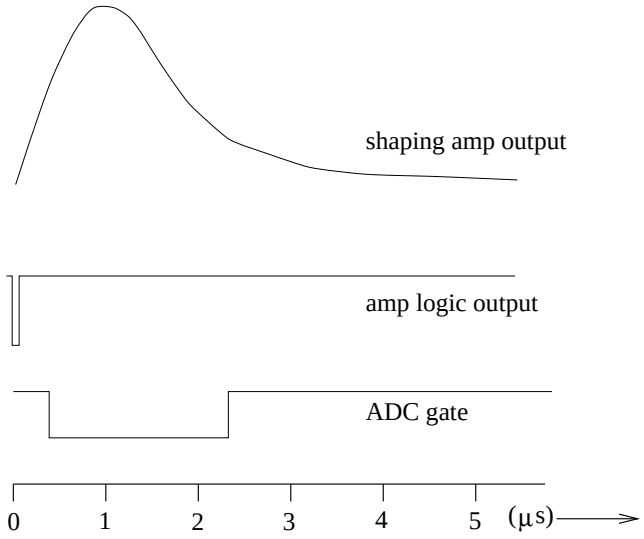

Figure 3.13: *Output shapes from amplifier and ADC gate.*

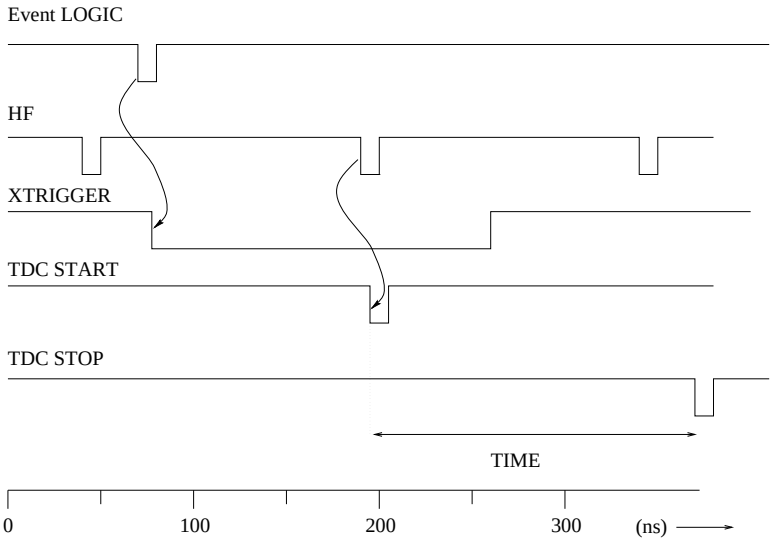

Figure 3.14: *Timing logic showing the TDC start signals based on coincidence with high frequency signal from cyclotron.*

3.3.6 Data acquisition

A schematic of the data acquisition system is shown in figure 3.16. The CAMAC crate contains:

- 17 Silena ADC's - 16 for the p^+ strips and 1 for the n^+ pads.
- 2 $\times$ LeCroy 2228A TDCs for the ring signals and 1 $\times$ LeCroy 4208 TDC for the sector signals.

Data from the TDC's and ADC's is collected by the VCC2117/B CAMAC crate controller which buffers the events. Once a block has been filled it is copied and sent to the CPU's (MVME167) in the VME crate via VICBUS standard connection. The acquisition software is implemented as a device and the tape process reads blocks from this device and writes them to tape. The RAM in the VME crate stores on-line spectra and the monitoring program writes the blocks to the PC where spectra can be viewed.

The dead time of the system depends on the the intensity of the beam which can vary significantly over a period of time. The pulser runs constantly during the

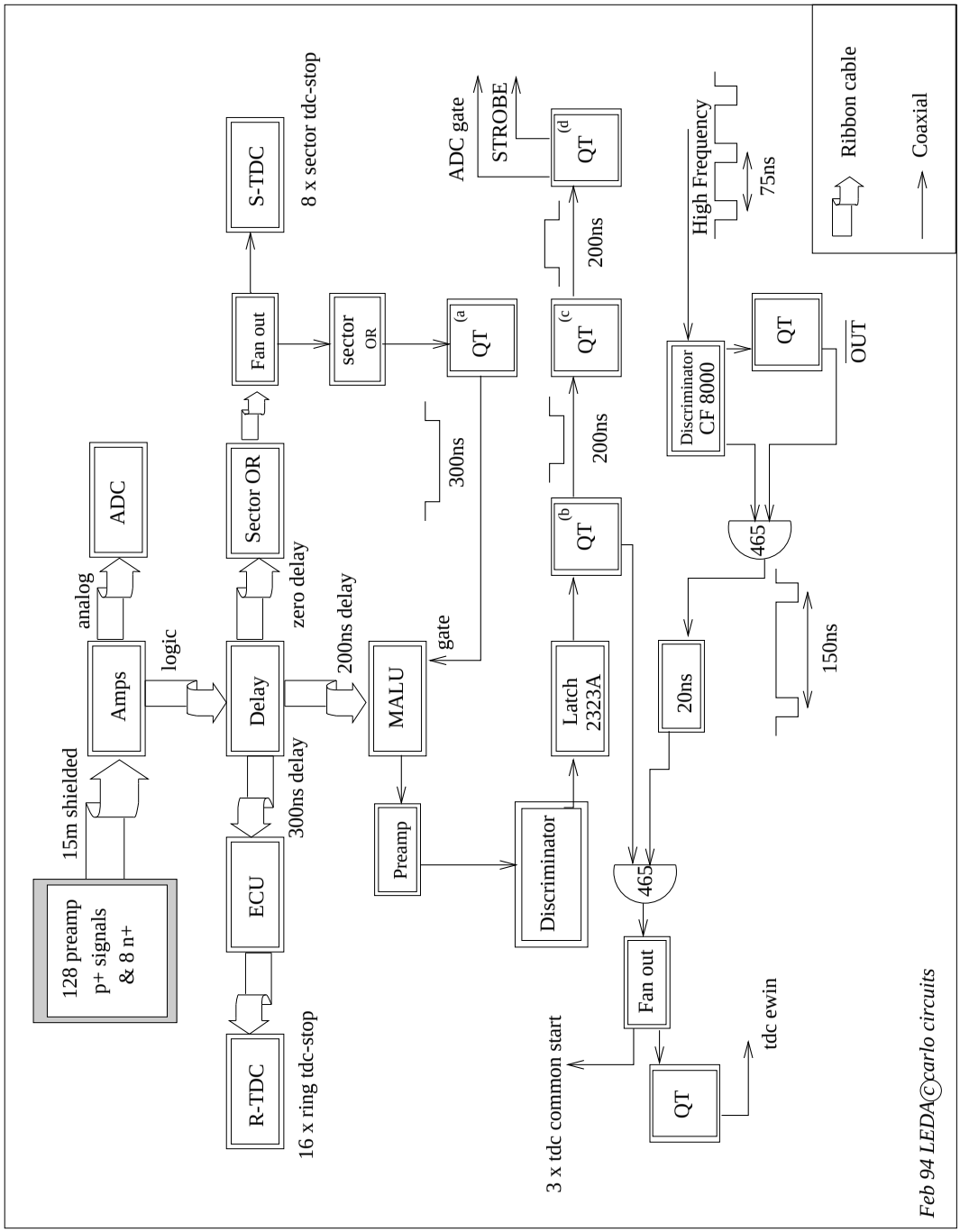

Figure 3.15: *Block diagram showing the layout of the electronics.*

experiment at the lowest setting. The dead time can be calculated for each run by comparing the actual number of pulser events and the number which would be expected. The dead time varied from 10-20%.

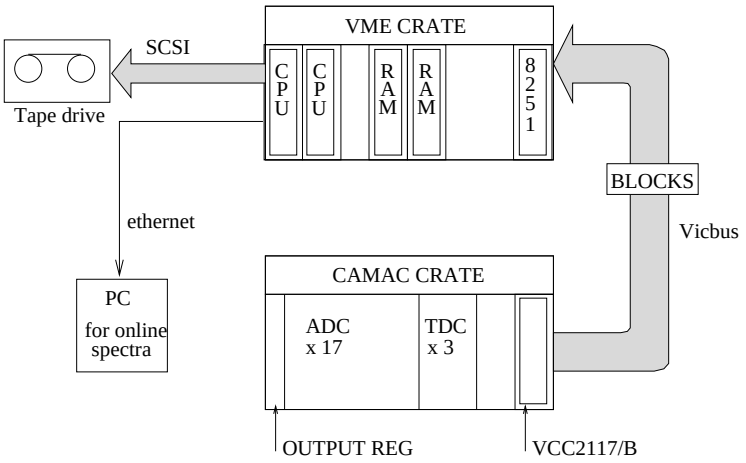

Figure 3.16: *Block diagram showing the layout of the acquisition system.*

3.3.7 Running the experiment

Prior to the experiment all preamplifiers and amplifiers were tested using the pulser. LEDA was tested with an α-source in the target position, running the acquisition system and checking the hit pattern. Figure 3.17 shows an example of the α-particle hit pattern for all 128 LEDA strips. Channels 0-15 correspond to sector 0, channels 16-31 to sector 1, etc. The solid angle effects can be seen clearly where the peak comes from the largest strip which is the fourth outermost (see figure 3.5).

A stable beam of 45 MeV $^{13}C^{3+}$ with the collimator in the target position was used to check that the beam profile was in the correct position. Current measurements from the collimator and the faraday cup were used by the engineers to fine tune the beam using vertical and horizontal steering magnets.

With the radioactive beam on the CH_2 target the timing delay from the HF was

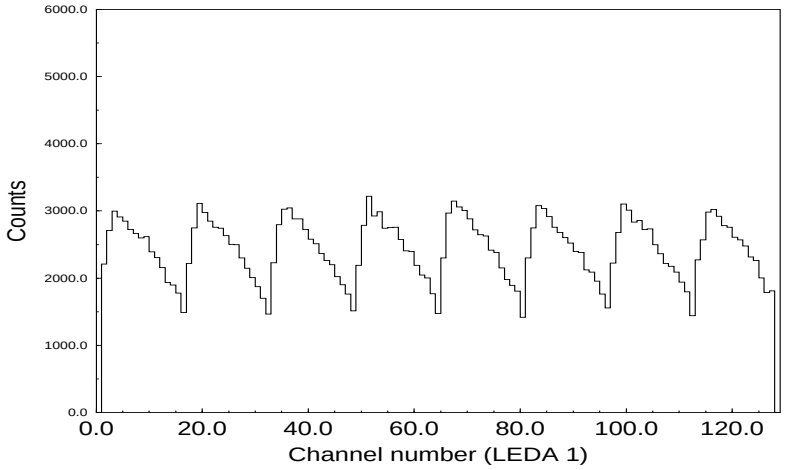

Figure 3.17: *α-particle hit pattern for the working strips in LEDA 1 with sets of 16 corresponding to each sector. Spectrum clearly shows the solid angle effects due to the different strip sizes.*

adjusted so that events from both pulses fell within the timing window.

The main run was on a CH_2 target with a number of control experiments also carried out. The control experiments were running with a ^{12}C target and running off-resonance by inserting a 1.45mg/cm^2 CH_2 foil into the beam line. The latter was the only viable option for beam degradation because once the beam energy was decided it could only be changed by shutting down the cyclotron and making modifications.

The amount of time and number of beam particles for the commissioning run is given in table 3.4.

3.3.8 Results of commissioning run

The results presented here can also be found in the proposal for the follow-up experiment submitted to the PAC in September 1994 [Woo94]. There is a certain degree of overlap between the results here and those for the second experiment. Thus matters such as particle identification and details of the behaviour of the

Commissioning experiment using single LEDA system			
Target	CH_2	Off-resonance CH_2	^{12}C
Thickness $\mu g/cm^2$	550	1450 + 550	200
Total ^{13}N incident • beam particles ($\times 10^{12}$)	4.1860	0.2708	0.8763
Total time (hrs.)	31.05	8.03	6.5

Table 3.4: *Summary of total beam for different targets for commissioning run.*
• *Estimated using average beam over period of time.*

elastically scattered protons can be found in the preliminary analysis of the data from the second run in section 3.5.

Figure 3.18 shows a typical time of flight versus energy plot for the sum of all strips in a single sector with a CH_2 target. The plot reveals the presence of α-particles, protons and the β background. A better example showing the clear separation between protons and alpha particles for the plot resulting from a single strip is given in section 3.5 figure 3.26. Particle identification is also discussed in the aforementioned section. The plot shows that the protons deposit a maximum of 6 MeV in the 300μm of silicon as discussed in 3.5 and that the two sets of pulses, separated by 75ns, are present because of the gate conditions.

The α channel is energetically closed for reactions on hydrogen so they must be generated by reactions with the carbon in the target. This is confirmed in a similar plot, shown in 3.19, obtained from the ^{12}C target data. What is noticeable is the significant level of protons observed from the ^{12}C target. The most likely origin of these protons is fusion-evaporation reactions since the incident energy of ^{13}N is well above the Coulomb barrier for a ^{12}C target.

Evaporation protons would have an average energy in excess of 10 MeV [Sie84] which would not be stopped by the 300μm thick LEDA detector. This explanation is confirmed by the existence of a high number of proton-proton coincidence events both in the CH_2 and ^{12}C data. Figures 3.20 and 3.21 show energy-energy plots

for coincident protons for CH_2 and ^{12}C data respectively.

A comparison between the singles alphas and the coincidence protons observed from the two targets indicates that ~90% of the CH_2 proton-proton coincidence data are due to evaporation protons from ^{12}C induced reactions which in turn implies that only ~10% of events are due to H induced reactions.

Figure 3.22 shows a comparison of the CH_2 proton coincidence data, subtracted and normalised with respect to the ^{12}C data, and ^{12}C data both projected from an energy-energy plot onto the 45^o axis. The plot clearly shows an excess of events in the region between 2.2-3.8 MeV that is not reflected in the ^{12}C data. This excess of around 2500 events cannot be re-normalised away without causing a large deficit in the region below 2.0 MeV where the ^{12}C yield peaks. An analysis of random coincidences between adjacent beam pulses indicated that only 160 of these events were caused by randoms.

Figure 3.23 compares the normalised data with Monte Carlo simulations for ^2He and sequential emission (the simulations are discussed in chapter 4). The data are broadly consistent with the simulations.

Conclusion

The conclusions drawn were that a signal for two proton emission had been observed but that the large background precluded a detailed analysis of the mechanism. This background from fusion-evaporation protons (~ 10 MeV) along with elastically scattered protons of around 8 to 11 MeV would not be stopped by the 300μm thick LEDA detector and instead deposit a fraction of their energy as they punched through. The solution put forward for the follow-up experiment to minimise this background was to use;

• E-Veto detection system where the protons of interest would be stopped in the first detector and/or

• metal hydride targets (titanium and zirconium). The fused system would lie much further from the proton drip-line than with ^{12}C and thus increase the dominance of the neutron evaporation channels.

The next section describes the E-Veto detection system which, using a CH_2 target, proved to have a large enough effect on the background that the metal hydride targets were not needed. Details of these metal hydride targets are given in appendix B.2.

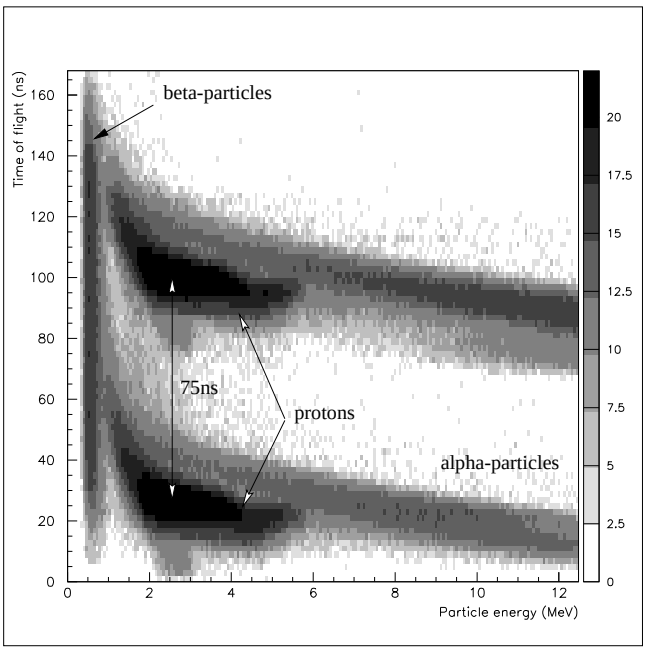

Figure 3.18: *Time of flight plot for CH_2 data for the sum of all strips in sector 4.*

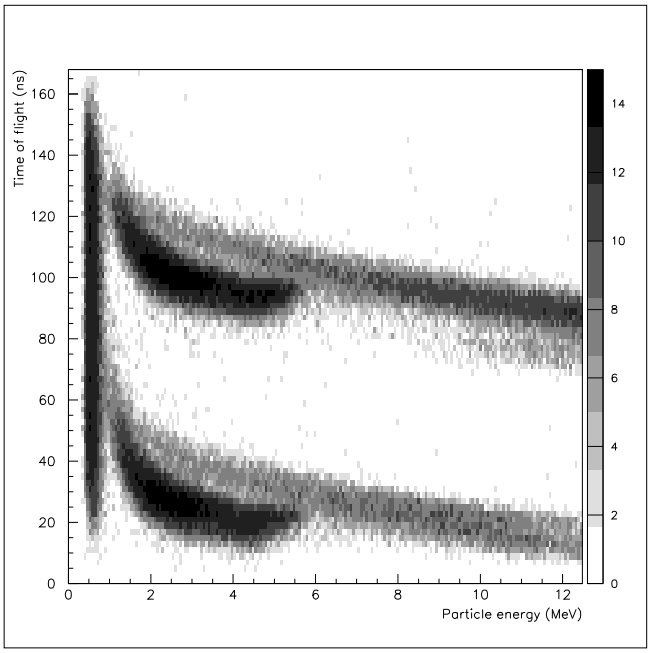

Figure 3.19: *Time of flight plot for ^{12}C data for the sum of all strips in sector 4.*

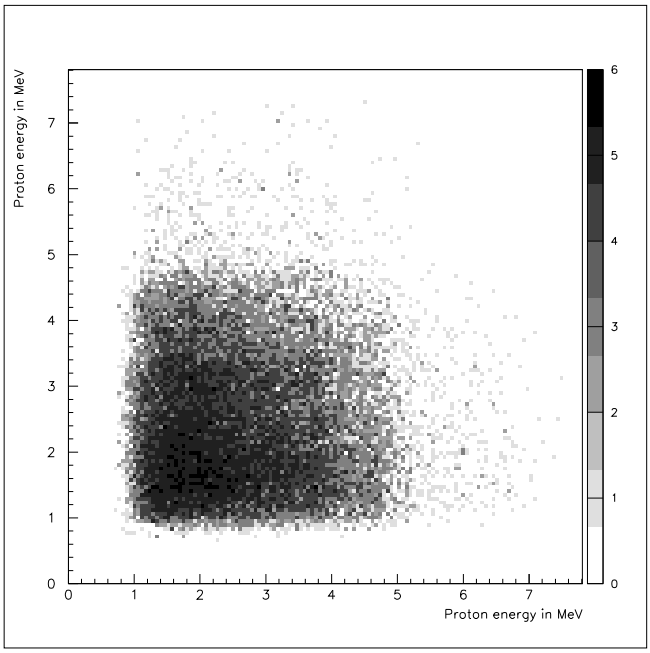

Figure 3.20: *Proton energy-energy plot for CH_2 data.*

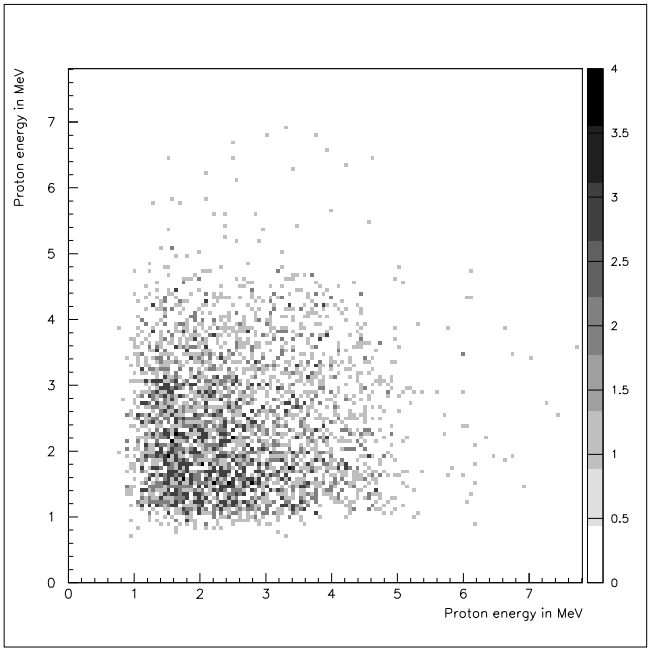

Figure 3.21: *Proton energy-energy plot for ^{12}C data.*

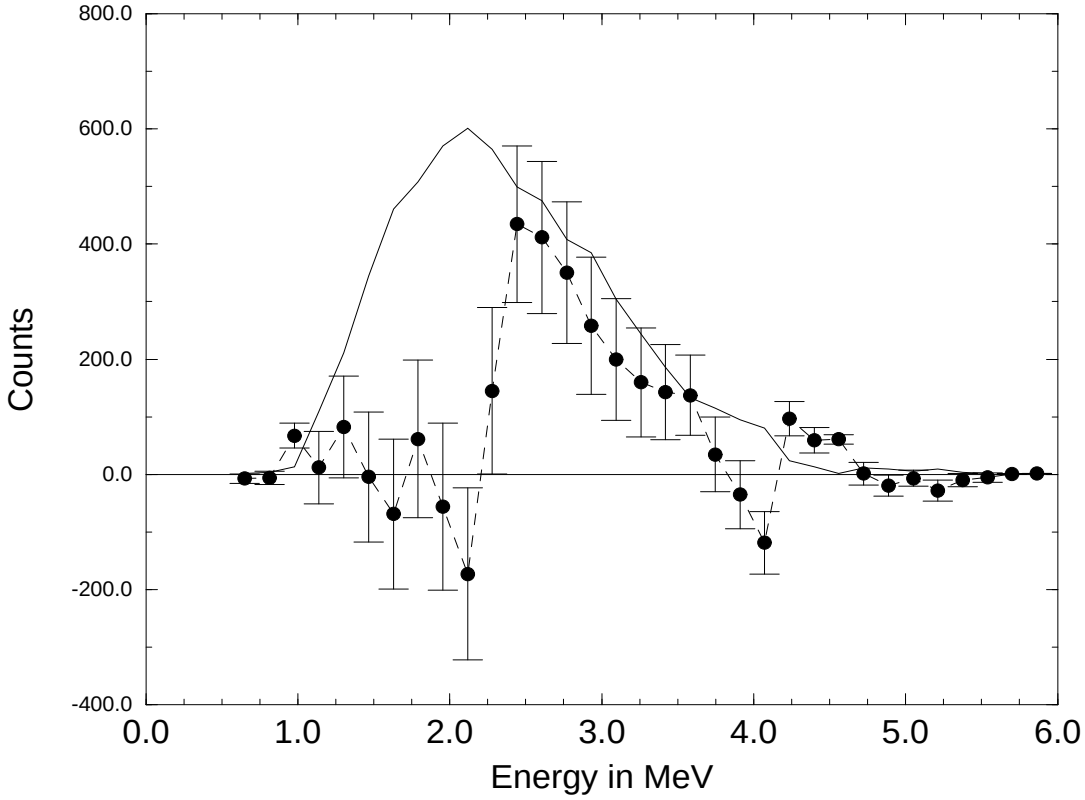

Figure 3.22: *Coincidence proton spectra projected onto 45° axis of energy-energy plots. The dashed line shows the CH_2 data with ^{12}C subtracted normalised with respect to the alphas. Solid line is for ^{12}C target.*

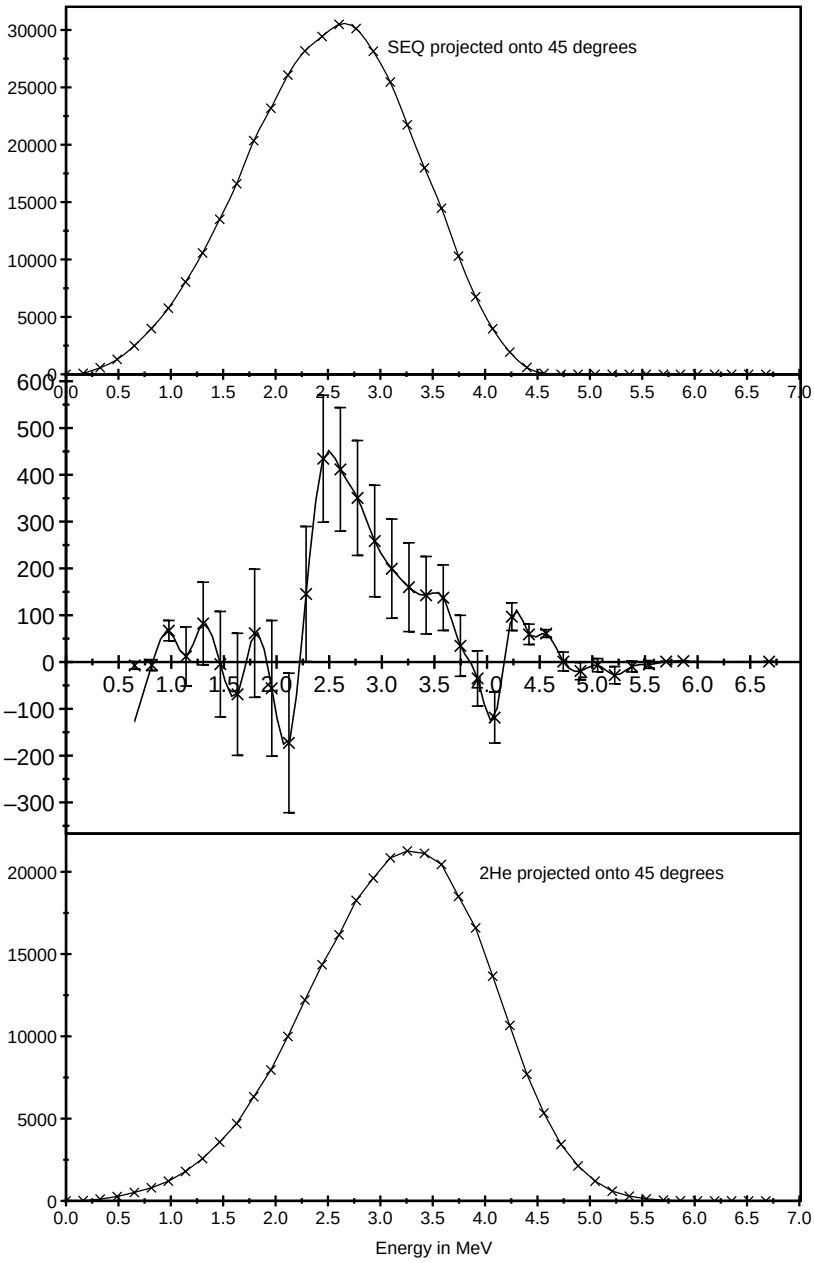

Figure 3.23: *Projection onto 45° for (a) simulation for sequential decay and (c) ^{2}He emission and (b) is the excess CH_2 counts.*

3.4 General setup for follow-up experiment

A side view of the the experimental vacuum chamber is shown in figure 3.24 with the two LEDA detectors at the heart of the system. LEDA 2 was attached to the inside of the chamber door and LEDA 1 held in position 2.5cm apart using mounts designed specifically for this thesis experiment. LEDA 2 is the same as that used in the first experiment.

The protons of interest in this experiment, as discussed in sections 4.2 and 4.3, will be stopped by the combination of the thicker 12.6mg/cm^2 aluminium foil and the 300μm of LEDA 1. The foil works over a larger range of target-detector distances than that in figure 3.8.

LEDA 2 acts as a large area veto to eliminate high energy protons that penetrate LEDA 1. As can be seen from the geometry the outer strips have no veto. The thicknesses for each sector of LEDA 1 and operating voltages are given in table 3.5.

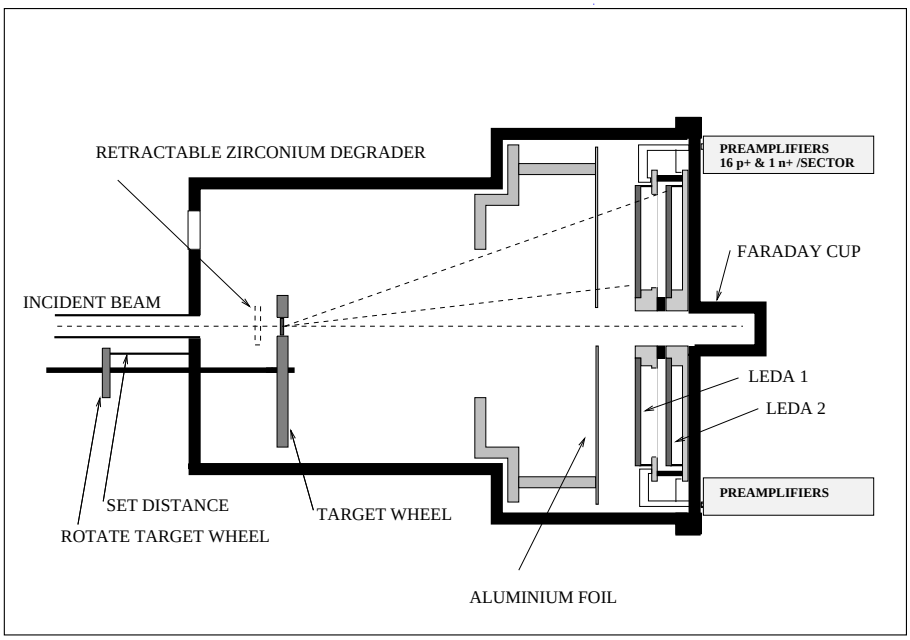

Figure 3.24: *Side view schematic of vacuum chamber used in follow-up run.*

The target to detector distance for the run was 22cm with LEDA 1 covering an angular range $\theta = 12.8^o - 30.5^o$.

The beam was degraded by inserting 1mg/cm^2 zirconium foil 2cm in front of the target by external means. With the previous degrading system a considerable fraction of the beam had been lost due to the degrader to target distance of 90cm.

LEDA 1 : front detector sectors								
	0	1	2	3	4	5	6	7
Serial: MSL-	1167-12	1188-3	1182-11	1188-13	1188-7	1167-20	1167-25	1182-12
Thickness (μm)	301	298	306	307	299	300	296	299
Bias voltage (-V)	60.3	58.0	62.2	56.1	60.3	75.1	60.3	62.3
Leakage current (-μA)	0.12	0.23	0.36	0.27	0.41	3.89	1.07	0.38

Table 3.5: *Summary of LEDA 1 sectors*

The beam current was measured using the faraday cup which was amplified by a factor of 1000 and read off an integrator located in the electronics cabin. The integrator was reset at the start of each run and stopped at the same time as the acquisition.

Again, a total of seventeen signals were taken from each sector; sixteen from the the front (LEDA 1) p^+, and one from the back (LEDA 2) n^+ pad. The same electronics were used as in the first run.

The final main difference between the two runs was in the logic which is shown in figure 3.25. The commissioning run showed that a hardware multiplicity trigger (using the MALU's) was not required and thus this was omitted from the second run. A rate divider was used to select every other pulse of the HF. The ECL logic from the amplifiers was split into two instead of three with one set for the ECU and the other the sector OR. The ADC and TDC gates were the same as those described in section 3.3.5.

The main run was on a CH_2 target with a number of control experiments also carried out. The control experiments were running off resonance by inserting the

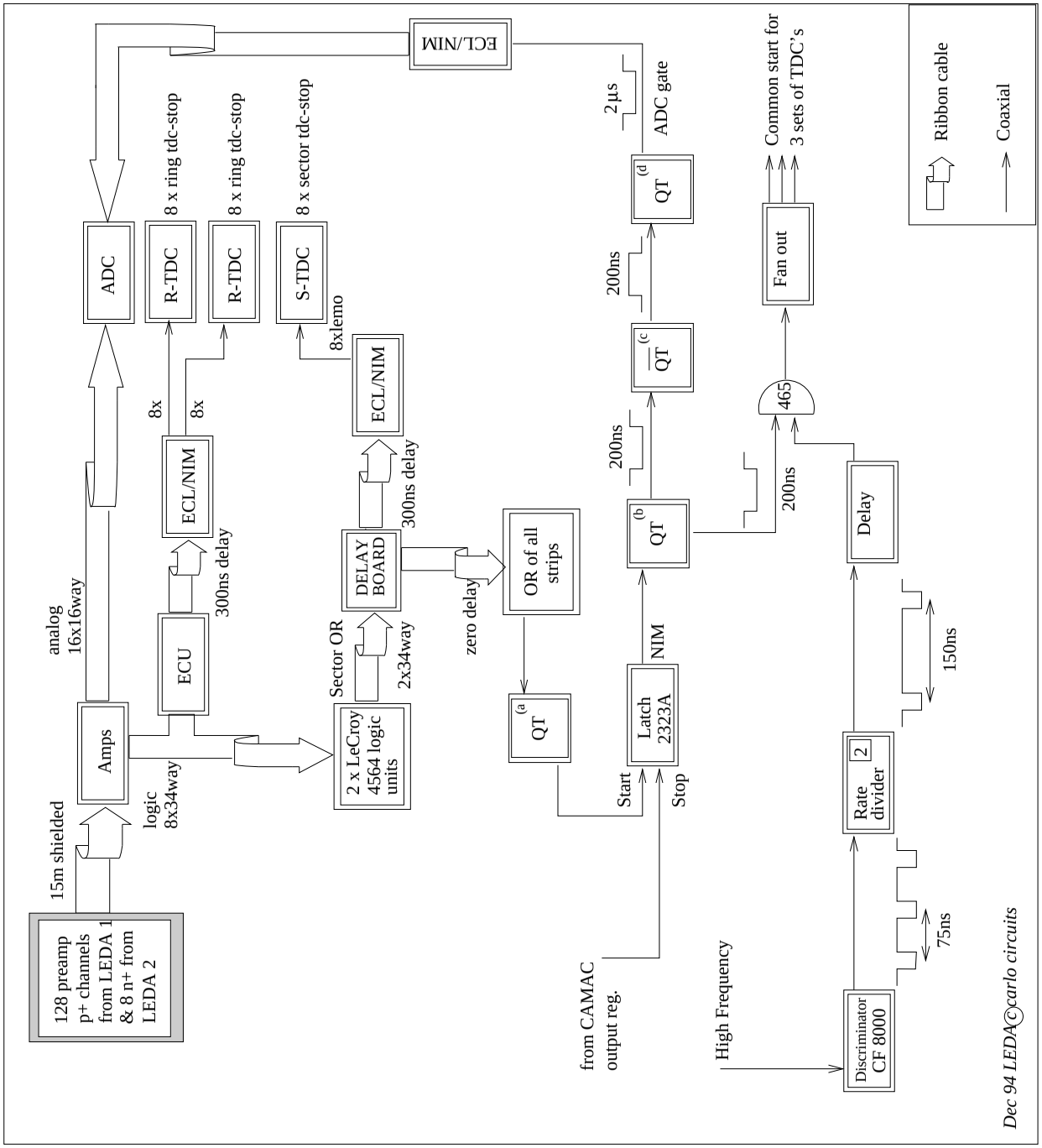

Figure 3.25: *Block diagram showing the layout of the electronics for the follow-up experiment.*

zirconium foil in front of the target, running with a ^{12}C target and a run with just the degrader foil in position and no target. The amount of time and number of beam particles for the second experimental run is given in table 3.6.

Second experiment using 2 × LEDA system				
Target	CH_2	Off-resonance CH_2	^{12}C	Zr degrader
Thickness $\mu g/cm^2$	540	Zr + 540	200	1000
Total ^{13}N incident † beam particles ($\times 10^{12}$)	1.4014	1.4814	1.3475	0.4774
Total time (hrs.)	5.87	5.90	6.25	2.05

Table 3.6: *Summary of total beam for different targets for follow-up experiment.* † *Measured from integrator for each run.*

3.5 Preliminary analysis of follow-up experiment

ADC channels 0 to 127 are the 128 p+ strips in LEDA 1 and ADC's 128 to 135 are the 8 n+ pads of LEDA 2. For each event in LEDA 1 the channel number is broken up into the form $(sector, ring)$. The sectors range from 0-7 and rings from 0-15 where ring(0) is the outermost and ring(15) the innermost. For the event to be accepted the two corresponding TDC channels must have fired. For multiplicity equal to two then 94% of events were found to fulfill this condition. If the particle is stopped in LEDA 1, i.e. there is no signal in the corresponding sector in LEDA 2, then the particle is identified.

Off-line analysis revealed that n^+ back plane veto for sector six did not respond and data from this sector have been omitted from the full analysis.

Figure 3.26 shows a typical time versus energy plot for a single strip where no veto was registered in the back detector. The spectrum reveals the presence of alpha particles and protons separated much better than in the corresponding case for the commissioning run (figure 3.18). Two beam pulses separated by 75ns

are recorded as described earlier in order to identify random coincidences. The β particles from the radioactive decay of the beam are present uniformly over time at low energies with a maximum energy of 1 MeV away from the region of interest. The protons deposit a maximum energy of 6 MeV as predicted by energy loss calculations [Arm73]. The ranges for different particles in silicon are summarised in table 3.7.

Particle	Maximum energy in LEDA 1	LEDA 1 & LEDA 2
proton	6 MeV	9 MeV
deuteron	8 MeV	12 MeV
alpha	24 MeV	36 MeV

Table 3.7: *Maximum energy deposited in LEDA 1 and in combination of LEDA 1 & LEDA 2 calculated for different particles.*

Windows such as the ones shown are set on the protons for all 128 strips in the front detector for off-line analysis.

Particles which punch through the first detector are plotted with energy in LEDA 2 against energy in LEDA 1 in figure 3.27. The back detector was not calibrated independently, hence, the energy calibration in the figure is based on the proton energy loss values given in table 3.7. Alpha particles, deuterons and protons can clearly be seen with a second fold back for particles which burst through both detectors. The high density proton grouping which penetrates both detectors corresponds to elastically scattered protons. These high energy protons lose a small amount of energy in the aluminium foil and deposit only a fraction in LEDA 1. For example at 12^o an 11.2 MeV proton losses 400 keV in the foil and deposits 2.6 MeV in LEDA 1.

In inverse kinematics the laboratory energy of the elastically scattered proton is

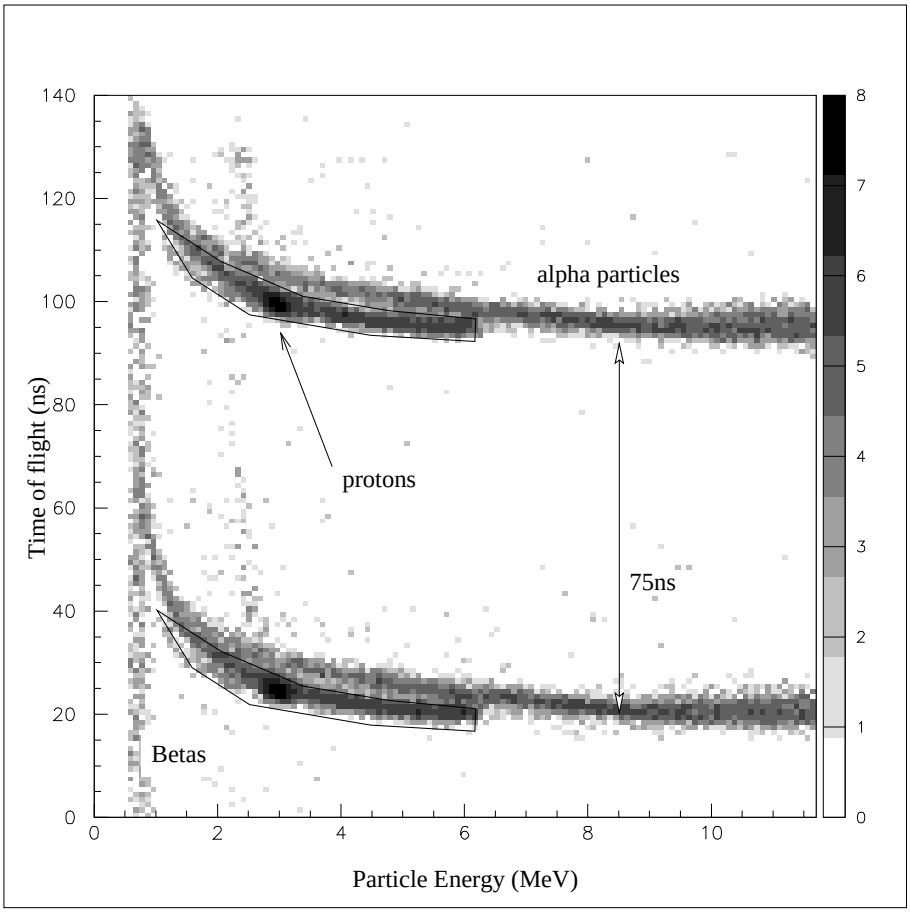

Figure 3.26: *Time versus energy plot for a single strip for events which leave no signal in LEDA 2. Protons, alphas and betas can clearly be distinguished and the figure shows typical proton windows which are set in the software for particle identification. Timing information is taken from the ring TDC.*

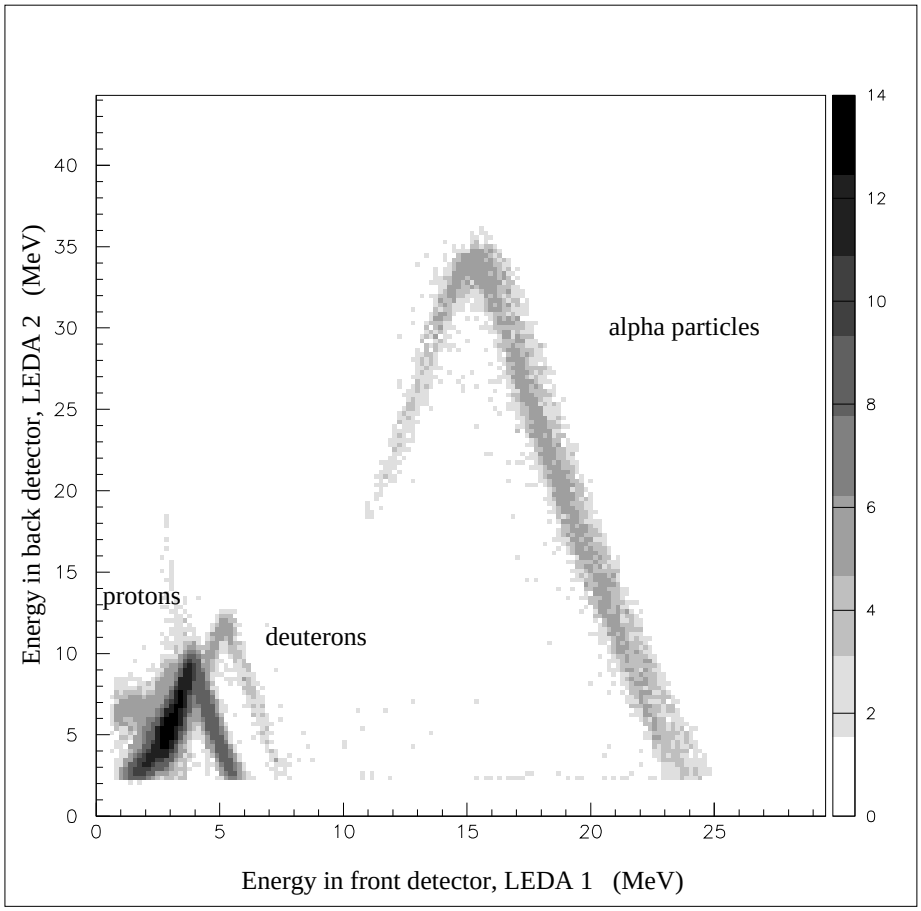

Figure 3.27: *Energy in LEDA 2 against energy in LEDA 1 for sum of all strips in sector 2 for multiplicity one events. Figure shows fold back for particles which are not stopped in either detector.*

given by,

$$E^{l}_{proton} = E_{projectile} \frac{4m_{projectile}}{(m_{projectile}+1)^2} \cos^2 \theta^{l}_{proton} \tag{3.2}$$

where $E_{projectile}$, $m_{projectile}$ are the projectile energy and mass, and θ^{l}_{proton} is the proton lab angle. The black circles in figure 3.28 represent the elastic proton peak against angle for on-resonance data. As the angle increases the protons have less energy, travel slower and, hence, deposit more energy in the detector. The solid line represents a simulation using equation(3.2) with energy loses in 12.6mg/cm^2 of aluminium foil and energy deposited in 307μm of silicon corresponding to sector 3 (see table 3.5) taken into consideration. The simulation uses a beam of energy, $E_{projectile} = 44$ MeV, corresponding to the centre of the target and it reproduces the data to a high degree of accuracy.

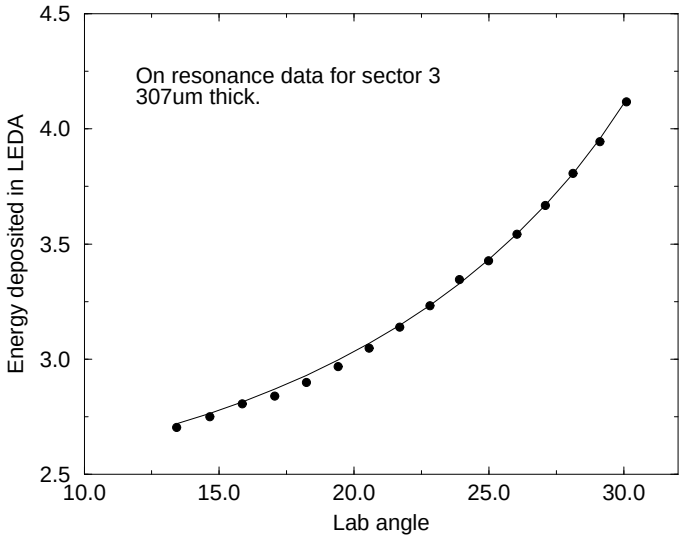

Figure 3.28: *Energy deposited by elastics in LEDA 1. Dark circles represents the data and the solid line the predicted amount using energy loss calculations with an incident beam of 44 MeV and the experimental conditions described in the text.*

The back detector does not veto all the high energy protons that punch through. This can be seen in figure 3.29 which shows the protons for each strip in sector

3. The dashed line represents any hit in LEDA 1 and is the source of the plot in figure 3.28, whereas the solid line is for a proton event that has no signal in the back detector. For the outer angles, strip(3,0) and strip(3,1), there is no veto due to the geometry of the detection system whereas the veto efficiency improves approaching the inner angles.

This veto efficiency is obtained by fitting the peaks with a gaussian with a flat background removed and is shown in figure 3.30 as a function of strip number. The efficiency is as expected with the outer strips, 0 and 1, having no veto and strips 2 to 4 not as efficient because the backing detector does not cover the same area as the front.

3.6 Summary

The results of the commissioning run have been discussed in detail leading to the conclusion that a signal for two proton emission had been observed but that the background was too large to identify the decay mechanism. The conclusions made from this led to a different setup for the follow-up experiment which has also been described. A number of features of the overall performance of this second run have been presented.

The aim of this follow-up experiment was to identify the decay mechanism for two protons emitted from the 7.77 MeV excited state in ^{14}O. The following chapter is devoted to a discussion of how the decay mechanisms have been simulated. A full analysis of the data and comparison with simulation is given in chapter 5.

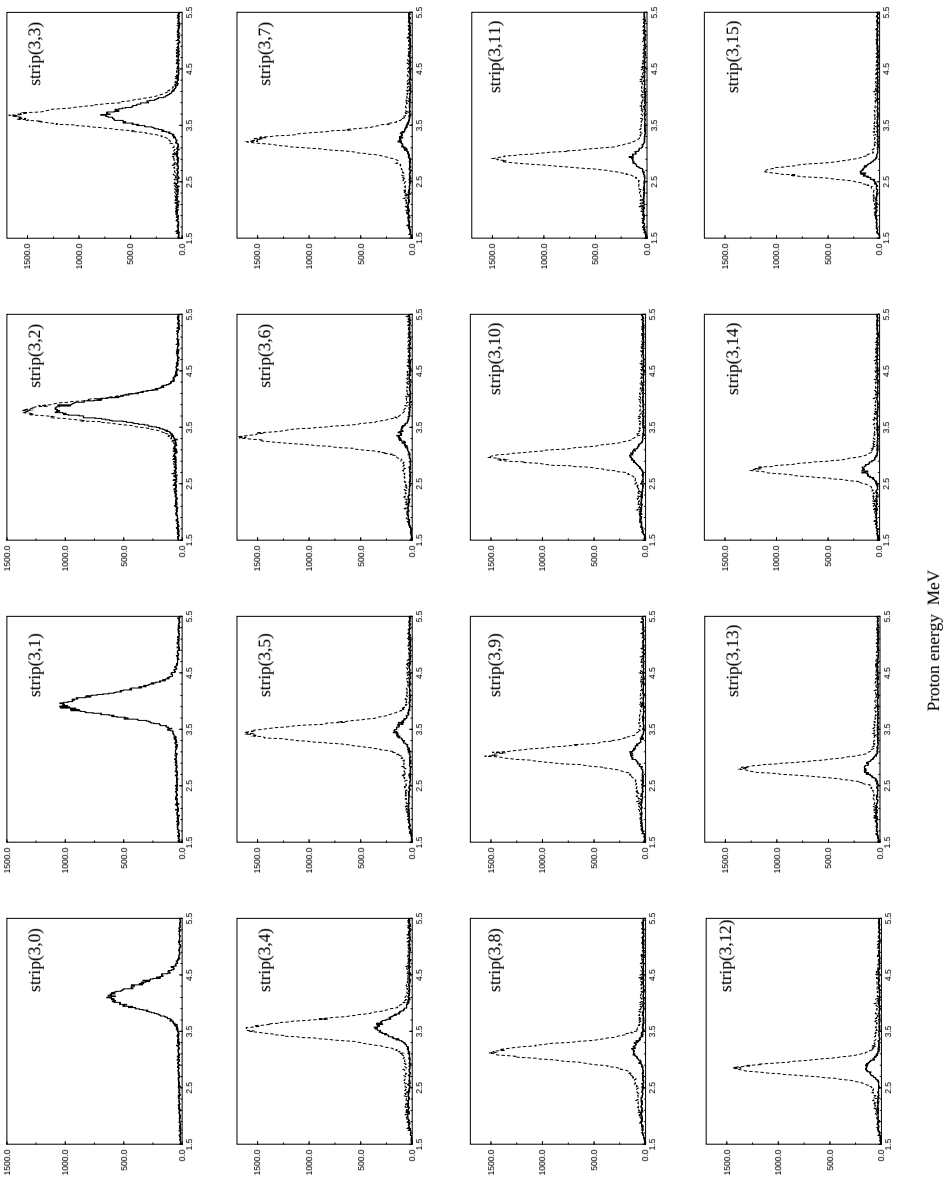

Figure 3.29: *Proton spectra for each strip in sector 3, strip(3,0) is the outermost and strip(15,0) the innermost. Dotted line represents protons which have hit front detector. The solid line requires that the protons do not hit the back detector. The spectra show how the high energy peak due to elastics increases with angle and that the high energy veto is not 100% since some are recorded in the vetoed data.*

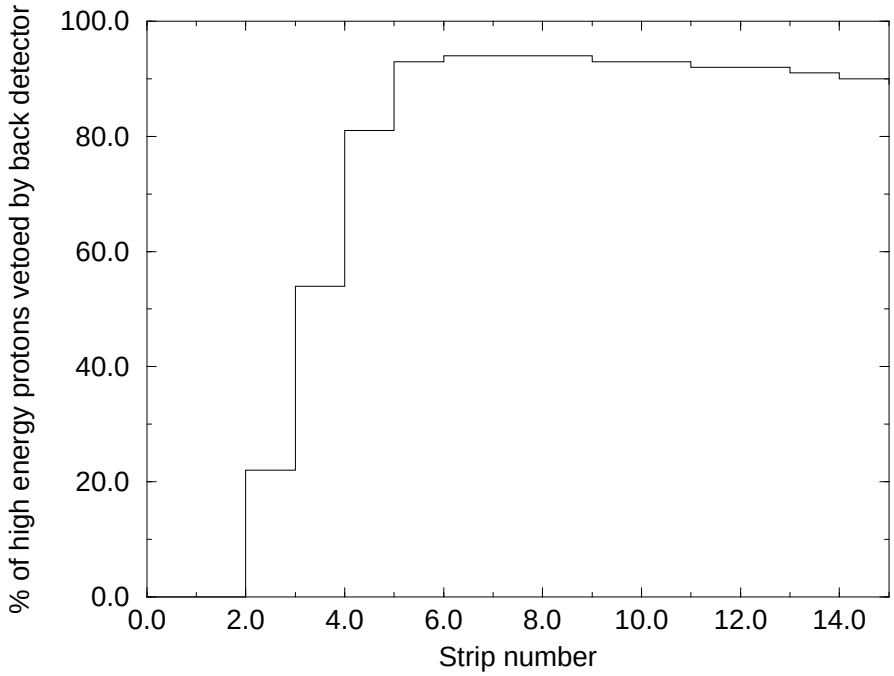

Figure 3.30: *Veto efficiency as a function of strip number were the efficiency is calculated from the number of high energy elastic protons that are vetoed by the back detector. Spectrum shows that the outer strips 0 and 1 have no veto because of the detector geometry.*

Chapter 4

Monte Carlo Simulation

The two proton decay mechanisms were simulated using a code called UNIMONTE which is an all purpose Monte Carlo breakup code [Mac].

The code was adapted to incorporate the LEDA detector and to simulate both sequential and ^{2}He emission. A large part of this thesis project has been to;

(i) Create a sophisticated model for ^{2}He emission containing FSI theory and the barrier penetrability discussed in sections 2.3.2 and 2.2 respectively.

(ii) Simulate sequential two proton emission.

(iii) Take account of the experimental conditions from section 3.4.

What follows is a general description of the code followed by details of how the different mechanisms were simulated giving sample spectra and, finally, tests for the code's robustness.

4.1 General features of UNIMONTE

4.1.1 Main code

The main code consists of three sections: input section, kinematic section and detector control.

In the input section the reaction is specified in the following form,

$$target(projectile, ejectile)$$

The simulation allows for the possibility of a recoil nucleus. However all the simulations which have been performed for this thesis project are for a single particle being produced in the reaction. Thus the kinematics discussed are for this case. The ejectile breaks up into two fragments which in turn can break up into, at most, two subfragments each;

$$ejectile \longrightarrow frag(1,0) + frag(2,0)$$

$$frag(1,0) \longrightarrow subfrag(1,1) + subfrag(1,2)$$

$$frag(2,0) \longrightarrow subfrag(2,1) + subfrag(2,2)$$

The input file also contains the beam energy, detector to target distance and the excitation energies and widths of any fragments which are not in their ground state. The reaction is H(^{13}N,^{14}O*) and the simulation studies the emission of two protons from the 7.77 MeV (Γ= 76 keV, J$^{\pi}$= 2^{+}) excited state in ^{14}O as discussed in section 1.3.

The kinematics section begins by taking a random point on the resonance, referred to as the excitation of the ejectile $E^{ex}_{ejectile}$. The code calculates where the beam was stopped in the target and, hence, the projectile lab energy, E^{l}_{p}. The notation is the same as that used in chapter 2 where c and l are centre of mass and laboratory frames respectively and subscripts p for projectile and t for the target.

The velocity of the centre of mass is given by

$$v^c = v_p^l(\frac{m_p}{m_p + m_t}) \tag{4.1}$$

where v_p^l is the projectile velocity

$$v_p^l = (\frac{2E_p^l}{m_p})^{\frac{1}{2}} \tag{4.2}$$

The total energy in the centre of mass is given by

$$E_{tot}^c = E_p^c + E_t^c = E_p^l(\frac{m_t}{m_p + m_t}) \tag{4.3}$$

The separation energy of the ejectile is calculated from

$$E_{ejectile}^{sep} = E_{ejectile}^{ex} + Q_{ejectile} - E_{frag(1,0)}^{ex} - E_{frag(2,0)}^{ex} \tag{4.4}$$

where $Q_{ejectile}$ is the the Q-value for the ground state reaction and the last two terms are the excitation energies of the two fragments. The ejectile breaks up into the two fragments with each sharing the energy inversely with respect to their mass,

$$E_{frag(1,0)}^c = E_{ejectile}^{sep}(\frac{m_{frag(2,0)}}{m_{frag(1,0)} + m_{frag(2,0)}}) \tag{4.5}$$

$$E_{frag(2,0)}^c = E_{ejectile}^{sep}(\frac{m_{frag(1,0)}}{m_{frag(1,0)} + m_{frag(2,0)}}) \tag{4.6}$$

The velocities of the fragments are given by

$$v_{frag(i,0)}^c = (\frac{2E_{frag(i,0)}^c}{m_{frag(i,0)}})^{\frac{1}{2}} \tag{4.7}$$

where i=1,2. The fragments are then scattered isotropically into 4π, unless otherwise specified, to give the three x, y, z velocity components. The laboratory velocities and energies are calculated from

$$\vec{v}_{frag(i,0)}^l = \vec{v}_{frag(i,0)}^l + \vec{v}^c \tag{4.8}$$

$$E_{frag(i,0)}^l = \frac{1}{2}m_{frag(i,0)}((v_x^l)^2 + (v_y^l)^2 + (v_z^l)^2)_{frag(i,0)} \tag{4.9}$$

Exactly the same decay procedure is applied to the decay of the fragments into subfragments.

The final section of the main code follows the trajectories of the particles to calculate their intersection with the plane of the detection system. Each event is described by the polar co-ordinates r and ϕ as shown in figure 4.1. The centre of this co-ordinate system corresponds to the centre of the LEDA detector and is on the beam axis. If a particle hits one of the strips the event is assigned $(sector, strip)$ information as well as retaining the precise angular information. The simulation accounts for the gaps between the sectors but not those between the strips which are considered to be negligible.

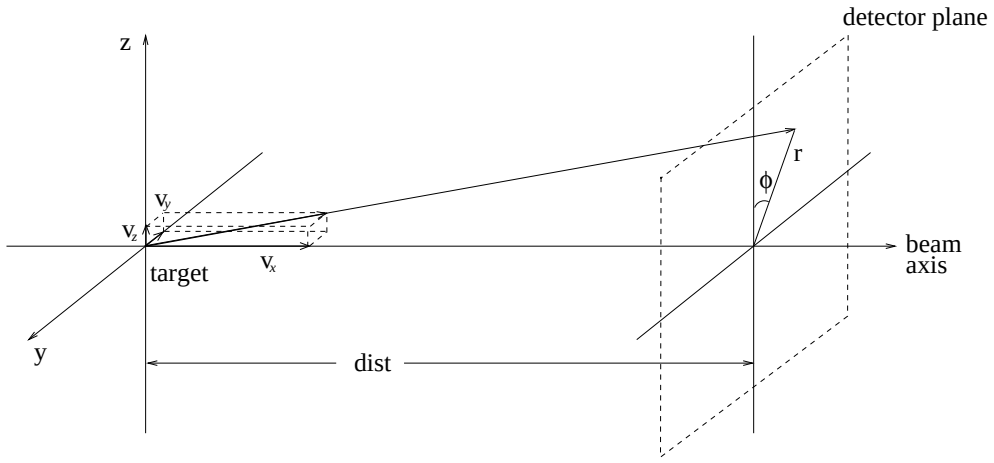

Figure 4.1: *Figure shows the velocity components of a particle and its intersection with the detector plane. Each event is give polar co-ordinates in the detection plane in the form r and ϕ.*

When two protons are detected in coincidence the event is dumped into the sort routine.

4.1.2 Sort routine

The sort routine has been designed to account for the experimental conditions described in section 3.4. Analysis of the experimental data provides limited angular information were we know which strip was hit but not where exactly on that strip. Thus, for each hit in the data analysis a random point on the strip is taken. In contrast the simulation provides exact angular information, so, in order to replicate experimental conditions a random point within the strip is taken. This is discussed in greater detail in section 4.5.3.

The proton energy losses in the 12.6mg/cm^2 aluminium foil, used in the experiment to stop the heavy ions, are calculated after correcting for angle. If the protons are not stopped in the 300μm of silicon then the energy which would be deposited is calculated. Examples for simulations with and without the aluminium foil for the different mechanisms are given later in this chapter.
Straggling in the aluminium foil is also calculated for each proton by choosing a random point on a gaussian centred on the initial energy. The FWHM for the gaussian is determined from the relationships given in [Gil92]. The standard deviation for non-relativistic heavy particles passing through a distance x (in metres) of a material is given by

$$\sigma^2 \;=\; 4\pi N_A r_e^2 (m_e c^2)^2 \rho \frac{Z}{A} x = 15.68 \times 10^{-3} \rho \frac{Z}{A} x \qquad (4.10)$$

where N_A is Avogadro's number, r_e and m_e the classical radius and electron mass and ρ, Z, A are the density, atomic number and atomic weight of the material. For 12.6mg/cm^2(= 4.66×10^{-6} m) of aluminium σ^2=0.961×10^{-3}MeV^2. This gives a FWHM of 75 keV following the relation, FWHM = 2.35σ.
The sort routine calculates a variety of quantities, such as;

- Energy versus energy plots and their projections.
- Proton energies are converted into the c frame using equation(2.2).
- Q-value of the reaction is calculated from equation(2.9).
- Relative energy of the two protons given by equation(2.13).

4.2 Sequential emission

```
-------------------------------------------------------------------
       45.0  250           | beam energy(MeV) Beam FWHM(keV)
      1H(13N,14O)          | target(projectile,ejectile)
      14O->13N+1H          | ejectile -> frag1 + frag2
      13N->12C+1H          | frag1 -> subfrag1-1 + subfrag1-2
                           | frag2 -> subfrag2-1 + subfrag2-2
                           -------------------------------------
        0    0             | energy and width of recoil state
    2.365 0.034            |   ..   ..    ..  .. frag1 state
        0    0             |   ..   ..    ..  .. subfrag1-1 state
        0    0             |   ..   ..    ..  .. subfrag1-2 state
        0    0             |   ..   ..    ..  .. frag2 state
                           |   ..   ..    ..  .. subfrag2-1 state
                           |   ..   ..    ..  .. subfrag2-2 state
                           -------------------------------------
    50000       1   0      | no. of events, detectors, collimators
-------------------------------------------------------------------
        .TRUE.             | LEDA-array ?
         220               | distance target to detector
         iso               | p1: "iso" , "aso"
-------------------------------------------------------------------
```

Figure 4.2: *Example of input file used to simulate sequential decay mechanism. The last line provides the option "aso" of using a non isotropic angular distribution for the first emitted proton.*

An example of the input file for sequential decay is given in figure 4.2. Sequential decay from the 7.77 MeV excited state in ^{14}O can only decay via one intermediate state in ^{13}N which has a width of 33.7$\pm$0.9 keV [Ajz91]. The two protons are unbound by 1.2 MeV which is divided between the two steps as follows;

$$^{14}\mathrm{O} \longrightarrow {}^{13}\mathrm{N}^{*} + p \quad (Q = 775\mathrm{keV})$$

$$^{13}\mathrm{N}^{*} \longrightarrow {}^{12}\mathrm{C}_{\mathrm{gs}} + p \quad (Q = 425\mathrm{keV})$$

The first proton $p1$ is emitted with angular momentum $l = 2$, $(2^{+} \longrightarrow 1/2^{+})$, and the second $p2$ with $l = 0$, $(1/2^{+} \longrightarrow 0^{+})$, as shown in figure 1.12. The simulations shown in this chapter use isotropic emission for the two protons. Figure 4.3 is a plot of the energy of the first proton $p1$ against the energy of the second proton $p2$ with no energy losses in the aluminium foil.

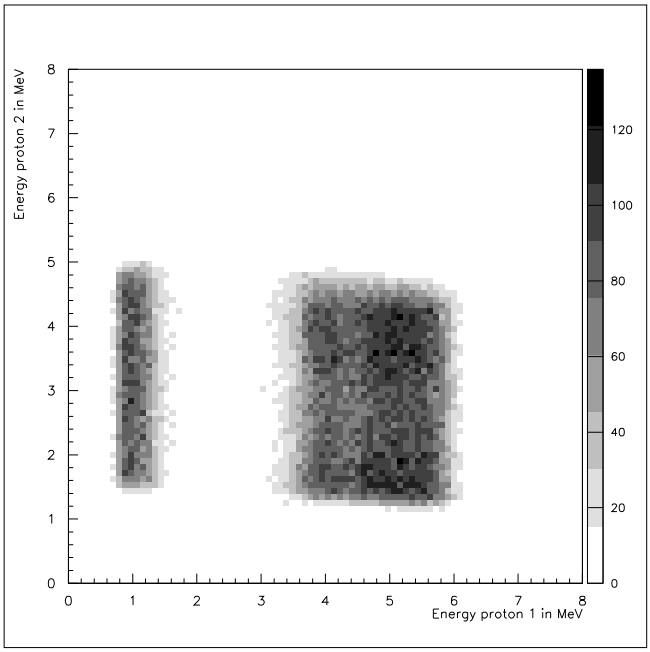

Figure 4.3: *Plot of proton 1 energy against proton 2 energy for sequential emission.*

The separation of the spectra into two fields is due to the first proton moving either towards or away from the detector. The laboratory energies for $p1$ lie between 0.8 MeV to 1.5 MeV and 3.5 MeV to 6 MeV and those of $p2$ from 1.5 MeV to 5 MeV. However with an experimental system which was unable to distinguish the two protons figure 4.4 would be expected. Inclusion of proton energy losses in the aluminium foil results in a 2D plot such as that in figure 4.5 which reveals that the lower energy grouping has insufficient energy to penetrate the foil.

The proton lab energies can be converted back into the centre of mass frame using equation(2.2). This conversion contains the value a_1 which depends on which part of the resonance has been hit. Since this is an unknown quantity in the experiment the simulation uses the energy corresponding to the centre of the resonance. This results in a broadening of the peaks and means that information on the widths is lost. Two examples are given in figures 4.6 and 4.7 which correspond to the cases were there is no aluminium foil and to the case where the foil is present respectively. In the first plot the two groupings are clearly separated with the energies of 720 keV for the first proton and 390 keV for the second. These

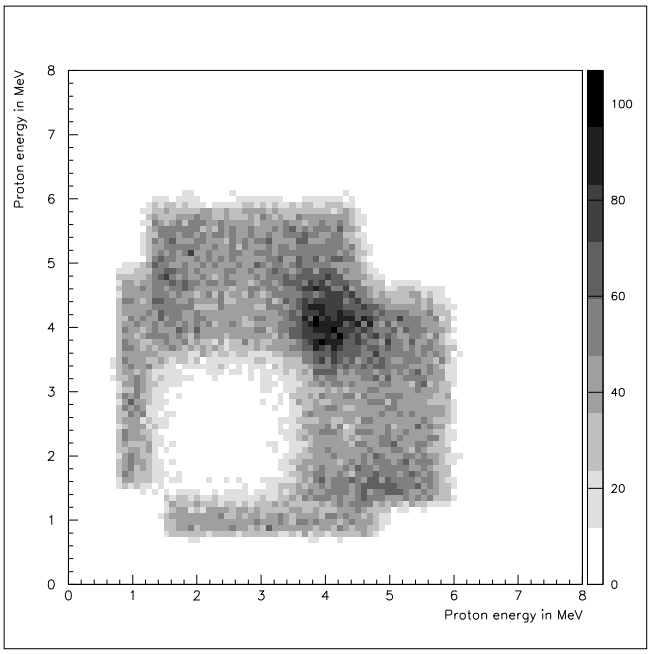

Figure 4.4: *Sequential emission energy-energy plot for coincident protons with no aluminium foil and a target to detector distance of 22cm.*

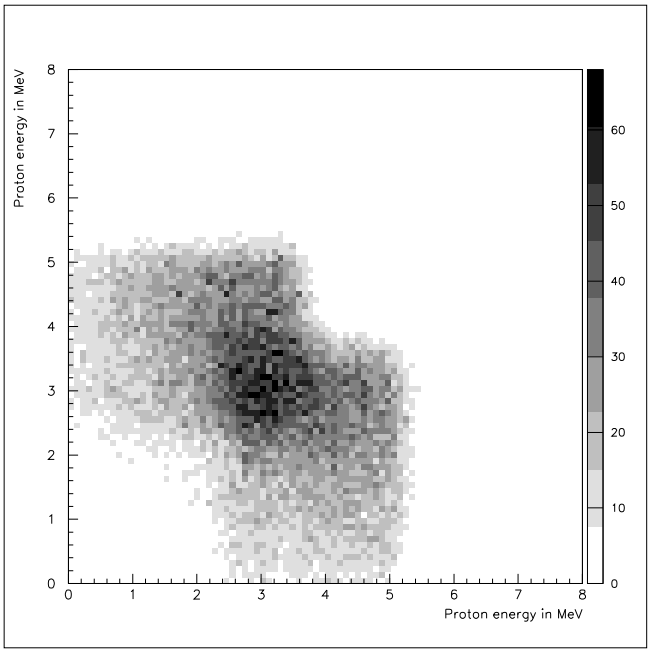

Figure 4.5: *Sequential emission energy-energy plot for coincident protons with proton energy losses due to a 12.6mg/cm^2 aluminium foil calculated. Target to detector distance of 22cm.*

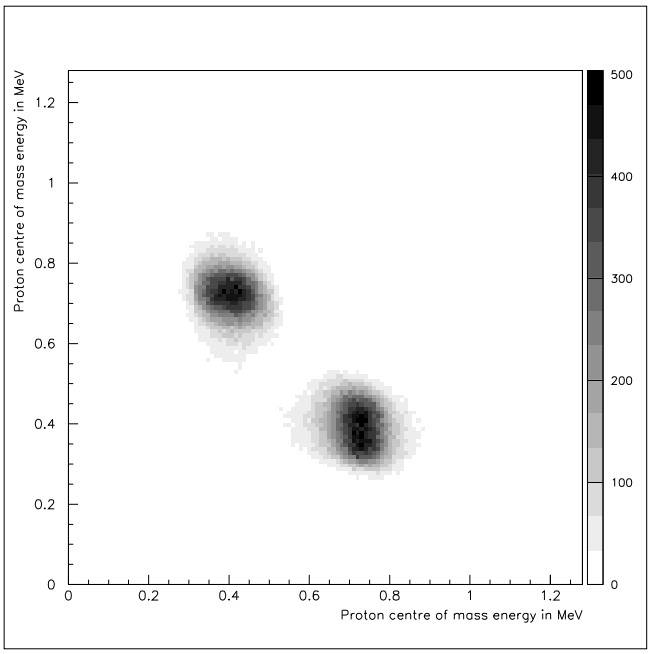

Figure 4.6: *Proton energies converted back into the centre of mass for no aluminium foil. The peaks are at 720 keV and 390 keV as expected from equation (4.5).*

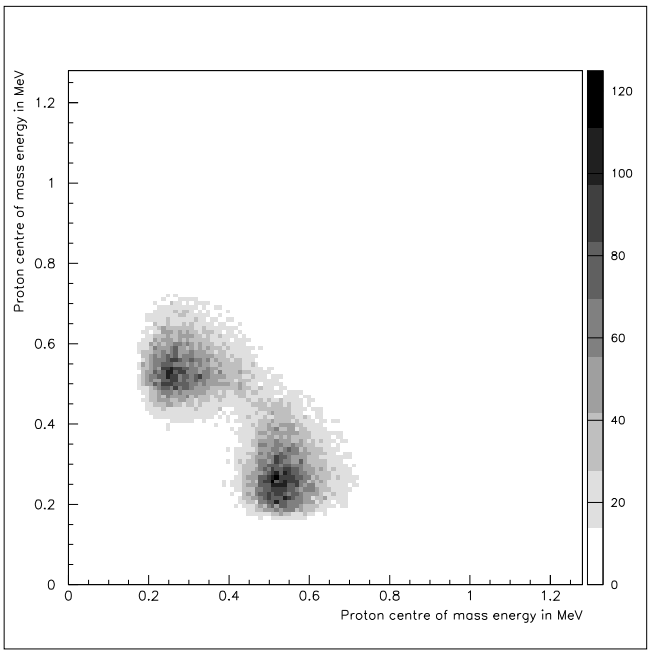

Figure 4.7: *Proton energies converted back into the centre of mass for the aluminium foil present.*

energies correspond to the total transition centre of mass energies shared between the fragments as described by equation(4.5).

With the energies and angles of two coincident protons the Q-value of the reaction can be calculated using the expression given in equation(2.9). The Q-value of the ground state reaction is Q = -1.944 MeV, as shown by the lighter line in figure 4.8, with the darker demonstrating the effect of the aluminium foil.

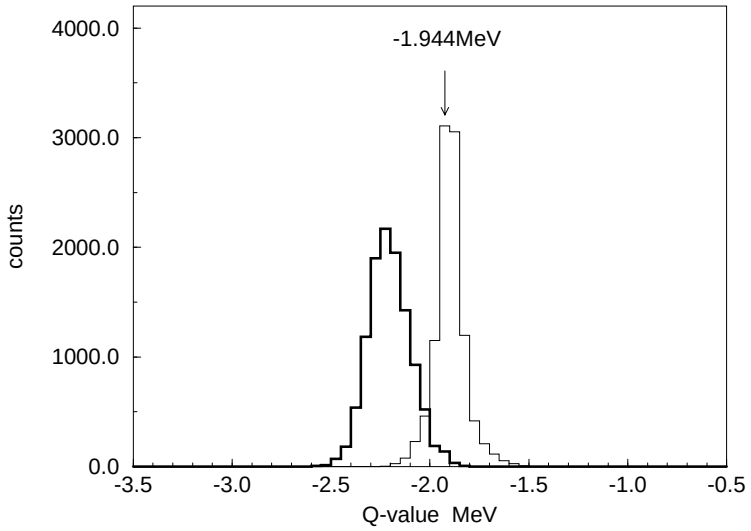

Figure 4.8: *Q-value of reaction* $^{13}\mathrm{N} + p \longrightarrow {}^{12}\mathrm{C}_{\mathrm{gs}} + p + p$ *(Q = -1.944 MeV). Spectra obtained from simulation for sequential emission using a random point on the strip. Darker line shows the effects on the plot when the proton energy losses in the aluminium foil are included in the simulation.*

4.3 ^{2}He emission

```
------------------------------------------------------------------------------
 45.0  250            | beam energy(MeV) Beam FWHM(keV)
1H(13N,14O)           | target(projectile,ejectile)
14O->2HE+12C          | ejectile -> frag1 + frag2
2HE->1H+1H            | frag1 -> subfrag1-1 + subfrag1-2
                      | frag2 -> subfrag2-1 + subfrag2-2
                      ------------------------------------------------
  0    0              | energy and width of recoil state
  0    0              |   ..   ..    ..  .. frag1 state
  0    0              |   ..   ..    ..  .. subfrag1-1 state
  0    0              |   ..   ..    ..  .. subfrag1-2 state
  0    0              |   ..   ..    ..  .. frag2 state
                      |   ..   ..    ..  .. subfrag2-1 state
                      |   ..   ..    ..  .. subfrag2-2 state
                      ------------------------------------------------
50000     1   0       | number of events, detectors, collimators
------------------------------------------------------------------------------
  .TRUE.              | LEDA-array ?
   220                | distance target to detector
------------------------------------------------------------------------------
```

Figure 4.9: *Example of input file used to simulate ^{2}He emission from the 7.77 MeV excited state in ^{14}O.*

The 7.77 MeV excited state in ^{14}O can also decay by emission of a ^{2}He cluster as discussed in section 2.2. Figure 4.9 shows a typical input file for the simulation of ^{2}He emission.

The ^{2}He cluster is formed inside the potential well of the ^{12}C. The total available energy to the two protons is 1.2 MeV, a fraction of this, ϵ, is converted into mass and the remainder E = 1.2 - ϵ is the energy available for the diproton to tunnel through the barrier. When the cluster penetrates the barrier it breaks up into two protons with the mass that held it together converted into relative energy of the pp pair. The decay is described as follows;

$$^{14}\mathrm{O}^{*} \longrightarrow {}^{2}\mathrm{He} + {}^{12}\mathrm{C}_{\mathrm{gs}} \qquad (Q = 1.2 - \epsilon)$$

$$^{2}\mathrm{He} \longrightarrow p + p \qquad (Q = \epsilon)$$

The simulation for diproton emission contains a probability distribution $Prob(\epsilon)$ from 0 to 1.2 MeV given by equation(4.11) and discussed fully in sections 2.2 and 2.3.2. $Prob(\epsilon)$ is the product of the final state interaction density of states and

the barrier penetrability

$$Prob(\epsilon) = \frac{\sin^2 \delta(k)}{C^2 k} \times \exp^{-2G} \tag{4.11}$$

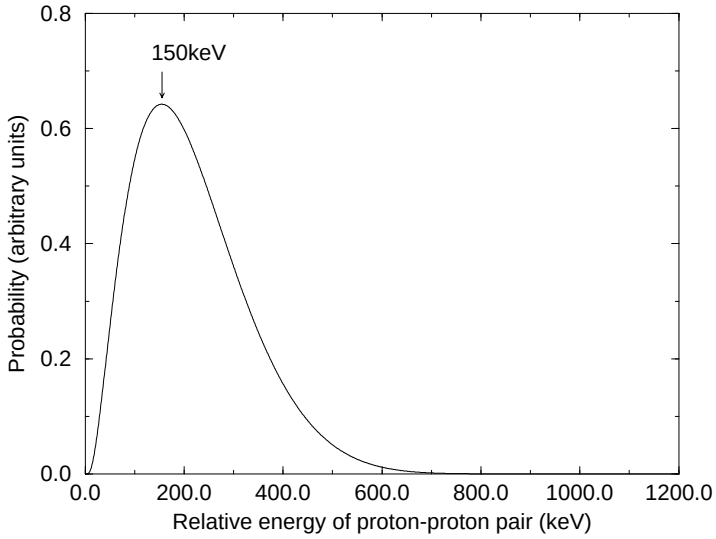

Figure 4.10: *Probability distribution for the relative energy of two protons given by equation(4.11).*

Figure 4.10 shows that the probability distribution has a broad peak centered at 150 keV. For each event in the simulation a value for the *pp* relative energy, ϵ, is taken. This is converted into the binding energy of the ^{2}He cluster by the equation

$$Mass_{^2\mathrm{He}} = {}^1\mathrm{H} + {}^1\mathrm{H} + \epsilon$$

$$Q_{^2\mathrm{He}} = \epsilon$$

The ejectile separation energy described by equation(4.4) is corrected for this mass increase. When the ^{2}He breaks up the two protons equally share ϵ in the centre of mass reference frame. Figure 4.11 is an energy-energy plot for ^{2}He emission and figure 4.12 shows the energy loss effect due to the presence of the aluminium foil. As a test of the code section 4.5.2 shows how these energy-energy plots vary when a narrow peak for the relative energy distribution is used in the simulations.

Figures 4.13 and 4.14 show the proton energies converted into the centre of mass frame, using a random point on the strip to define the angles, for no aluminium foil and for foil present respectively. The former shows a line running along $E^c_{p1}+E^c_{p2} =$ 1.05 MeV as expected for a relative energy distribution peaking at 150 keV.

Figure 4.15 shows the Q-value spectrum with and without aluminium foil with the lighter line corresponding to no foil.

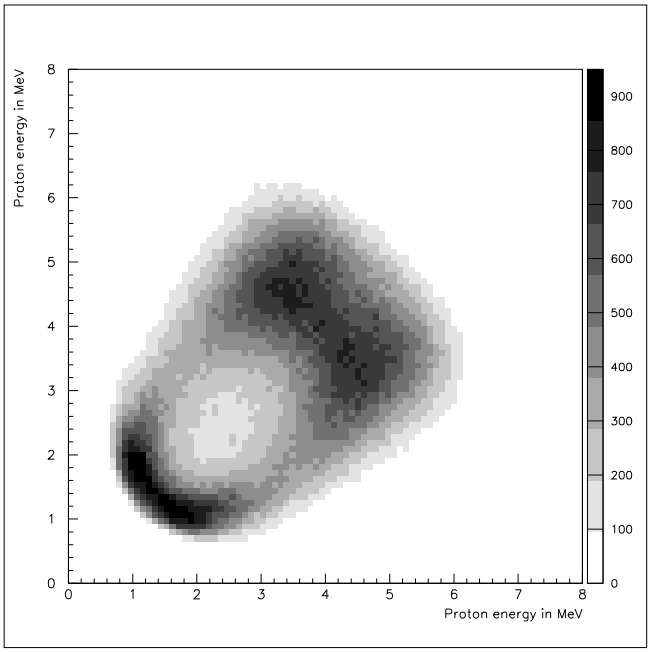

Figure 4.11: *^{2}He emission energy-energy plot for coincident protons with a target to detector distance of 22cm.*

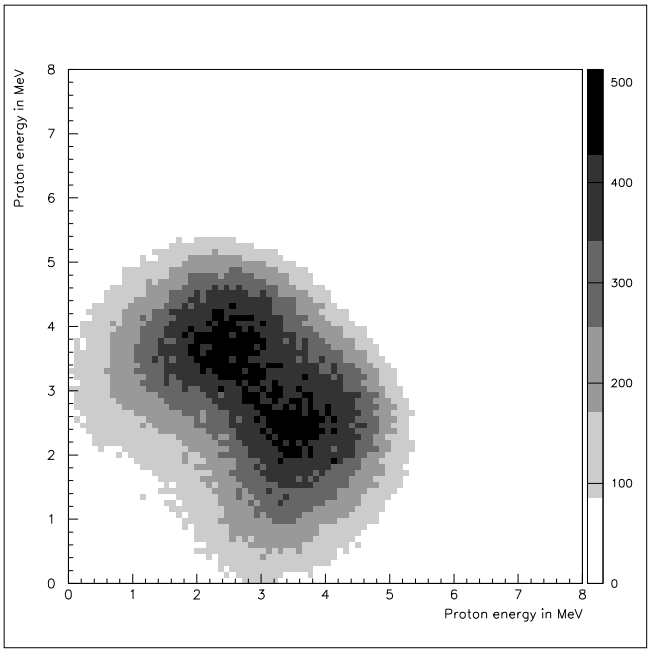

Figure 4.12: *^{2}He emission energy-energy plot for coincident protons with proton energy losses due to a 12.6mg/cm^2 aluminium foil calculated and a target to detector distance of 22cm.*

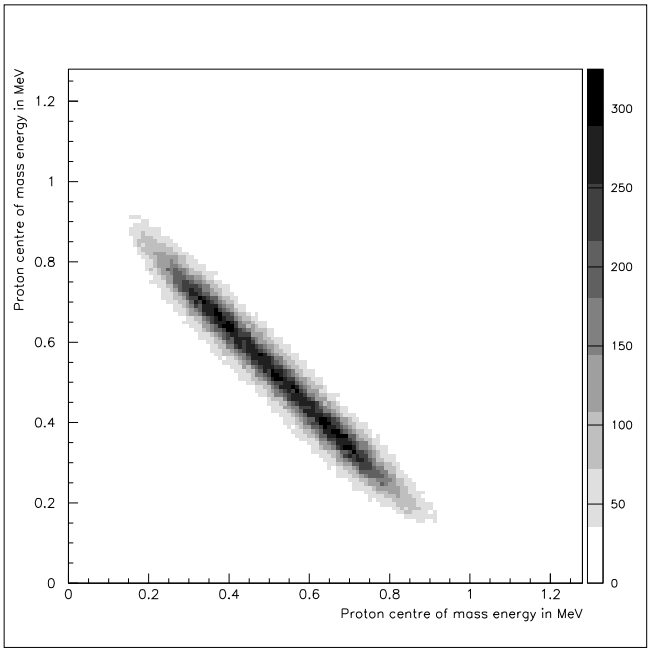

Figure 4.13: *Proton energies converted back into the centre of mass for the no aluminium foil case.*

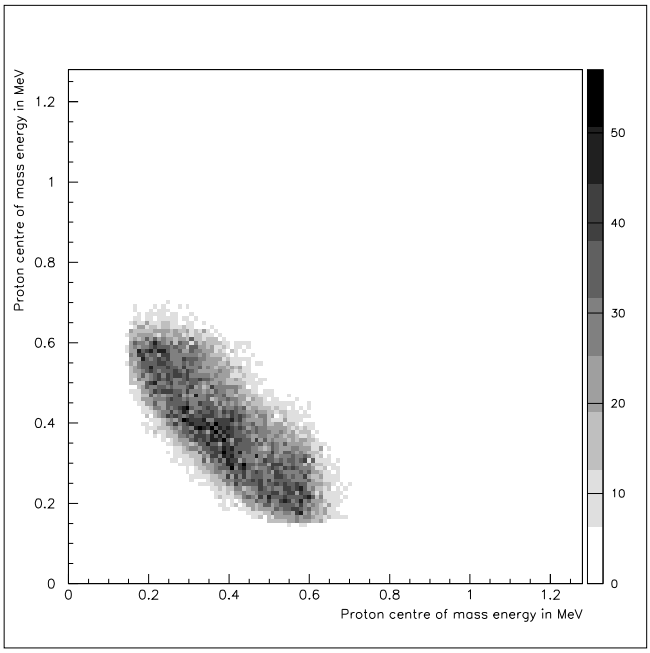

Figure 4.14: *Proton energies converted back into the centre of mass for the aluminium foil present.*

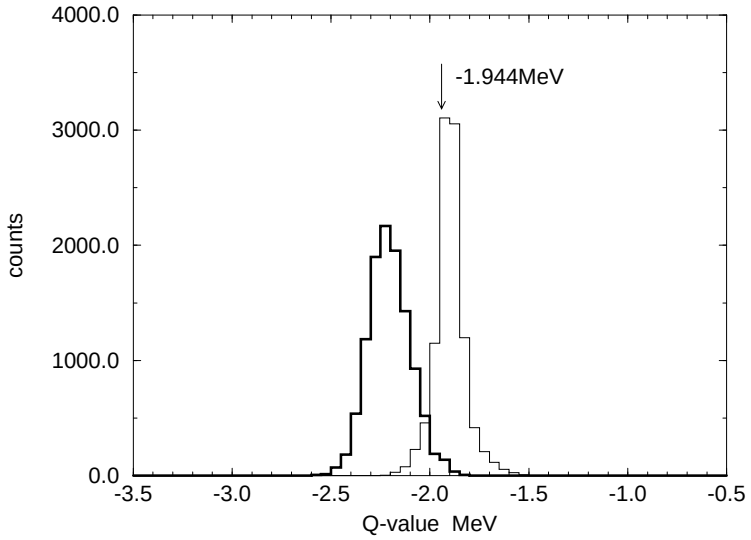

Figure 4.15: *Q-value of reaction* $^{13}\mathrm{N} + p \longrightarrow {}^{12}\mathrm{C}_{\mathrm{gs}} + p + p \quad Q$ = *-1.944 MeV. Darker line shows effect on the spectrum when the aluminium foil is included in the simulation.*

4.4 Comparison of the two mechanisms

It can clearly be seen from figures 4.5 and 4.12 that the protons, after losing energy in the aluminium foil, have a maximum energy less than 6 MeV and will consequently be stopped in the 300μm of silicon which make up LEDA (see table 3.7 for ranges of particles in silicon).

This section presents a comparison of the two mechanisms in which the darker line represents ^{2}He emission and the lighter line sequential emission. All the spectra shown in this section are for the case where the aluminium foil is present.

Figure 4.16 shows how the two mechanisms can be distinguished by comparing slices on the energy-energy plots. These figures correspond to projections of energy-energy plots onto an $E^{l}_{p1} + E^{l}_{p2} = z$ axis where, for the following slices, z is set at;

(a) 5.52 MeV $\leq z <$ 6.44 MeV

(b) 6.44 MeV $\leq z <$ 7.63 MeV

(c) $z \geq 7.36$ MeV

(d) 5.88 MeV $\leq z \leq$ 7.54 MeV

The figures for ^{2}He are relatively flat. For the sequential case the different energy slices produce distinct figures. The slice for (c) corresponds to the highest energy and picks out the two extremes which can be seen in figure 4.5, whilst the others (a),(b) and (d) highlight the high number of counts in the central region in figure 4.5.

The four spectra in figure 4.17(a)-(d) are;

(a) The measured Q-value of the reaction which is independent of the mechanism as expected.

(b) Projection of energy-energy spectra onto 45^o line. In this case the two mechanisms show very little difference.

(c) Opening angle θ_{12} given by equation (2.10). This shows that the ^{2}He has a narrower range of opening angles with a maximum at 12^o whereas the sequential simulation extends up to 50^o.

(d) The relative energy of the pp pair given by equation(2.13) which again shows a large difference between the two mechanisms.

The first two spectra(a) and (b) can be considered to be consistency tests whereas (c) and (d) contain the physics and will be the most important relations for analysing the results and attempting to extract a limit for a ^{2}He component.

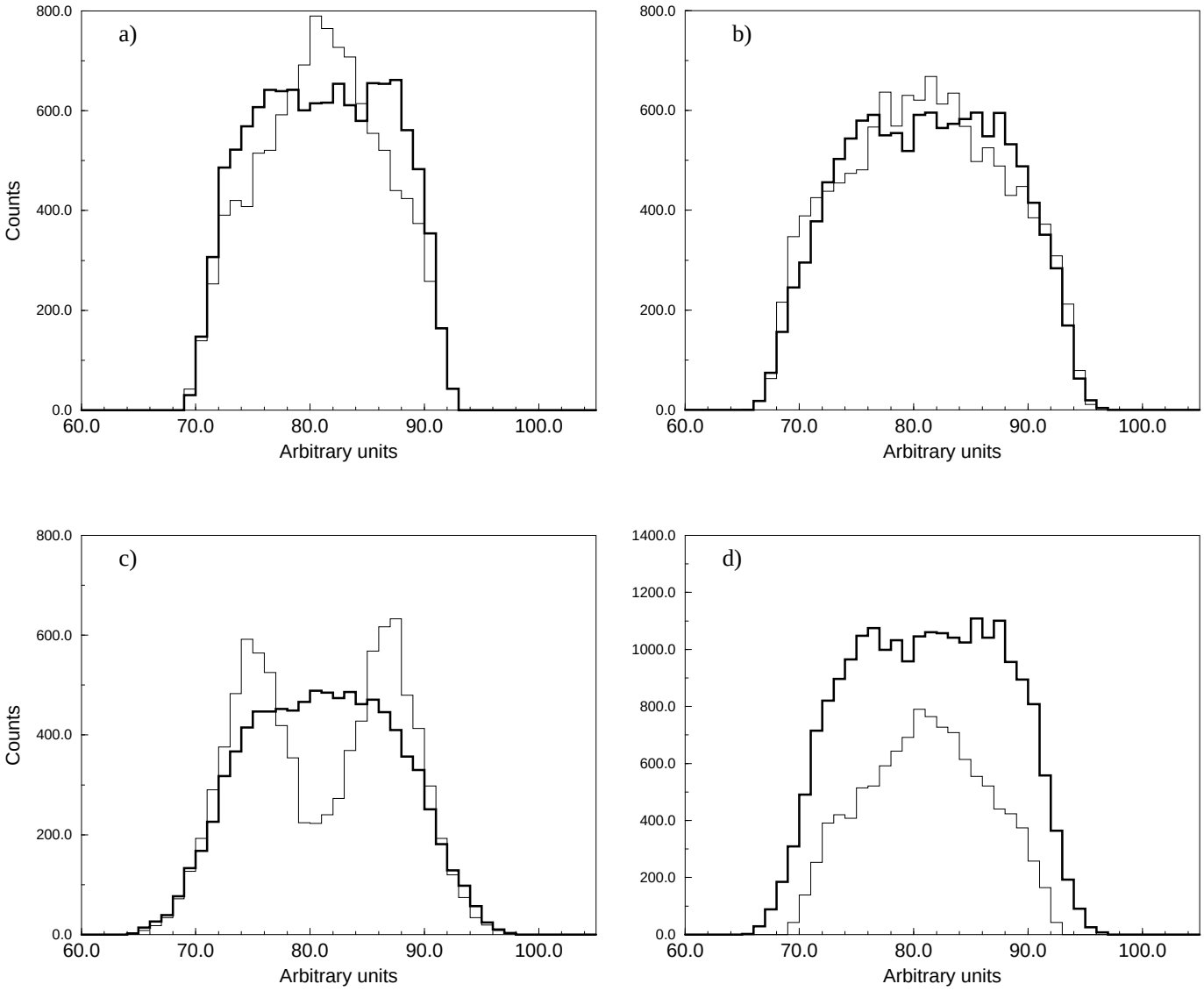

Figure 4.16: *Darker line represents ^{2}He emission and the lighter line sequential emission for the following slices taken from energy-energy plots in figures 4.12 and 4.5. (a) 5.52 MeV $\leq z <$ 6.44 MeV, (b) 6.44 MeV $\leq z <$ 7.63 MeV, (c) $z \geq$ 7.36 MeV, (d) 5.88 MeV $\leq z \leq$ 7.54 MeV.*

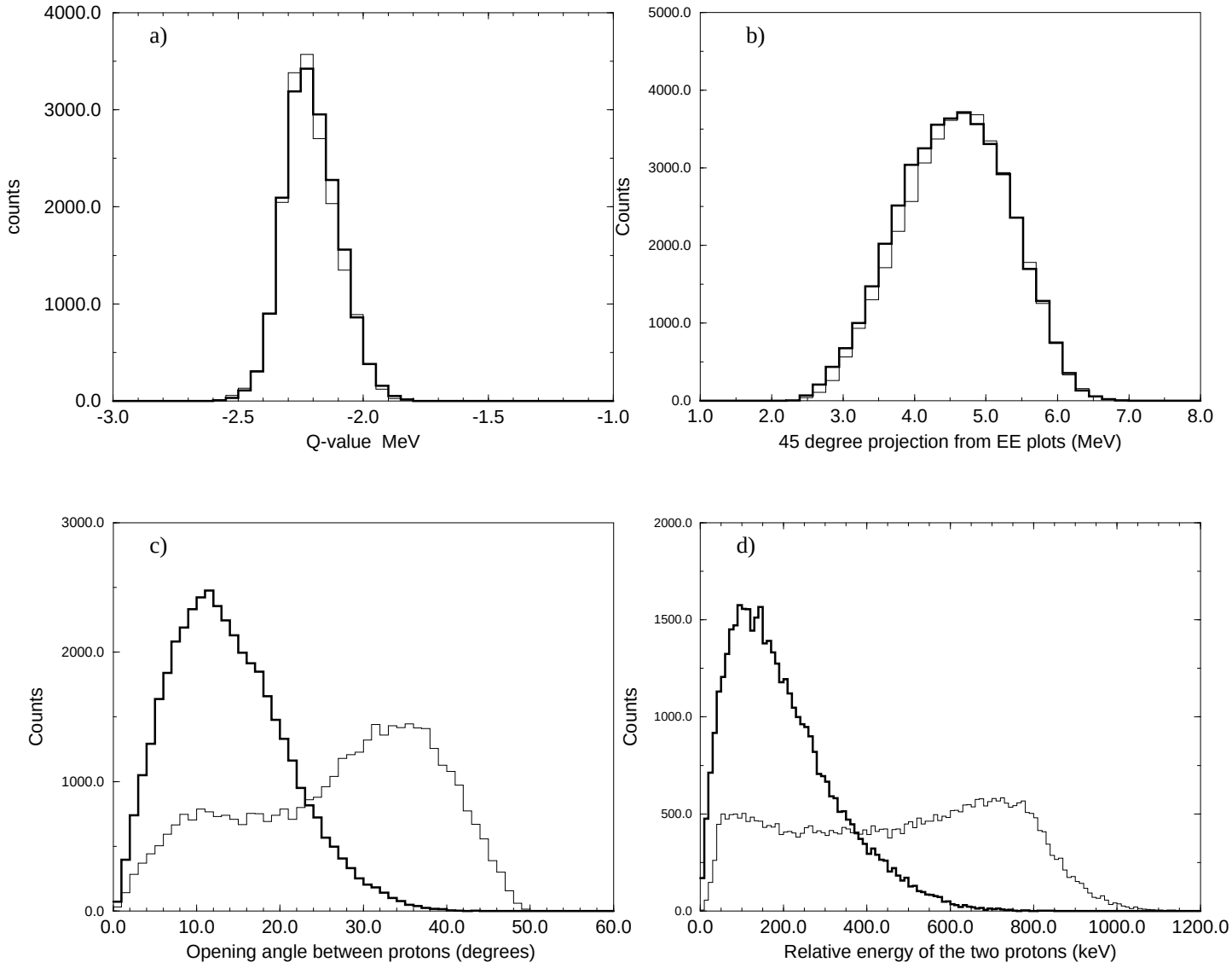

Figure 4.17: *Darker line represents ^{2}He emission and the lighter line sequential emission; (a) Q-value of the reaction, (b) 45^o projection from energy-energy plots, (c) θ_{12} the two proton opening angle and (d) ϵ the relative energy of the pp pair.*

4.5 Testing the code

With the simulations for sequential and ^{2}He emission working well as described in the previous sections it was decided to present the following tests in order to demonstrate how changes in the parameters effect the spectra and how these can be understood.

4.5.1 Simultaneous emission

Simultaneous emission of two protons occurs when the two protons leave the nucleus independently with no angular or energy correlation. The simulation for this mechanism uses the same basic input file as that for sequential (see figure 4.2) but with an artificial intermediate energy level that is given a very small width ($\sim$1 keV).

This section is not a thorough investigation into this mechanism but instead shows the results for two different cases. In the first, case 1, the intermediate level is set at 2.542 MeV so that the protons will equally share the available energy, i.e. each will have 600 keV. For case 2 the level is set at 2.242 MeV whereby the first proton has 900 keV and the second 300 keV. Figure 4.18 (a) and (b) show energy-energy plots for these two cases and show the effect of the choice of intermediate level. Figure 4.4, for sequential emission, lies in between these two extreme cases. These plots show the dramatic effect which results from the energy ranges available to the two protons in the centre of mass.

Figure 4.18(c) and (d) are plots of the proton centre of mass energies and, once again, can be understood in terms of the energy being shared between the protons and recoil nuclei.

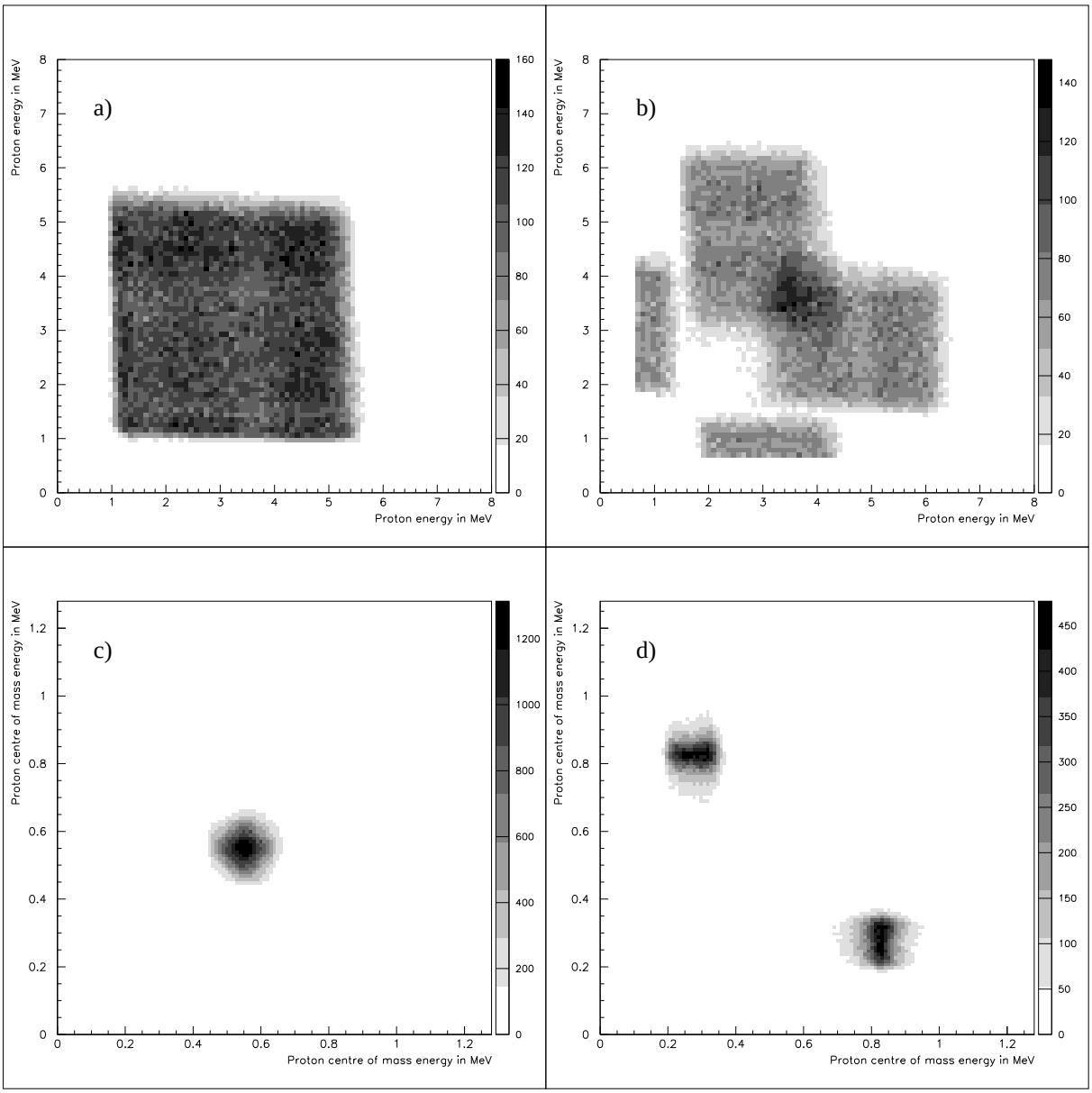

Figure 4.18: *CASE 1-(a) Energy-energy plot for simultaneous emission for protons sharing the total 1.2 MeV equally and (c) is the corresponding conversion into the centre of mass. CASE 2-(b) Energy-energy plot for simultaneous emission where the first proton has 900 keV and the second has 300 keV with (d) the corresponding conversion into the centre of mass.*

4.5.2 Relative energy distribution for ^{2}He emission

This section is meant only as a test of the code. The following energy-energy spectra show the effect of taking a narrow peak for the relative energy for the ^{2}He cluster in favour of using the broad peak as in figure 4.11. Figures 4.19, 4.20 and 4.21 take peak values at 150 keV, 400 keV and 700 keV respectively. The simulations are for no aluminium foil present.

The figures show that as the value for the relative energy increases then more energy is available to the two protons and less to the ^{12}C and as a result the energy-energy plots widen.

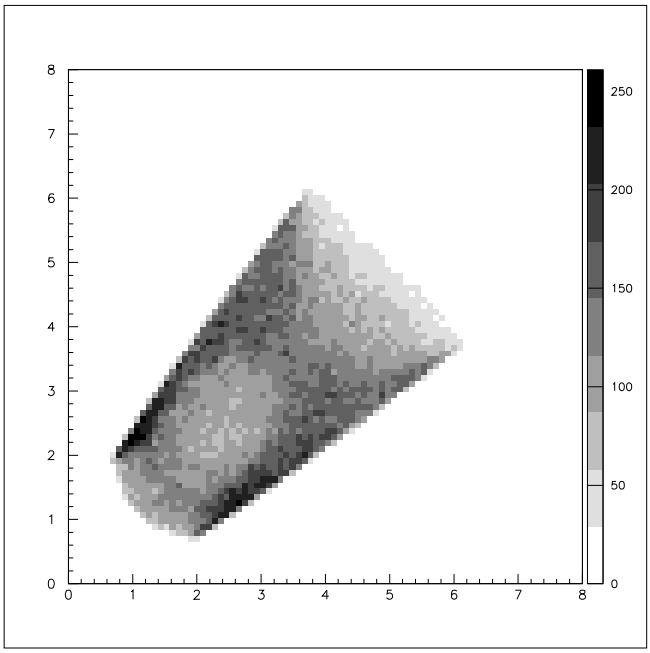

Figure 4.19: *Energy-energy plot for ^{2}He emission using a sharp peak at 150 keV for the relative energy distribution.*

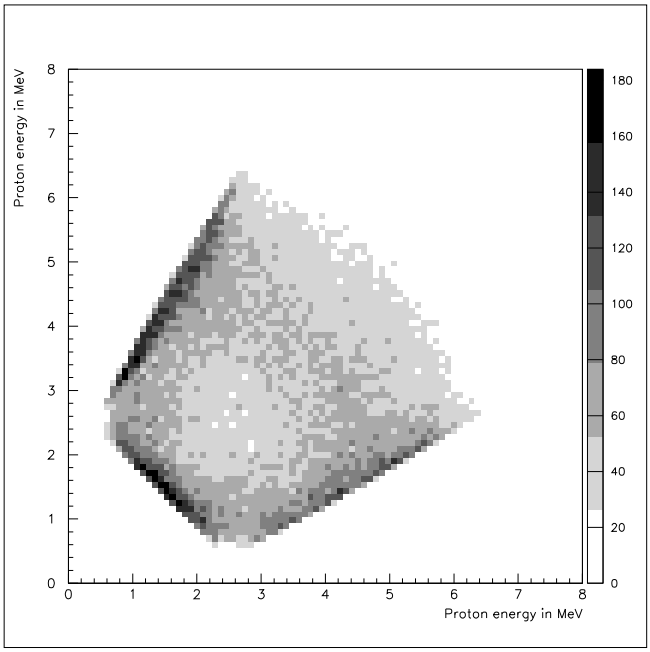

Figure 4.20: *Energy-energy plot for ^{2}He emission using a sharp peak at 400 keV for the relative energy distribution.*

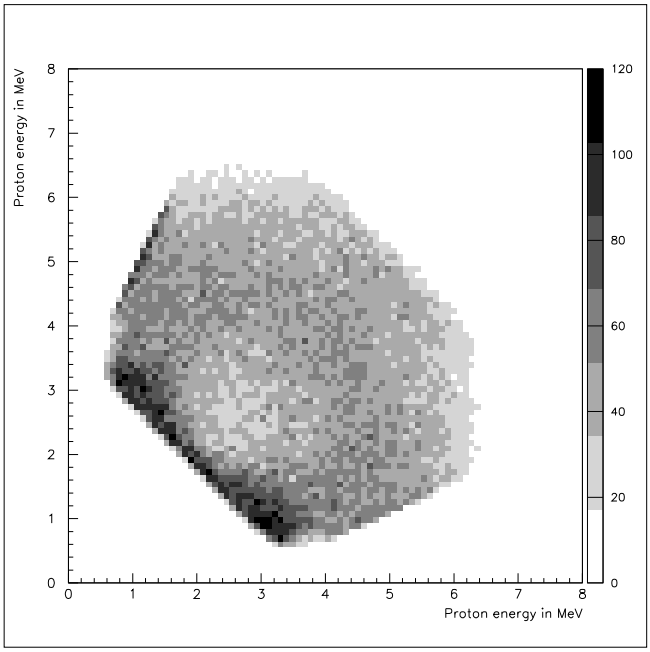

Figure 4.21: *Energy-energy plot for ^{2}He emission using a sharp peak at 700 keV for the relative energy distribution.*

4.5.3 Effect of taking random angle

It was highlighted earlier that under experimental conditions the only angular information comes from identification of the strip which the particle has hit. This introduces a small error in the polar angle but a large one for the azimuthal angle (see tables 3.2 and 3.3). The simulation provides precise angular information as well as $(sector, strip)$ information. Thus the results of the simulation can be presented using either the exact angular information or a random point on the strip. This section presents the results for these two different cases.

The relative energy spectra of the two protons ϵ and the opening angle θ_{12} are shown for the different decay mechanisms. The darker and the lighter line correspond to the cases where precise and random angular information were used respectively.

The results show that the effect is barely noticeable in sequential emission because the range of possible opening angles θ_{12} covers all possibilities that randomising can produce (figure 4.22(a1) and (a2)). Using the broad ^{2}He relative energy distribution produces a noticeable broadening in both spectra (figure 4.22(b1) and (b2)) which is attributed to the smaller range of opening angles.

This effect is increased when a sharp peak is used for the ^{2}He relative spectrum (figure 4.22c1 and c2)). It must be again be highlighted that using a narrow peak for the ^{2}He simulation is not proposed as an option and is only shown here to demonstrate the effect.

The conclusions drawn are that using the random point method in both the analysis of the data and in the simulations is acceptable.

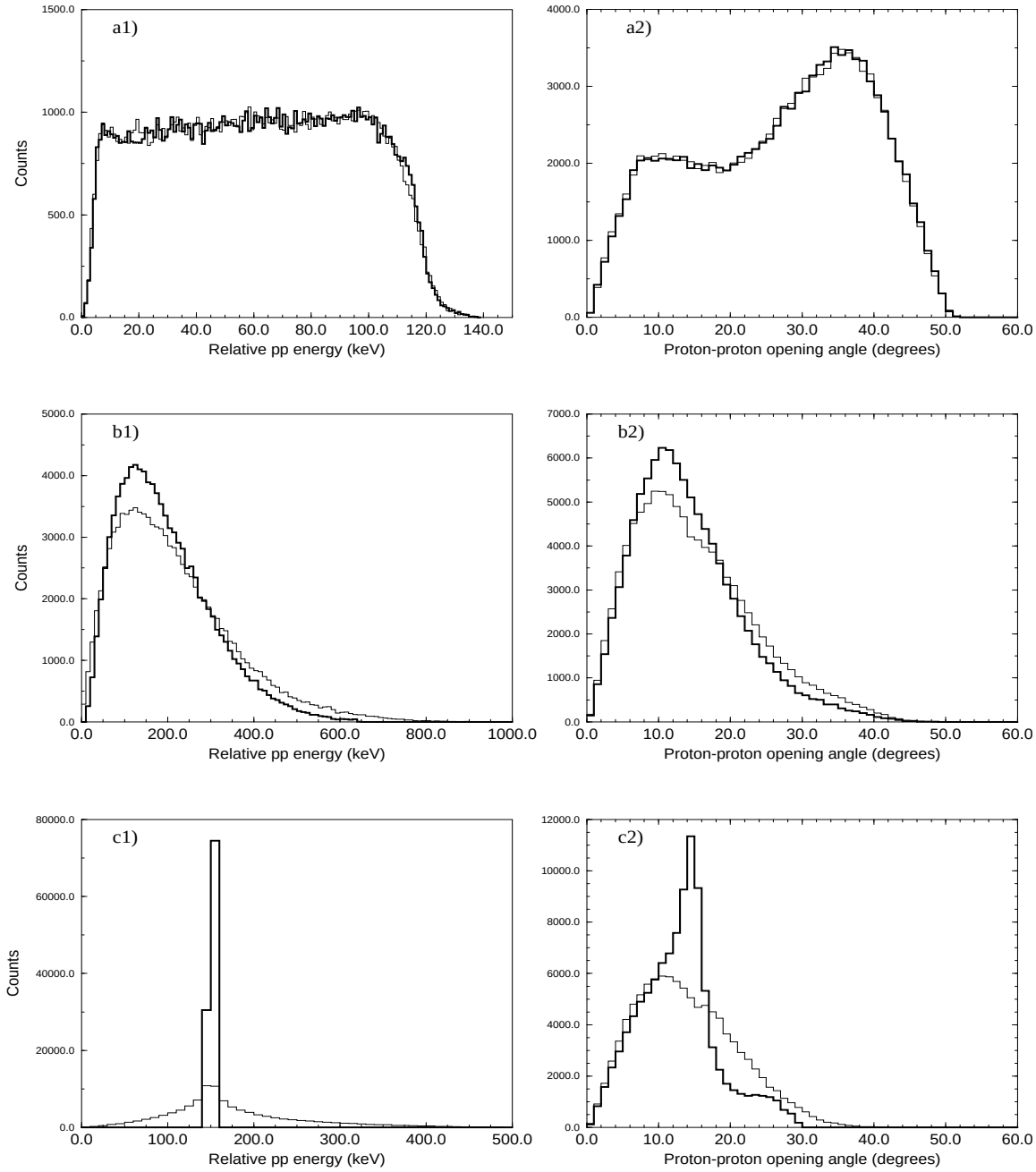

Figure 4.22: *Darker line represents results from simulations which use the precise angular information and the lighter line show results where a random point on the strip was used for θ_{12} and ϵ. (a1-a2) sequential emission, (b1-b2) ^{2}He emission with a broad peak in relative energy spectrum, (c1-c2) ^{2}He emission with a sharp peak centred at 150 keV in relative energy spectrum.*

4.6 Summary

This chapter has provided an extensive study of the Monte Carlo simulations for the different decay mechanisms. The results of these will be compared to the data obtained from the experiment in the next chapter.

Chapter 5

Results and Discussion

Chapter 3 has provided a preliminary analysis describing the general performance of the detection system, particle identification and veto efficiency. This chapter presents an analysis of the nature of the decay mechanism for two proton emission from the 7.77 MeV excited state in ^{14}O.

The first section provides evidence that the resonance was populated by comparison of the on and off-resonance data, also showing how the background can be reduced. The data is then normalised and compared with the simulations for sequential and ^{2}He emission described in chapter 4. These comparisons reveal that the mechanism is dominantly a sequential one. To improve the fits an anisotropic angular distribution for the first, $l = 2$, sequentially emitted proton is introduced into the simulation. An upper limit for the ^{2}He contribution is extracted using χ^2-fits to the data. Finally the results are compared to the theoretically predicted widths using the methods described in chapter 2.

5.1 Resonant features

Figure 5.1 show energy-energy plots for two proton events for on and off-resonance data respectively. The figures immediately reveal that the on-resonance data shows a distinct pattern over the different energies whereas off-resonance is uniform. Both sets of data had approximately the same integrated beam incident on the target as summarised in table 3.6. The spectra show an energy cut off at $\sim$ 1.5 MeV resulting from the proton windows being set above the β-background. Projections of the energy-energy plots onto the 45^o axis in figure 5.2 clearly show the resonant effect.

The Q-value of the reaction for both sets of data is shown in figure 5.3 with the darker line representing on-resonance and the lighter off-resonance. The resonant effect is clear and the peak corresponds to the Q-value of the ground state reaction as described in section 4.4. The background can thus be reduced by placing a cut on this Q-value. The results of making this cut are described following the normalisation process.

5.2 Control experiments

Data from the two sets of control experiments are presented in this section. These were a run with the beam degraded on the CH_2 target and a run with a ^{12}C target.

Normalisation for the off-resonance data is made from the comparison of total integrated beam as measured from the faraday cup for each individual run. Events from the zirconium degrader foil were subtracted from the off-resonance data. Examples of spectra showing the on and off-resonance data have been given in the previous section in figures 5.2 and 5.3. They show the non-resonant contribution producing a smooth broad peak under the resonance. The same can be seen in the ^{12}C data.

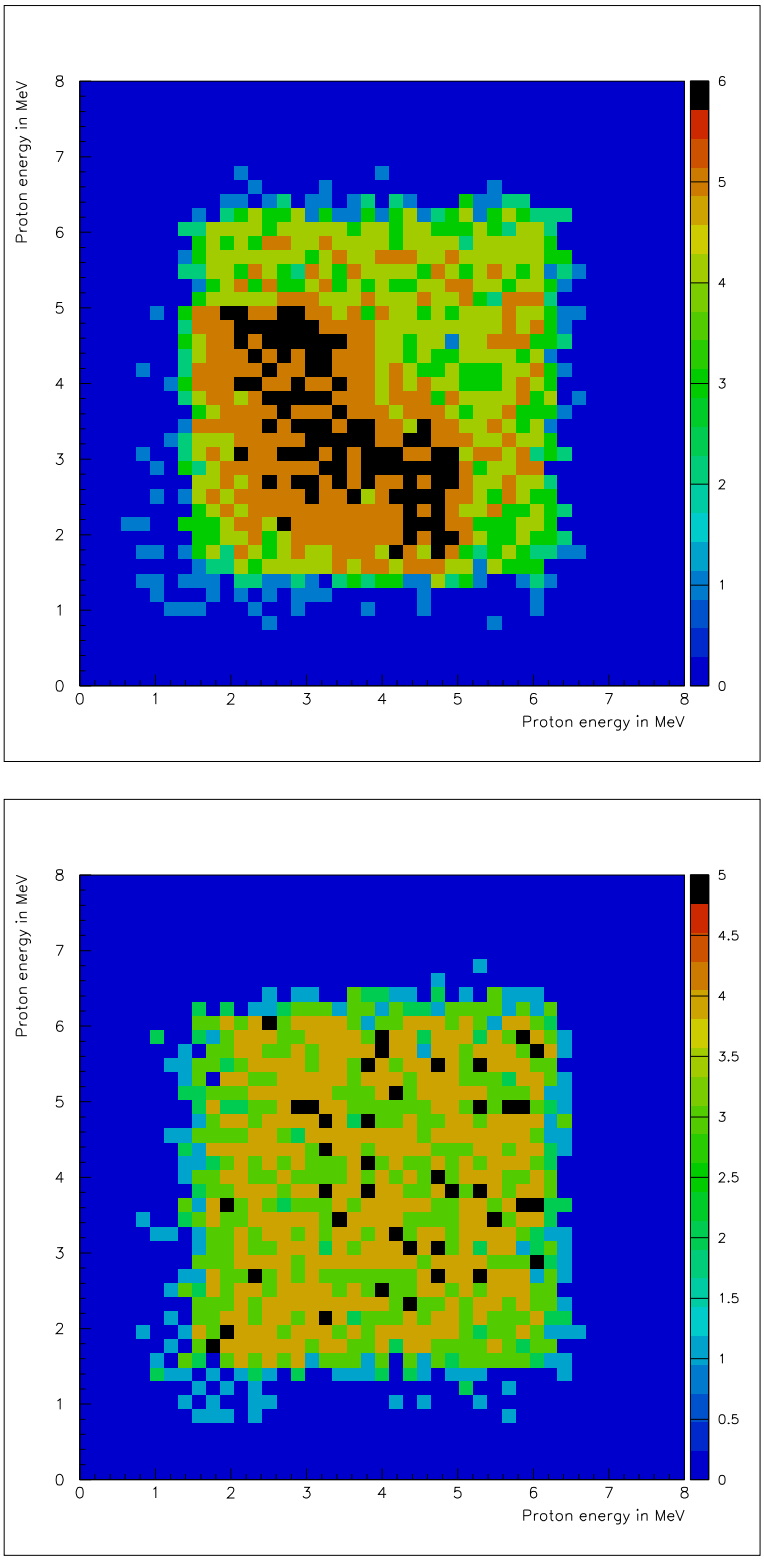

Figure 5.1: *Energy-energy plots for two protons detected in coincidence which have been stopped in front detector. Top figure is for on-resonance data and bottom for off-resonance.*

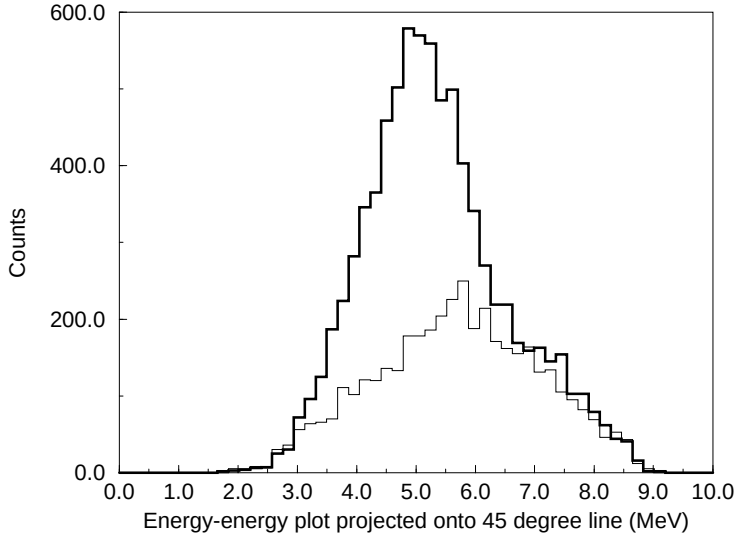

Figure 5.2: *Projection of energy-energy plots shown in figure 5.1 onto 45^o axis. Darker line represents on-resonance data and lighter line is off-resonance.*

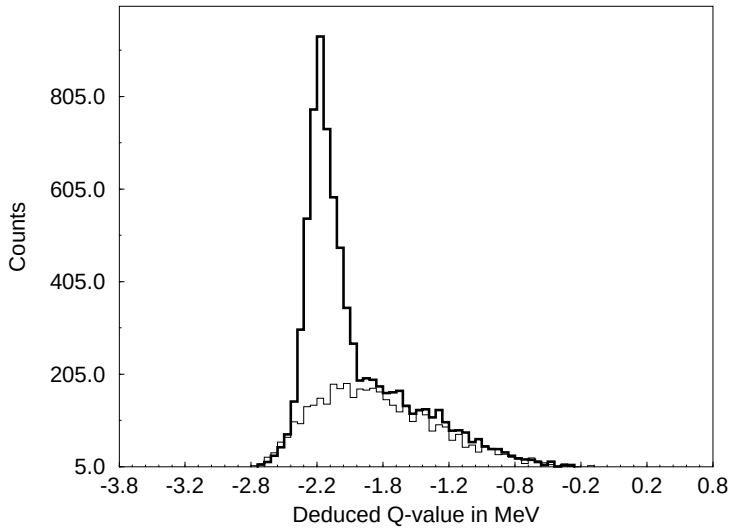

Figure 5.3: *Q-value calculated for each two proton event for on-resonance (dark line) and off-resonance (light line).*

The normalisation process for the ^{12}C data is the same as that used in the commissioning run described in section 3.3.8. From the high energy singles alphas observed in the CH_2 and ^{12}C data a ratio of 1.53$\pm$0.05 is determined for reactions induced by ^{12}C nuclei in the two targets. Figure 5.4 and 5.5 shows the on-resonance data (with the darker line) and the ^{12}C data (lighter line) for the 45^o projection and the measured Q-value. The spectra clearly show the resonant effect and that the evaporation protons produce a smooth broad peak under it. Using the integrated beam corrected for target thickness does not produce the same ratio which can be. understood if the ^{12}C target had been thicker than the 200μg/cm^2.

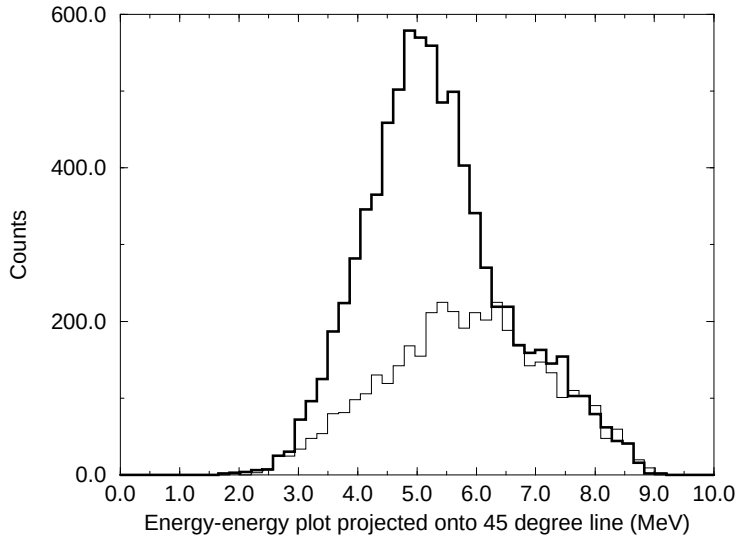

Figure 5.4: *Projection of energy-energy plots onto 45^o axis. Darker line represents on-resonance data and lighter line is ^{12}C normalised w.r.t. the alphas.*

As described in the previous section a cut on the Q-value is made on the data in order to reduce the background, a reduction which will be quantified in the next section. Since this is the case it is most useful now to compare the ^{12}C and off-resonance sets of data with this cut.

Figure 5.6(a)-(d) show comparisons of the off-resonance data with the zirconium events removed (dark line) and ^{12}C data (dashed line). Error bars have not been

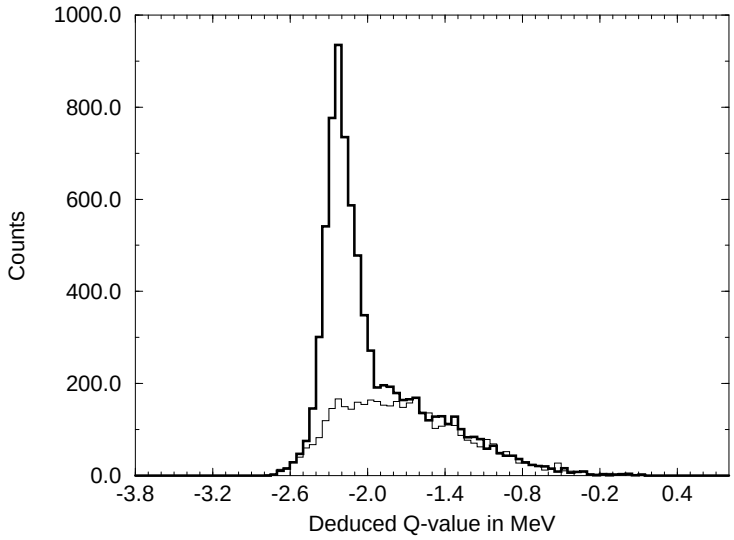

Figure 5.5: *Q-value calculated for each event for on-resonance (dark line) and* ^{12}C *data (light line) normalised w.r.t. the alphas.*

included in the data to make their viewing easier;
(a) Q-value of the reaction with both sets of data having the same general shape.
(b) 45^o projection of energy-energy plots which shows that degrading the beam energy does not affect the shape of the evaporation proton distribution.
(c)-(d) are the *pp* relative opening angle θ_{12} and the relative energy ϵ. The plot for ϵ shows number of counts increasing as the the energy tends to zero for both sets of data. This is an important point and will be referred to again when the normalised data is compared to the simulations.

In general the two sets of data shown agree within error. The spectra emphasise the fact that beam degradation has a negligible effect on the proton evaporation characteristics.

Normalisation with respect to the ^{12}C data was effective for data taken from the commissioning run but it was felt that the uncertainty in the target thickness meant that normalisation with the off-resonance data would be more reliable. The following section presents the data which has been normalised in this way.

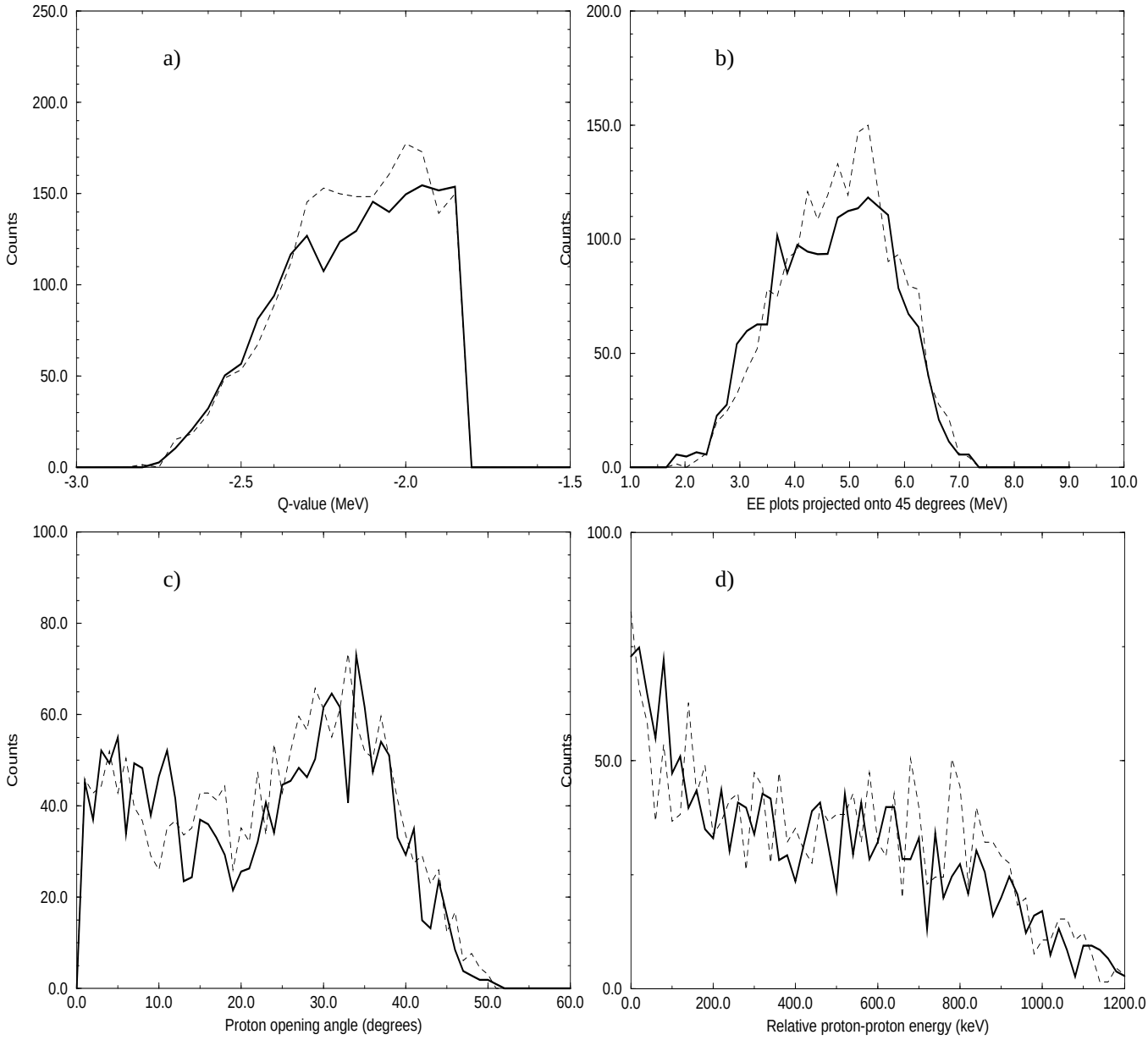

Figure 5.6: Comparison of off-resonance data (solid line) and ^{12}C data (dashed line) for events with $Q \leq -1.85$ MeV. (a) Q-value of the reaction, (b) 45^o projection from energy-energy plots, (c) θ_{12} the two proton opening angle and (d) ϵ the relative energy of the pp pair.

5.3 Normalised data

The results for the data with a cut of $Q \leq$-1.85 MeV are shown in the energy-energy plots in figure 5.7. The cut reduces the background from 48% to 36% compared to 90% in the commissioning run (see section 3.3.8). This section shows the data with this cut and normalised with respect to the off-resonance data. The total number of proton-proton events is ~3900. This shows the increase in statistics obtained from directly populating the resonance as compared to populating using β-decay (see figure 1.5) and also represents approximately ten times as many counts as obtained by Kryger *et al.*[Kry95] (shown in figure 1.4).

The pattern in the on-resonance data becomes clearer than in the previous energy-energy plots. The plots for the proton centre of mass energies shown in figure 5.8 also show a distinct pattern for on-resonance with two groups appearing indicating an energy correlation in the centre of mass. Both these plots are very similar to the simulations for sequential shown in section 4.2.

Figures 5.9 and 5.10 show the proton energy spectra for the sum of all strips in each ring. Ring 15 is the innermost and clearly shows a two peak structure. As the angle increase the positions of the peaks decrease and in the outermost ring (ring 4) the second peak does not have sufficient energy to penetrate the aluminium foil and thus only one is present. This distinct separation into two different energy components results from different energies in the centre of mass. This will be shown in the next section to be a clear signal for the sequential decay mechanism.

The projections of the energy-energy plots onto equal energy axes shown in figure 5.11 all have distinct shapes with (c) clearly showing a structure with two peaks.

Finally, figure 5.12(a)-(d) show the key spectra for the;
(a) Q-value of the reaction,
(b) 45^o projection from energy-energy plots,
(c) θ_{12} the two proton opening angle and

(d) ϵ the relative energy of the pp pair.

The next section compares the data to the different simulations for the two proton emission mechanisms.

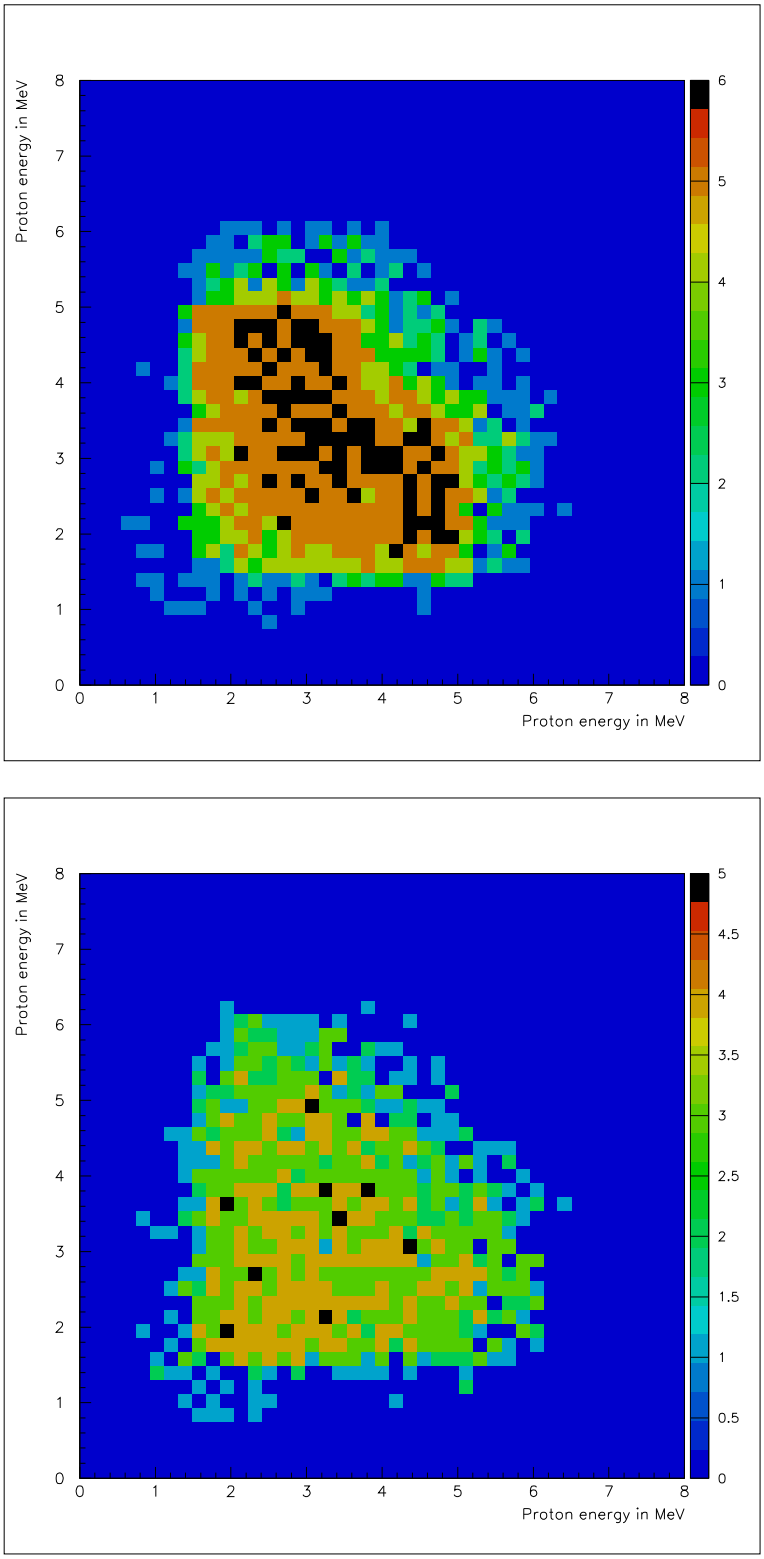

Figure 5.7: *Energy-energy plots for two protons detected in coincidence with* $Q \leq -1.85$ *MeV. Top figure is for on-resonance data and bottom for off-resonance.*

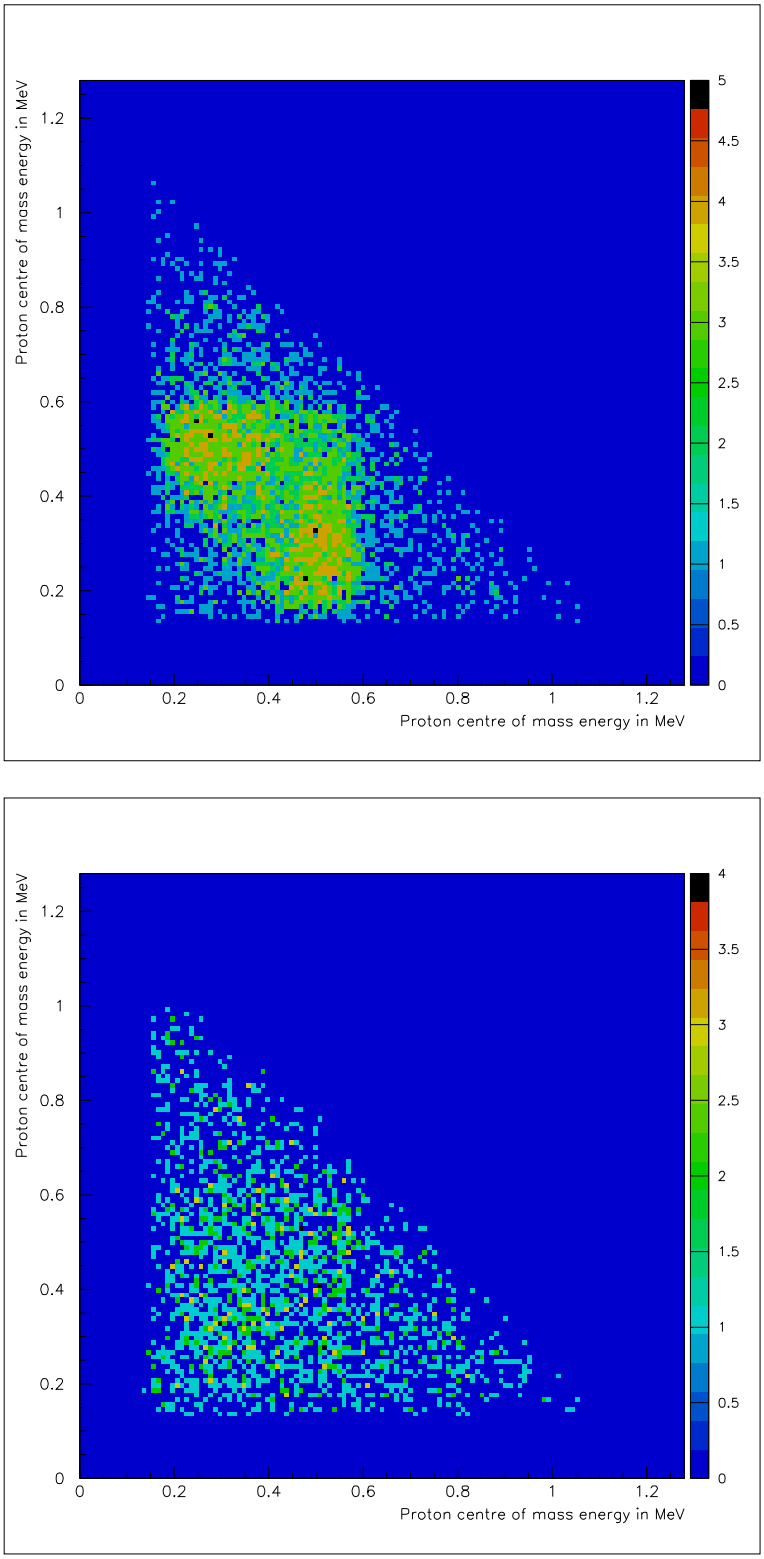

Figure 5.8: *Proton centre of mass energy-energy plots with Q-value cut. Top figure is for on-resonance data and bottom for off-resonance.*

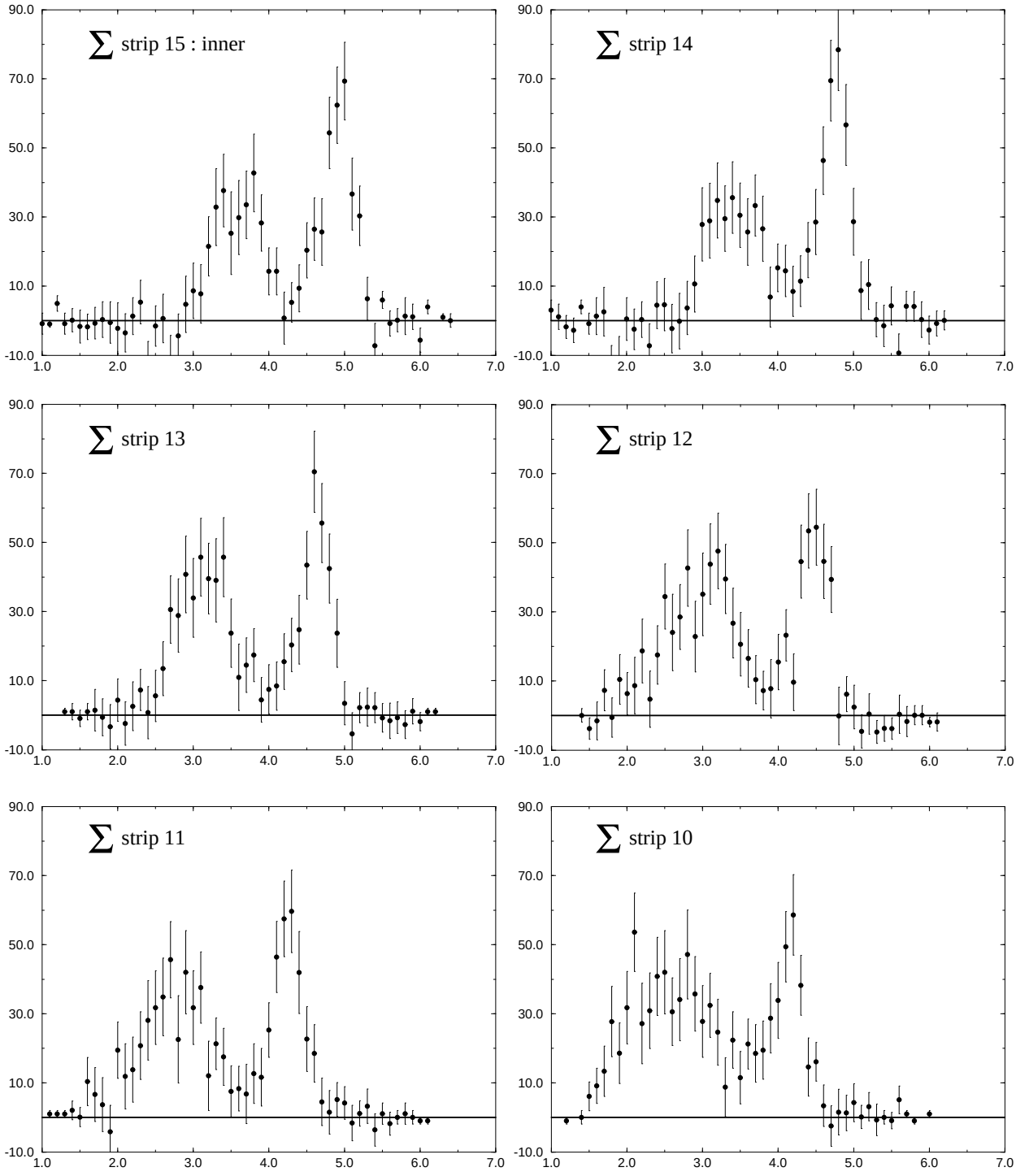

Figure 5.9: Normalised data for the proton energy spectra for two proton events for the sum of the strips in each ring. Plot shows rings 15 to 10 where 15 is at the innermost angles.

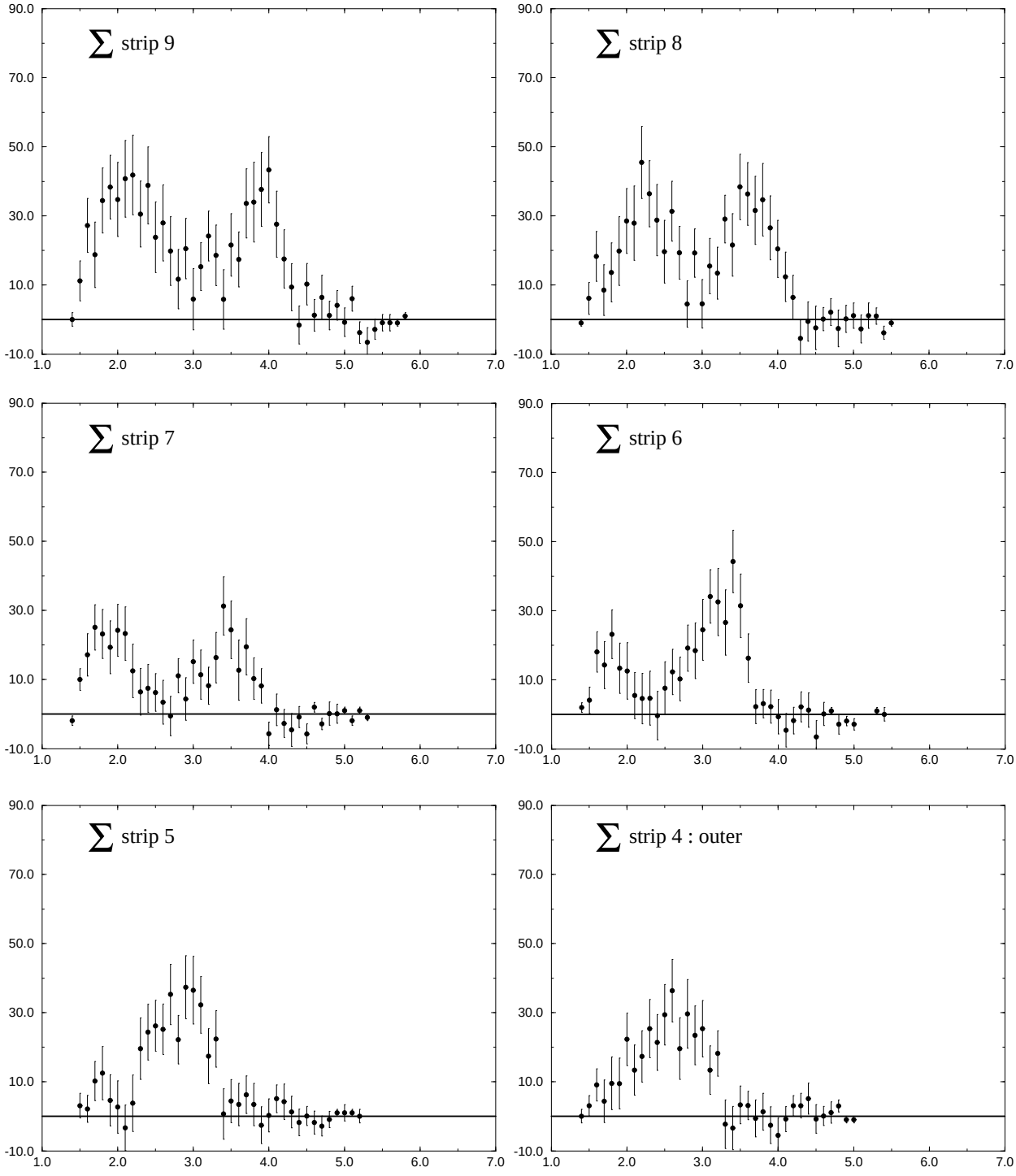

Figure 5.10: Normalised data for the proton energy spectra for rings 9 to 4.

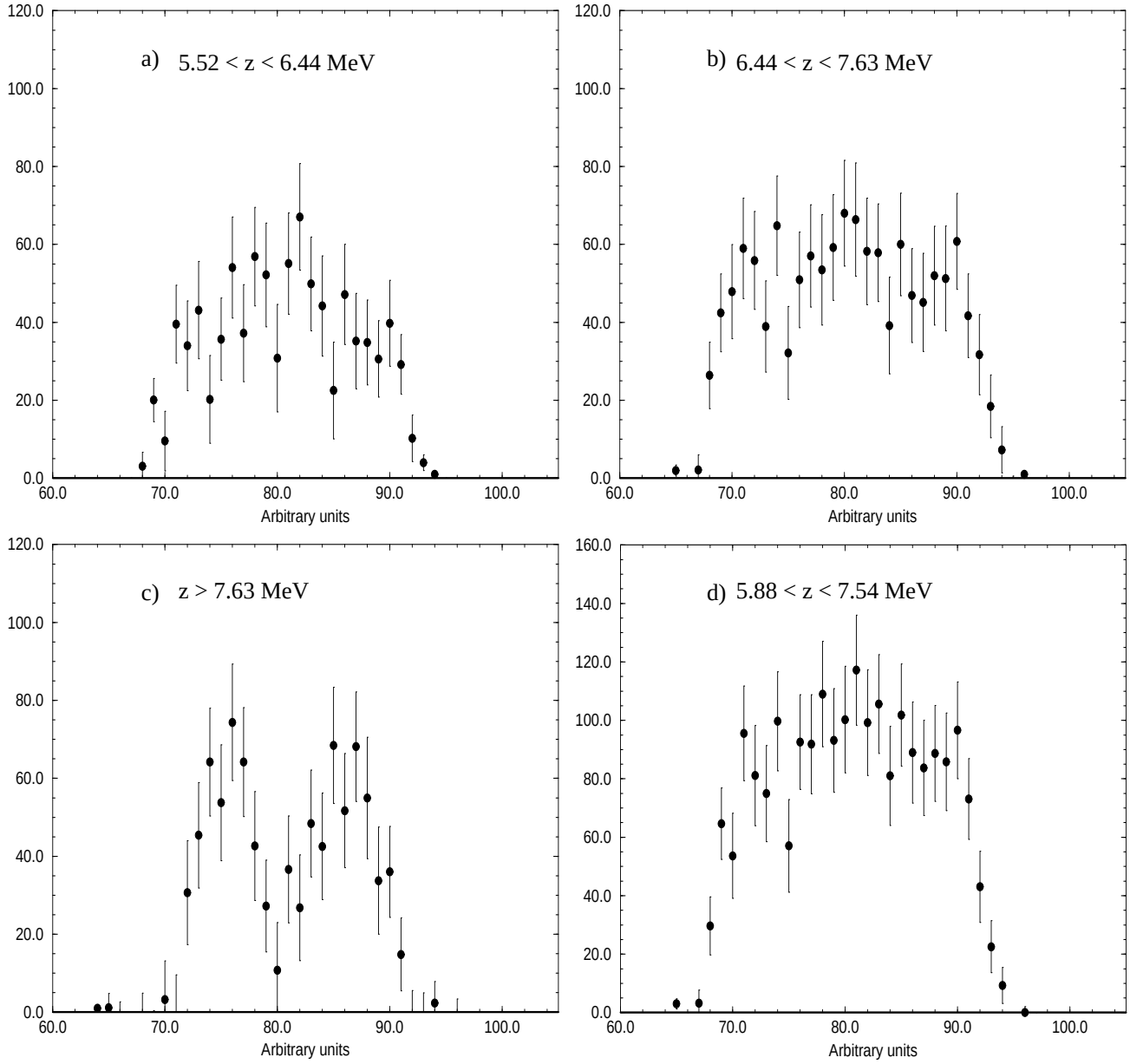

Figure 5.11: Figure shows different projections of slices on the energy-energy plot for normalised data. The values for the different slices are shown on the spectra where $z = E_{p1} + E_{p2}$.

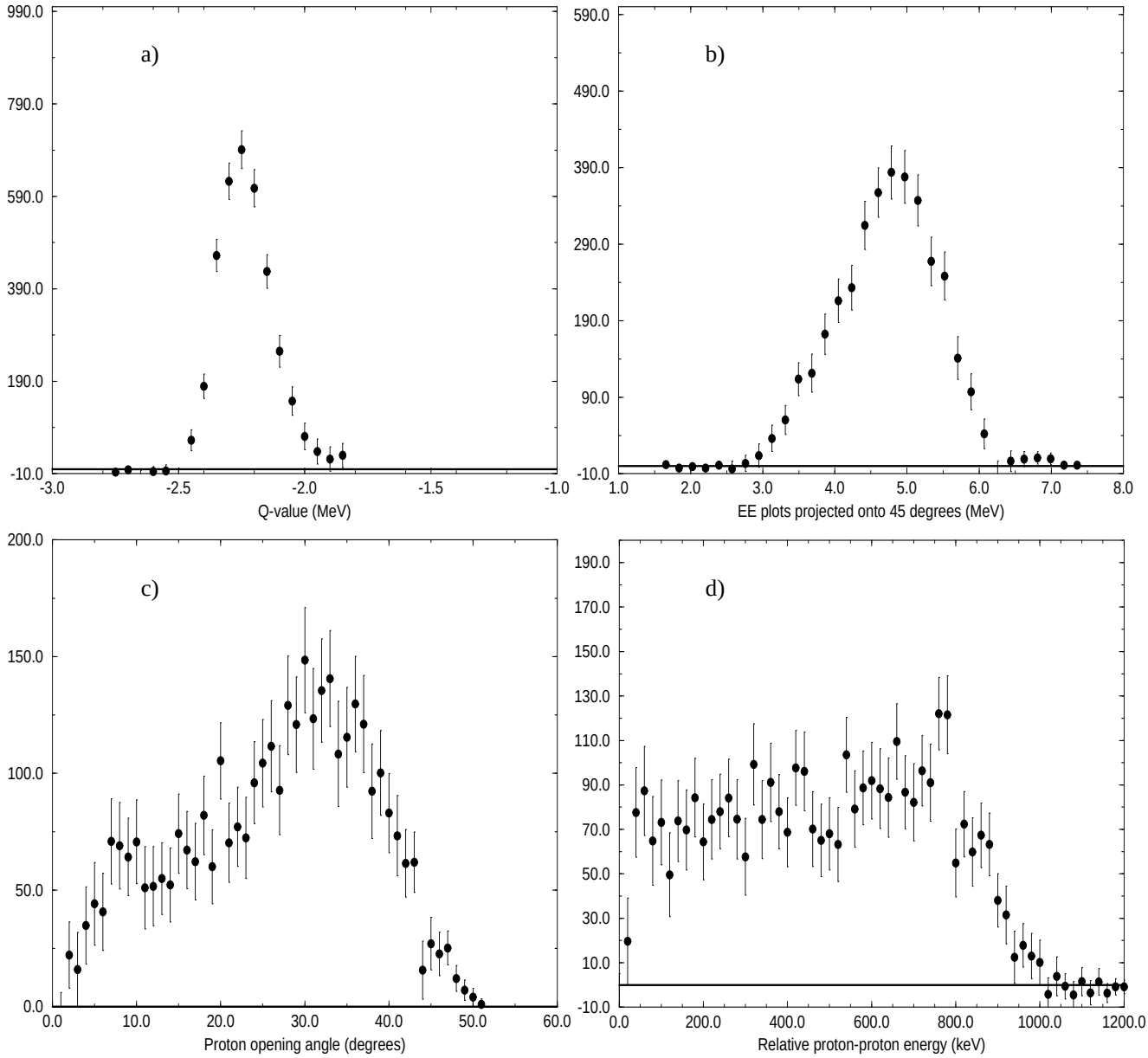

Figure 5.12: Normalised data plots for (a) Q-value of the reaction, (b) 45^o projection from energy-energy plots, (c) θ_{12} the two proton opening angle and (d) ϵ the relative energy of the pp pair.

5.4 Comparison of data with simulation

5.4.1 Isotropic sequential emission

The following spectra compare the simulation for sequential emission, where both protons are emitted isotropically into 4π, and the normalised data.

Figures 5.13 and 5.14 show the proton energy spectra for the sum of all strips in each ring. In the sequential simulation the two peaks correspond to the two emitted protons with the high energy peak being the first proton $p1$ and the lower energy peak the second proton $p2$. As the angle increases the proton peaks decrease in energy and for the outermost strip $p2$ has insufficient energy to penetrate the aluminium foil.

There is very good agreement between the data and the simulation for the peak positions and widths but there is a clear disagreement in the number of counts under each peak. At small angles (strip 15) the simulation does not produce enough numbers of $p1$ whereas at larger angles (strip 4) it overestimates. The distribution of $p2$ is the reverse of this. This represents a focusing of $p1$ into forward angles as expected for a proton with angular momentum not equal to zero. The $p2$ peaks in rings 5 to 8 appear to peak too early in the simulation.

Figure 5.15 (a)-(d) show the different projections of the energy-energy spectra for the different slices. The data in (c) reproduces the peak positions but underestimates the number whilst the data in the three other spectra have peaks on either side of the central maximum which are not reproduced by the simulation.

The first two spectra from the four in figure 5.16 are measures of the general goodness of fit but the second two (c),(d) contain the physics;
(a) the Q-value of the reaction which matches the data well and
(b) the 45^o projection of the energy-energy plots shows that there is disagreement with the simulation peaking at a lower energy than the data.

The other two spectra (c) and (d) show the opening angle between the two protons θ_{12} and the pp relative energy ϵ. In both cases there is good agreement. The plot for ϵ shows a steady drop to zero for low energy values in both the data and the simulation. This may have been considered as an edge effect from the analysis and simulation but when the equivalent off-resonance spectra are viewed in figures 5.6(d) it appears that this a real effect.

This section has shown that there is good agreement between the data and the simulation for sequential emission. The biggest disagreement comes from the angular distribution of the protons. This would have been expected since the simulation assumes isotropic emission which is incorrect since the first proton has $l = 2$. Results of using an anisotropic emission for $p1$ are described in section 5.4.3, but first a comparison of the data and the simulation for ^{2}He is presented.

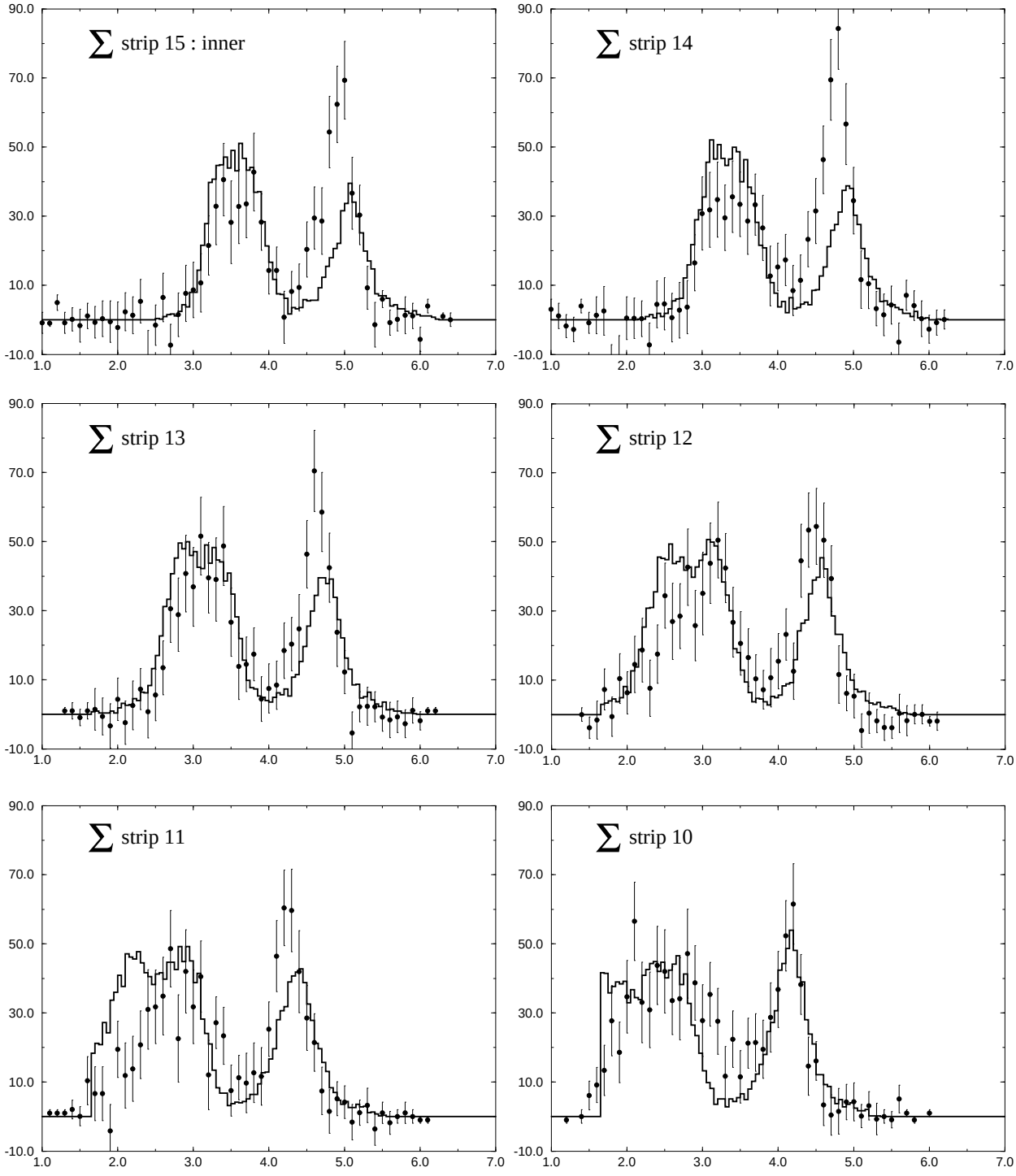

Figure 5.13: Normalised data shown by filled points with the solid line representing isotropic sequential emission overlapped. The spectra show the proton energy spectra for two proton events for the sum of the strips in each ring. Strip 15 is the innermost angle.

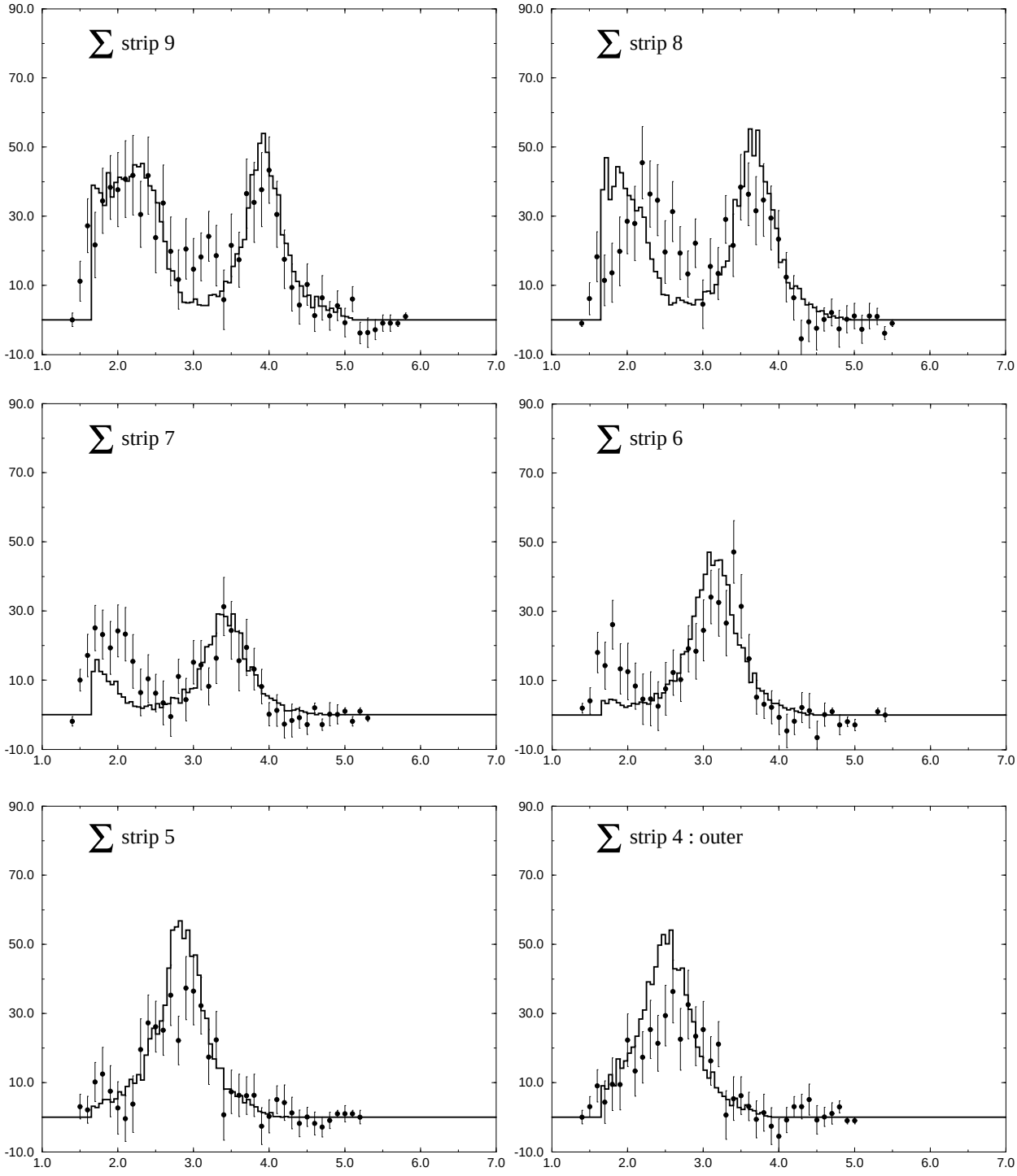

Figure 5.14: Normalised data shown by filled points with the solid line representing isotropic sequential emission overlapped. Strip 4 is the outermost angle.

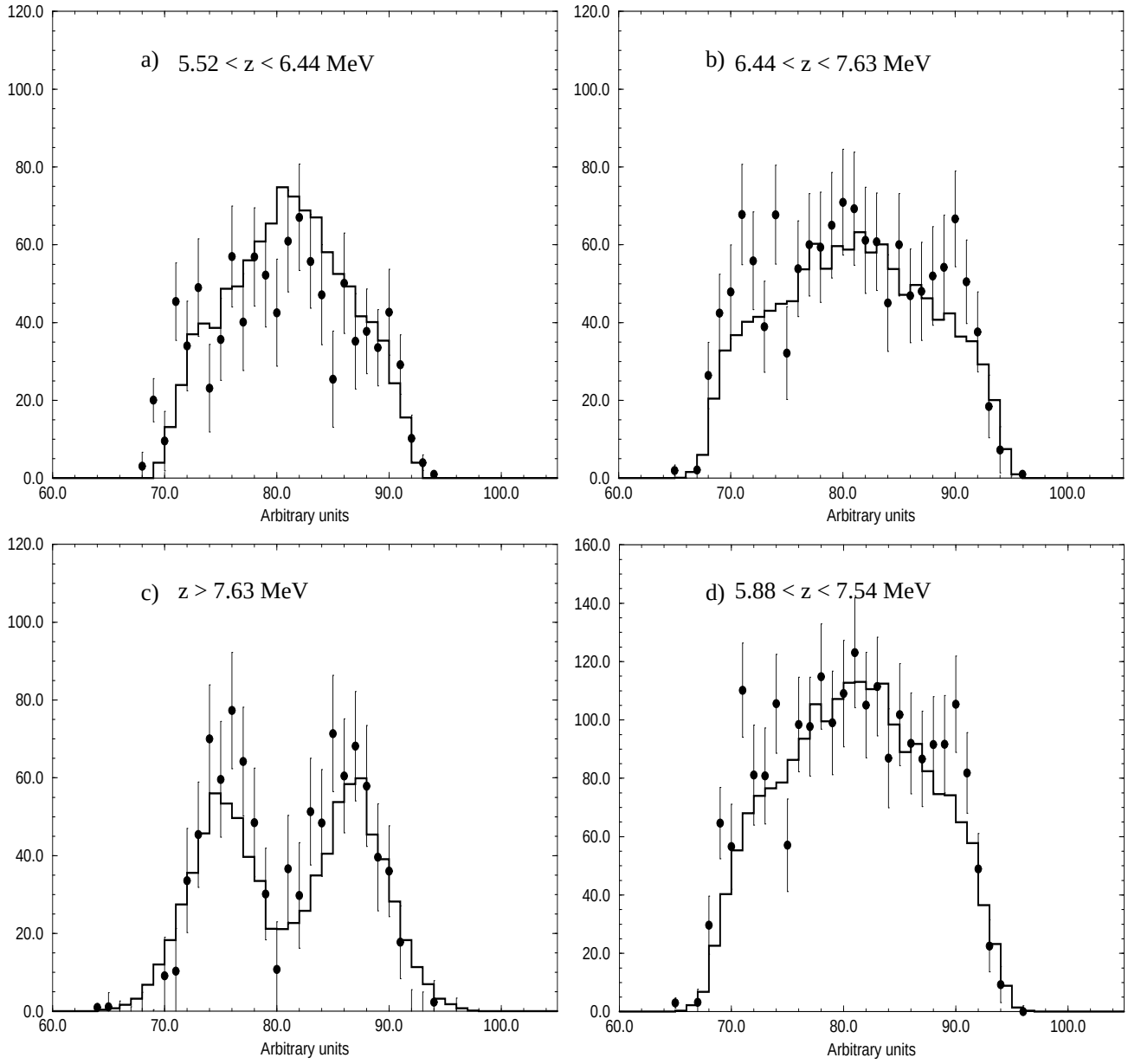

Figure 5.15: Figure shows different projections of slices on the energy-energy plot for normalised data and isotropic sequential emission. The values for the different slices are shown on the spectra where $z = E_{p1} + E_{p2}$. The x-axis is in arbitrary units with the central region corresponding to $E_{p1} = E_{p2}$.

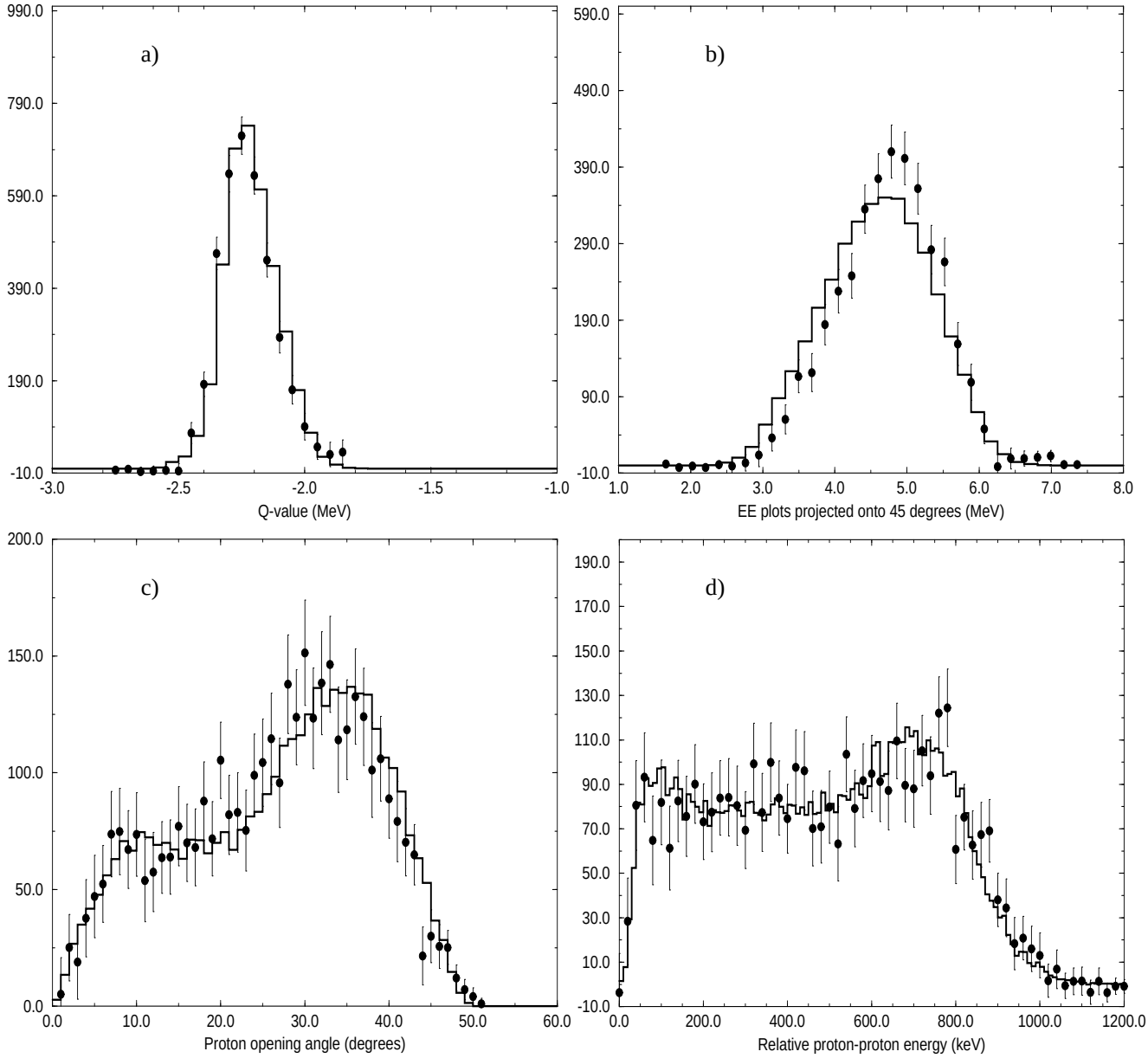

Figure 5.16: Comparison of data and isotropic sequential emission (a) Q-value of the reaction, (b) 45^o projection from energy-energy plots, (c) θ_{12} the two proton opening angle and (d) ϵ the relative energy of the pp pair.

5.4.2 ^{2}He emission

This section compares the data to the simulation for ^{2}He emission using the model described in section 4.3.

It is very clear from figures 5.17 and 5.18 that ^{2}He emission produces an energy continuum and not the distinct two peak structure observed in the data. More evidence of this appears in the slices of the energy-energy plots in figure 5.19(a)-(d) where the simulations produce flat structureless spectra. This is again particularly prominent in (c) where the data has a very clear two peak structure.

Figure 5.20(a) of the Q-value shows a good match as would be expected and (b) is as good a match as in the case for isotropic sequential.
The other two spectra 5.20(c) and (d) show that a ^{2}He contribution would result in an enhancement at small values of θ_{12} and ϵ. In the plot for θ_{12} the data shows a small enhancement around 8^o. If this is as a result of a ^{2}He contribution it is essential to improve the simulation for sequential emission as best as possible in order to estimate its level.

The following section introduces an anisotropic angular distribution into the sequential simulation based on the values obtained from the data.

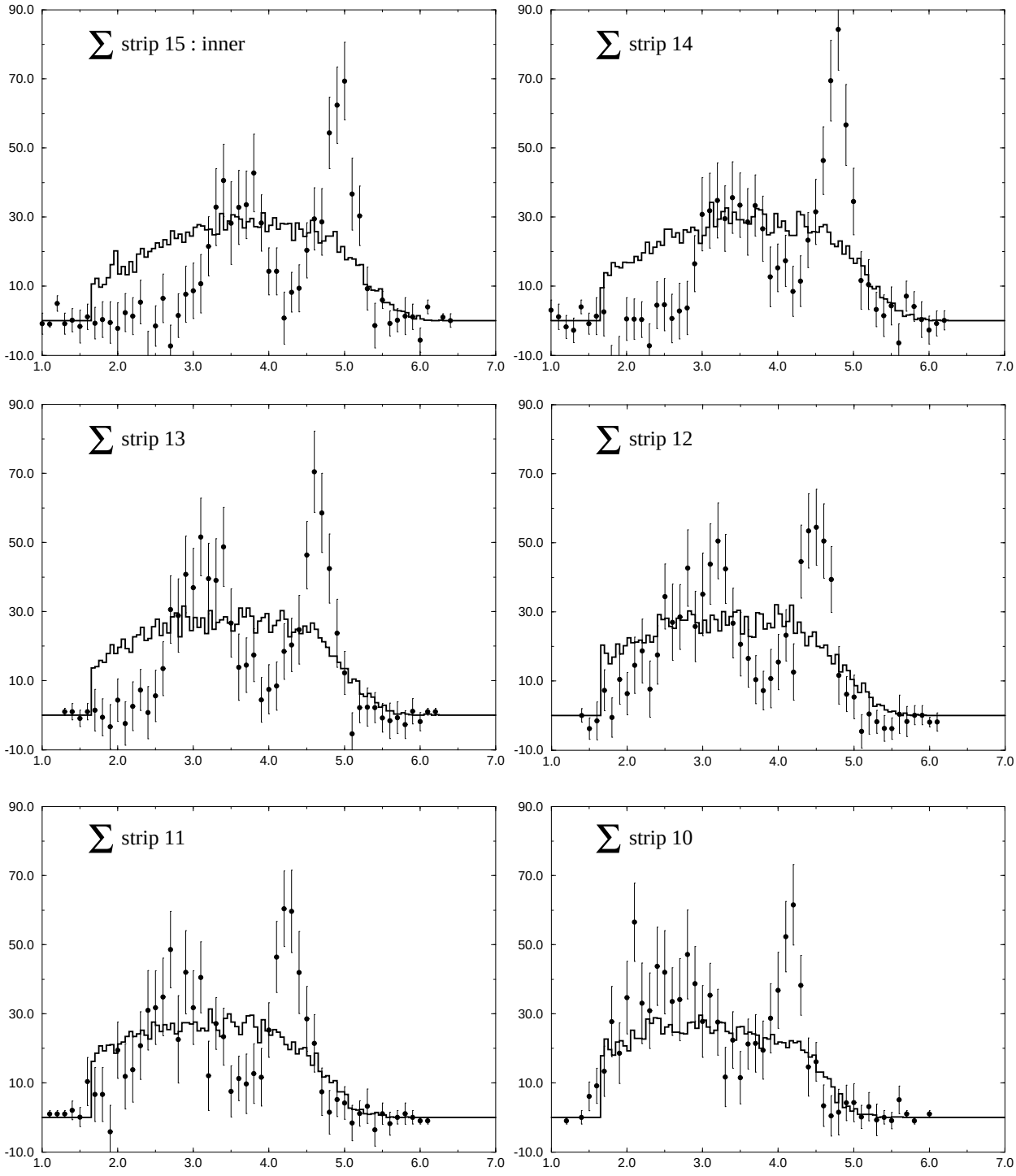

Figure 5.17: Normalised data shown by filled points with the solid line representing ^{2}He emission overlapped. The plots show the proton energy spectra for two proton events for the sum of the strips in each ring.

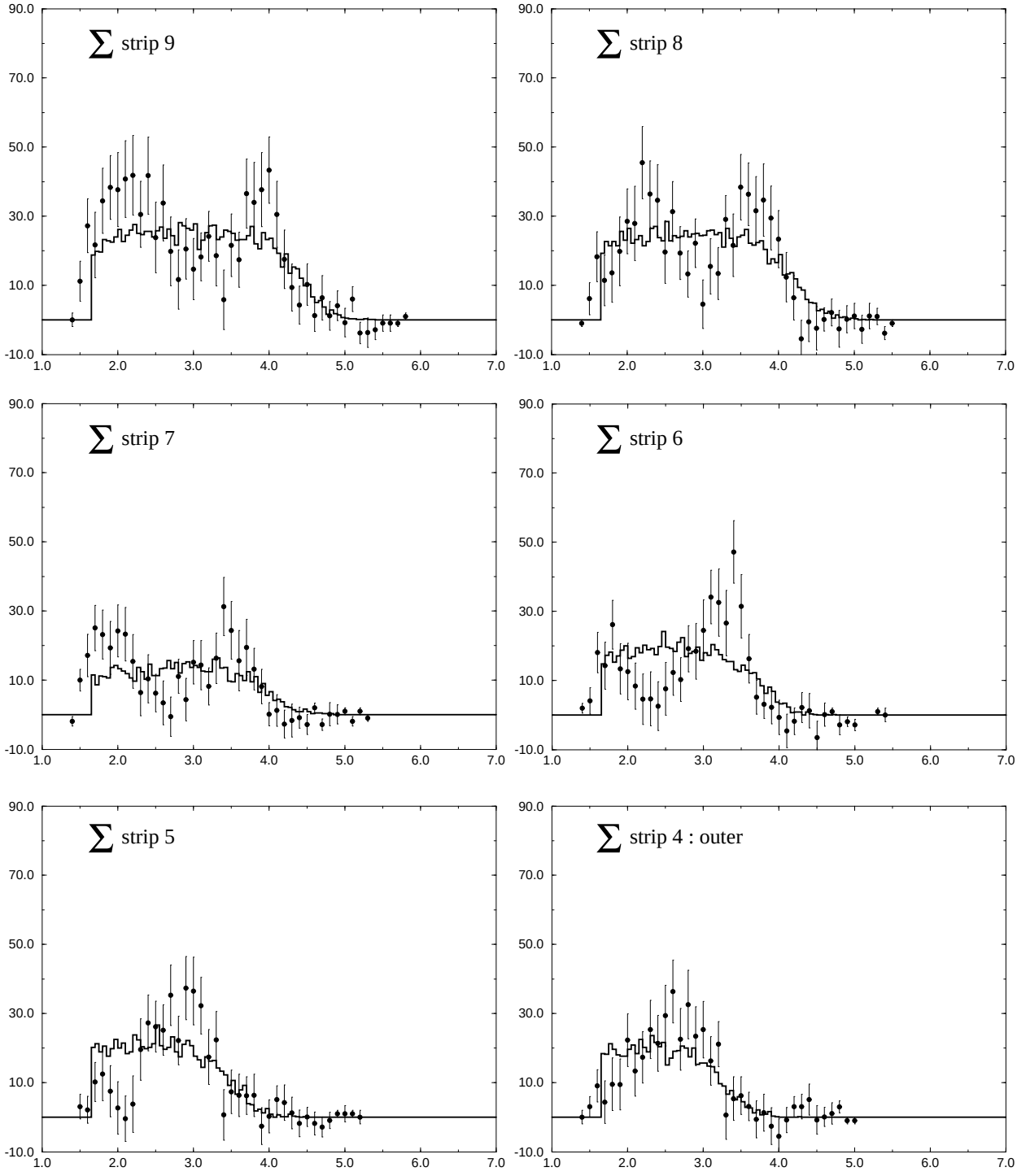

Figure 5.18: Normalised data shown by filled points with the solid line representing ^{2}He emission overlapped.

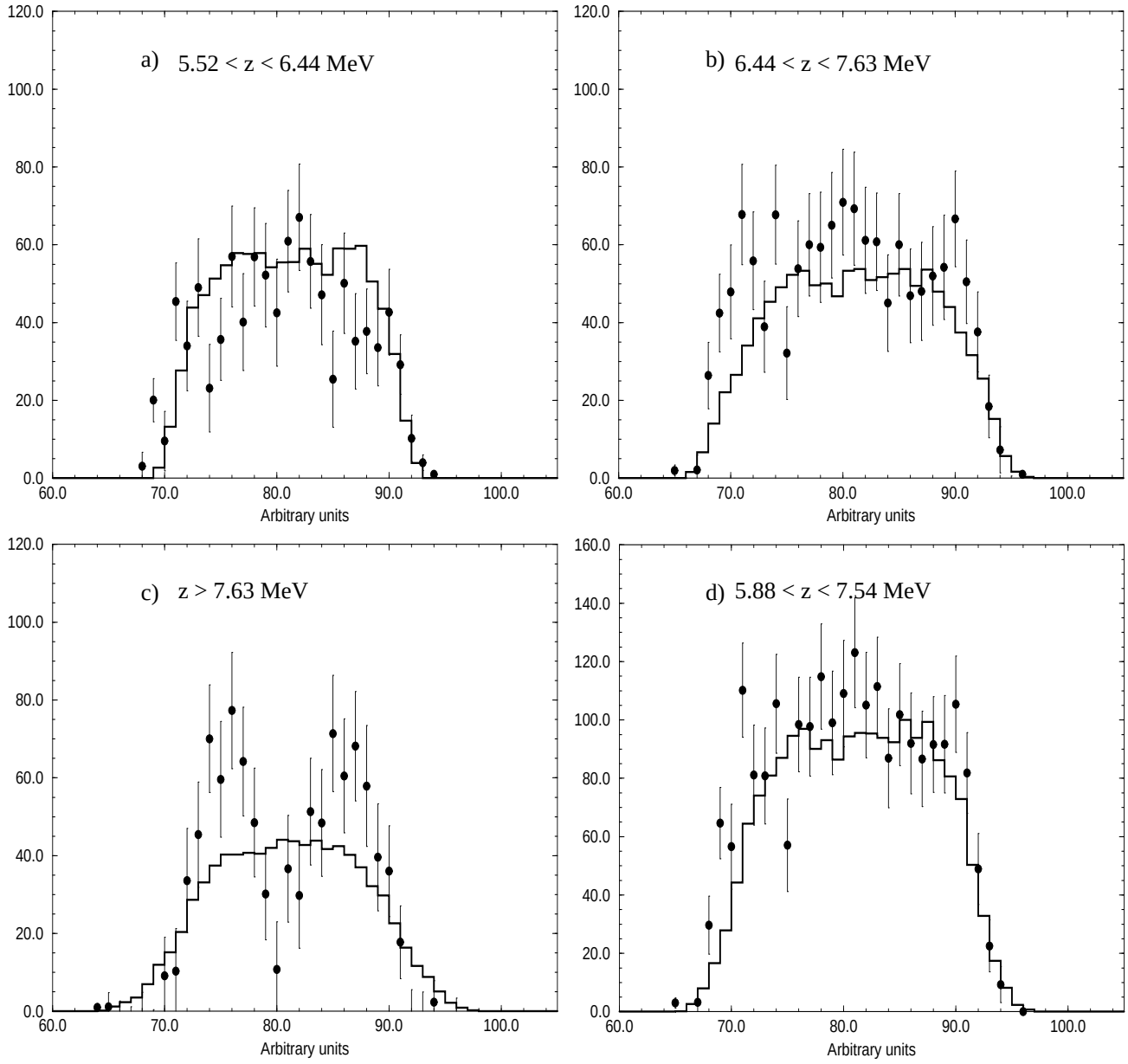

Figure 5.19: Figure shows different projections of slices on the energy-energy plot for normalised data and ^{2}He emission. The values for the different slices are shown on the spectra where $z = E_{p1} + E_{p2}$. The x-axis is in arbitrary units with the central region corresponding to $E_{p1} = E_{p2}$.

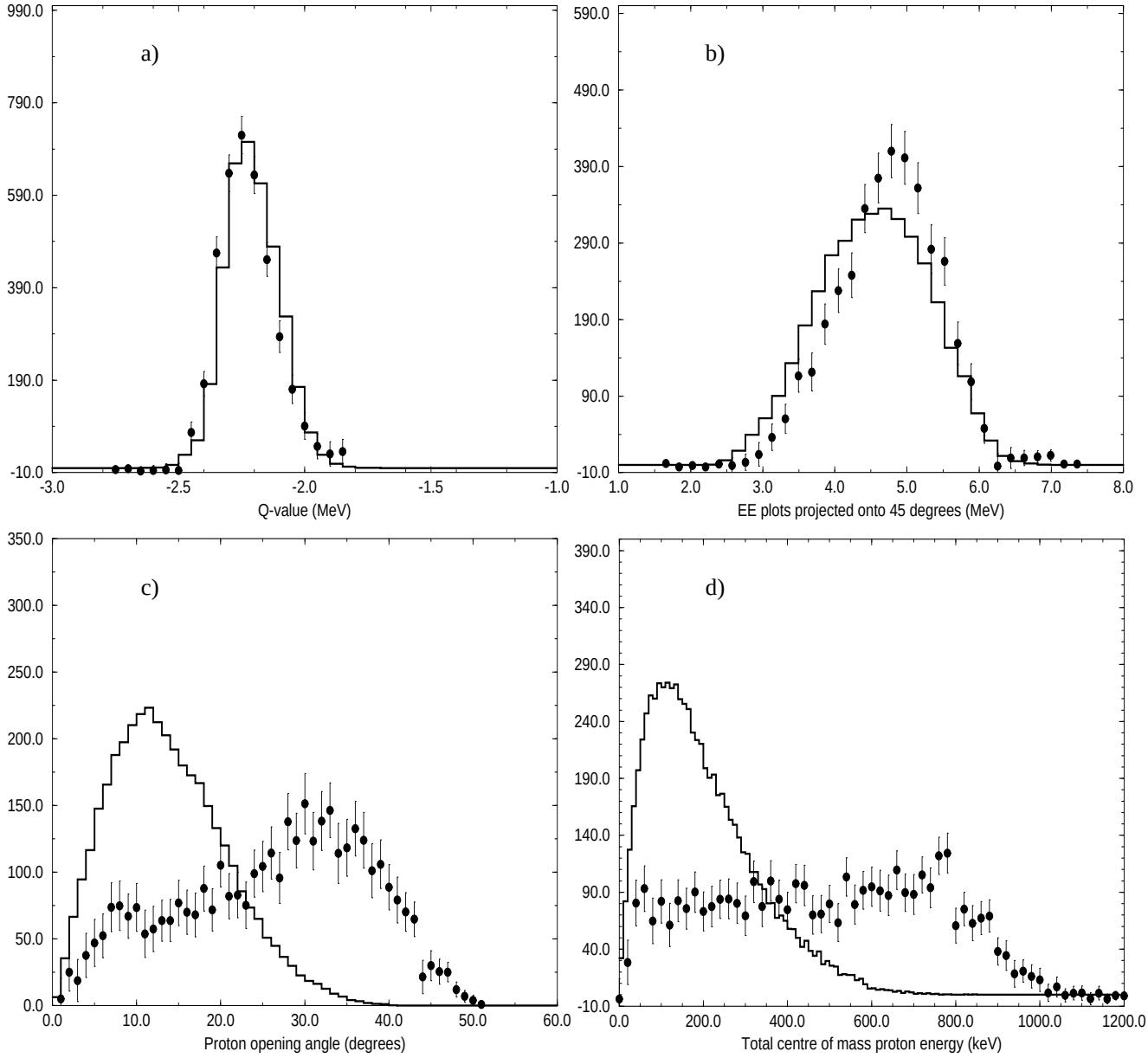

Figure 5.20: Comparison of data and ^{2}He emission for (a) Q-value of the reaction, (b) 45^o projection from energy-energy plots, (c) θ_{12} the two proton opening angle and (d) ϵ the relative energy of the pp pair.

5.4.3 Anisotropic sequential emission

The results from the previous two sections clearly show that the decay is dominantly a sequential one. The peak positions in the proton energy spectra in figures 5.13 and 5.14 can only be reproduced using the actual intermediate state in ^{13}N. Protons emitted with different energies produce different peaks and structures as discussed in section 4.5.1.

The comparison of the $p1$ counts in each ring for the normalised data (solid line) and isotropic sequential emission (dashed line) in figure 5.21 clearly shows that the simulation under compensates for inner angles (ring 15). The irregularity of the lines is explained by the fact that for some rings not all strips were used because of noise problems. This is the case for ring 7 which had three strips missing and ring 6 with two missing. These missing strips have been accounted for in the simulation.

On the assumption that the mechanism is predominantly sequential the fit can be improved by using an anisotropic angular distribution for the first proton $p1$. The distribution $W_{p1}(\theta^c_{p1})$ of the centre of mass angle of $p1$ with respect to the beam axis contains even Legendre polynomials with terms up to $l = 2$ and is expressed in the form

$$W_{p1}(\theta^c_{p1}) = \sum_{l=0}^{2} a_{2l} P_{2l}(cos(\theta^c_{p1})) \tag{5.1}$$

which is expressed in full as

$$W_{p1}(\theta^c_{p1}) = 1 + a_2 \frac{1}{2}(3cos^2(\theta^c_{p1}) - 1) + a_4 \frac{1}{8}(35cos^4(\theta^c_{p1}) - 30cos^2(\theta^c_{p1}) + 3) \tag{5.2}$$

The parameters a_{2l} contain the radiation parameters for particles as described in [Sat83]. The second proton $p2$ is emitted isotropically in the centre of mass frame of the recoiling ^{13}N nucleus.

In order to achieve a better fit the sequential simulation was altered to incorporate a distribution were the parameters a_2 and a_4 were varied until a best fit spectrum

for the data was achieved. The χ^2-fit, of the type discussed in section 5.5, over a range of values gave the best fit to data for the parameters $a_2 = 1.0$ and $a_4 = 0.6$, as shown in figure 5.22 by the dotted line. This plot shows a much better fit, however, rings 8, 12 and 14 are not as good as the others. Figures 5.23 and 5.24 show this improved correlation between the data and simulation in the energy spectra for the different rings although some plots are not reproduced perfectly.

The simulation for the slices in figure 5.25 (a) and (c) are slightly better than those for isotropic with (c) now reproducing the number of counts as well as the peak positions. A comparison of figures (b) and (d) with the corresponding plots for isotropic emission show that the central peak is not reproduced giving a flatter structure. This results from the angular distribution not being recreated exactly and it was found that these spectra are very sensitive to this.

The most convincing figure is 5.26(b) with the simulation agreeing very well with the data. Figures (c) and (d) also show a better agreement than was the case for isotropic emission. The next section presents a statistical analysis of these two plots, θ_{12} and ϵ, to determine the level at which there could be a ^{2}He contribution.

The conclusions drawn from the figures shown in this section are that the introduction of anisotropic emission into the simulation has overall improved the fits to the data.

A final point to make is that this angular distribution is calculable but after discussions with R. Satchler and I. Stone [Sat95, Sto95] it was found to be too complex requiring the use of optical models.

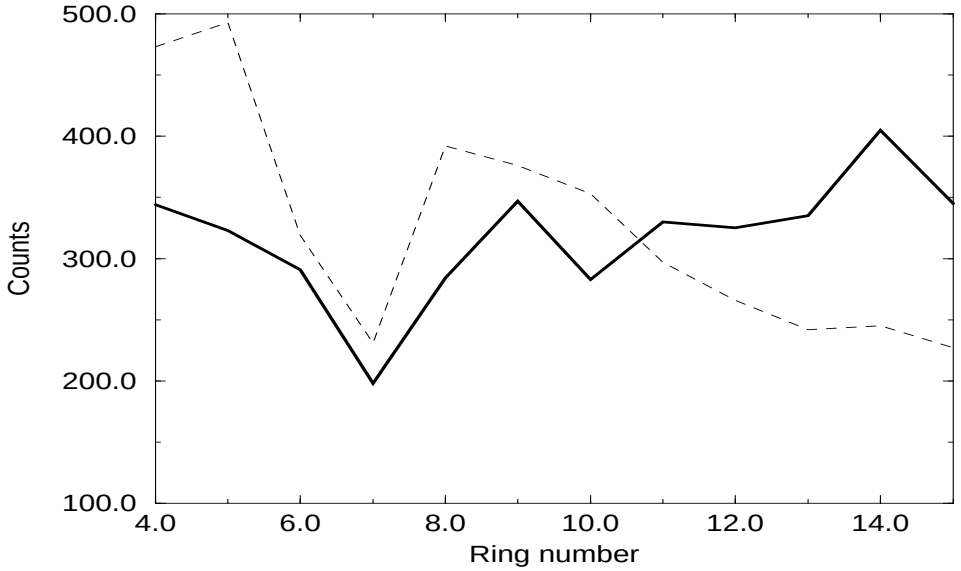

Figure 5.21: *p*1 *angular distribution for normalised data shown with the solid line compared to the distribution obtained using isotropic emission in the sequential simulation (dashed line).*

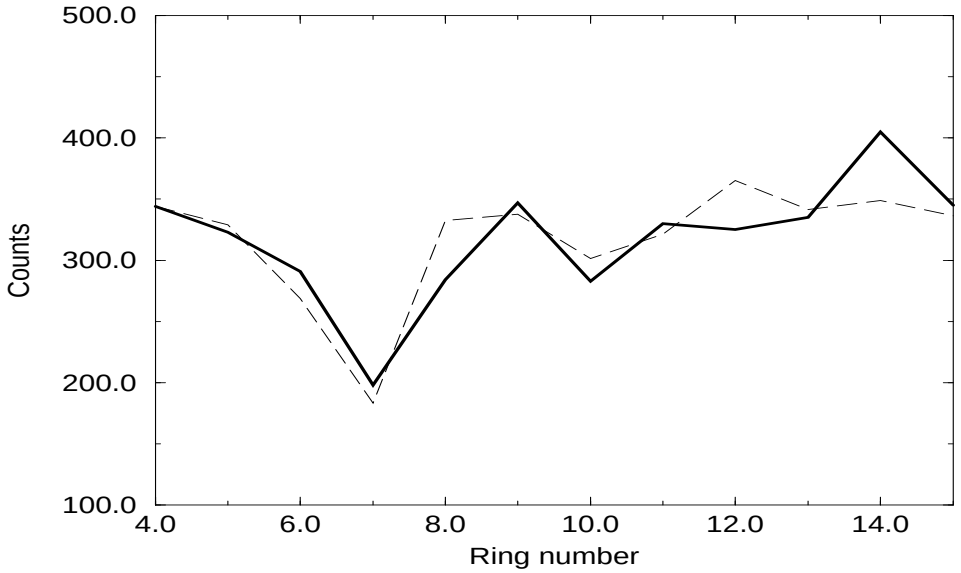

Figure 5.22: *p*1 *angular distribution for normalised data shown with the solid line compared to the distribution obtained using anisotropic emission using equation(5.1) with parameters* $a_2 = 1.0$ *and* $a_4 = 0.6$ *(dashed line).*

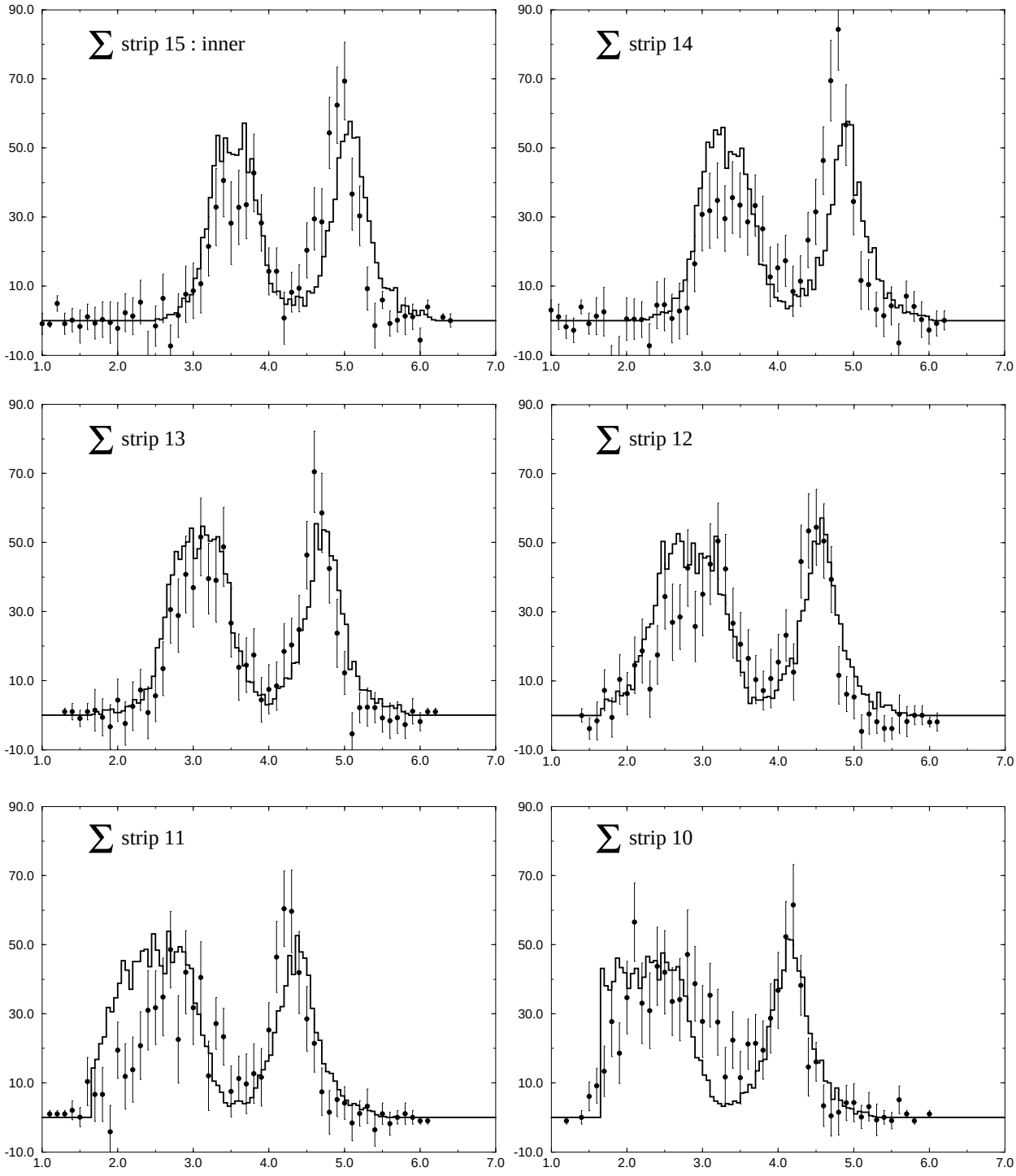

Figure 5.23: Normalised data shown by filled points with the solid line representing anisotropic sequential emission overlapped. The spectra show the proton energy spectra for two proton events for the sum of the strips in each ring.

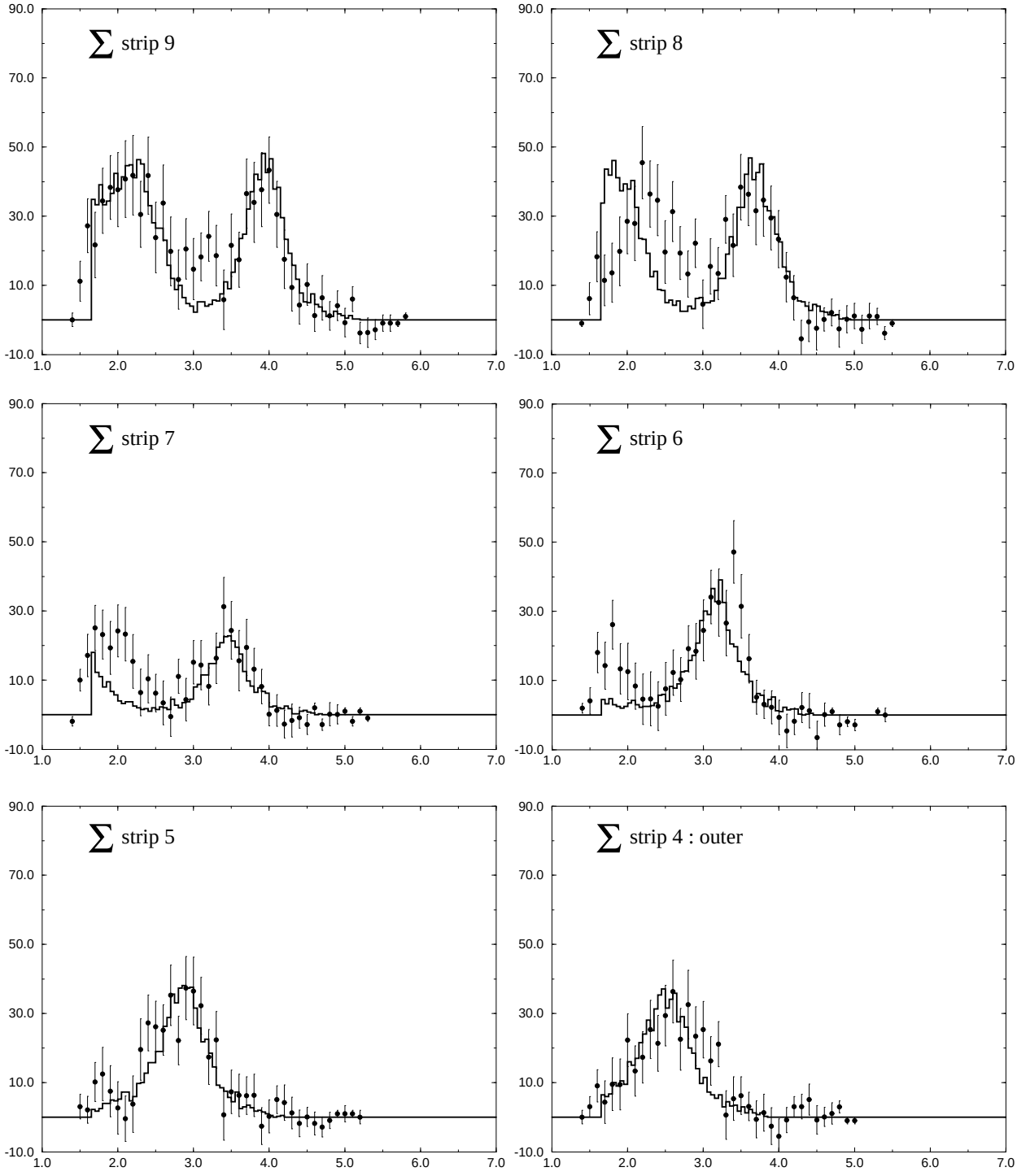

Figure 5.24: Normalised data shown by filled points with the solid line representing anisotropic sequential emission overlapped.

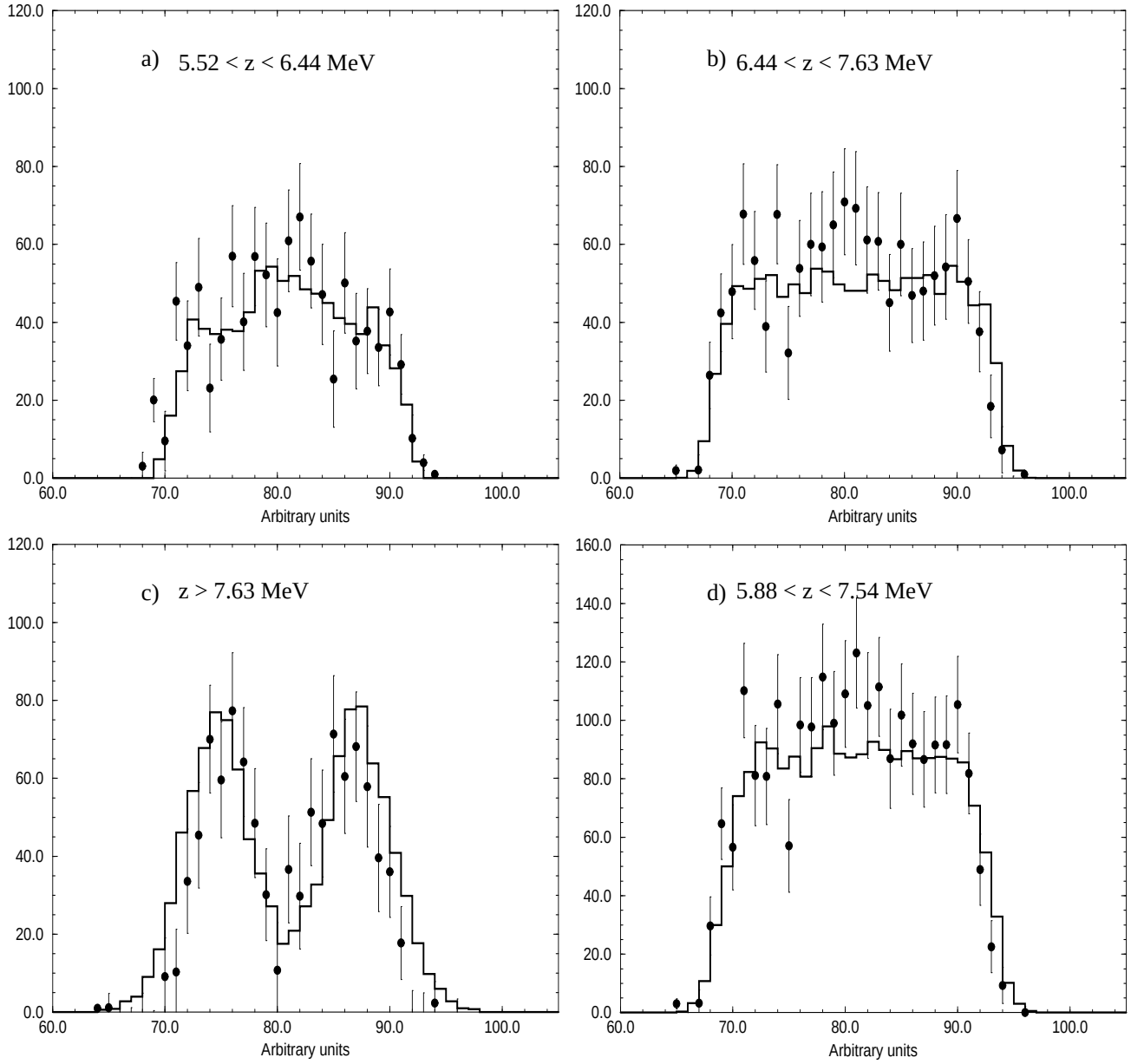

Figure 5.25: Figure shows different projections of slices on the energy-energy plot. The values for the different slices are shown on the spectra where $z = E_{p1} + E_{p2}$. The x-axis is in arbitrary units with the central region corresponding to $E_{p1} = E_{p2}$.

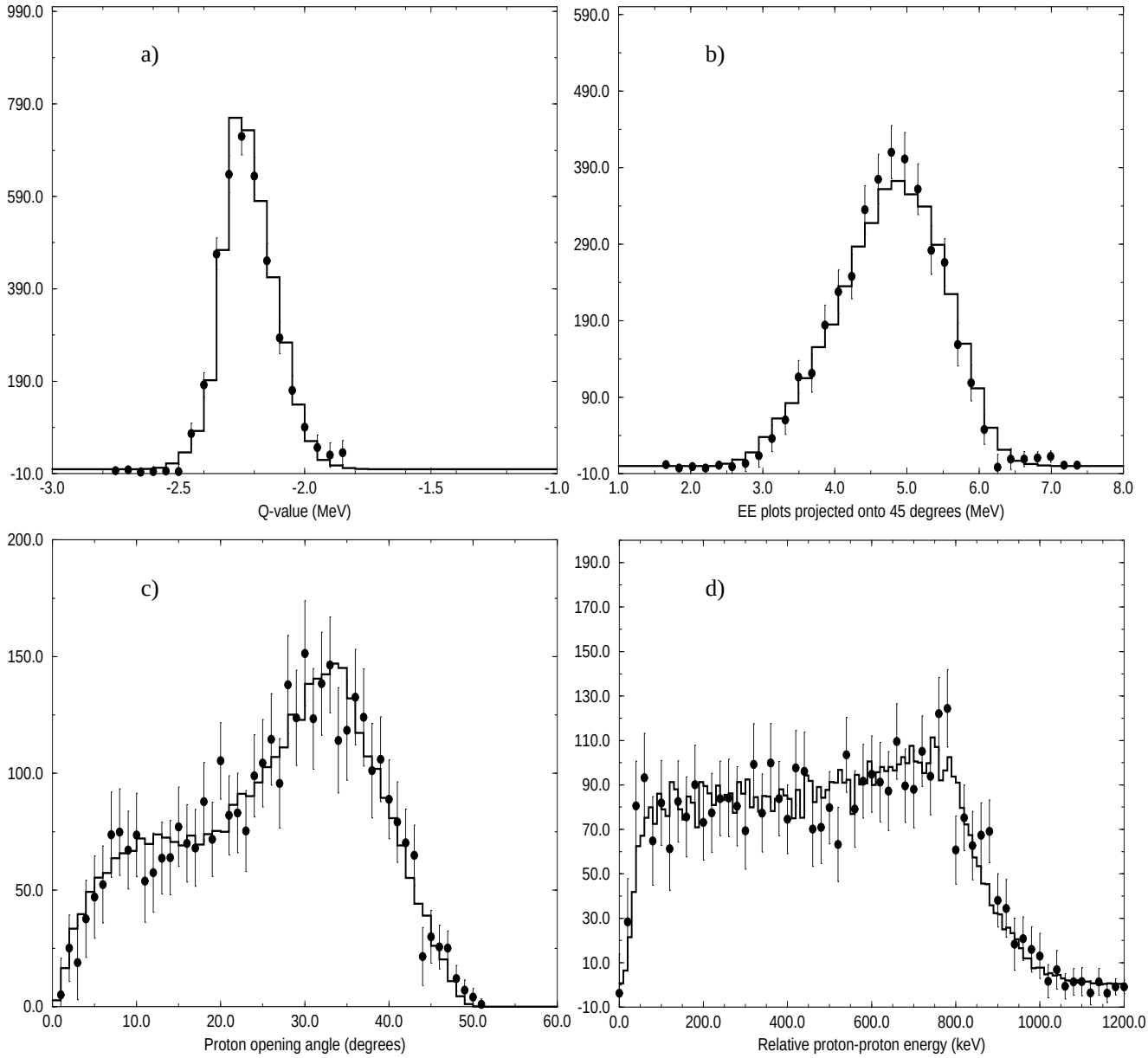

Figure 5.26: (a) Q-value of the reaction, (b) 45^o projection from energy-energy plots, (c) θ_{12} the two proton opening angle and (d) ϵ the relative energy of the pp pair.

5.5 χ^2 fits to data

The quantity χ^2 is defined as the squared difference between the observed values and the theoretical predictions, suitably weighted by the errors of the measurement [Bar];

$$\chi^2 = \sum_{i=1}^{N} \left(\frac{y_i^{obs} - y_i^{the}}{\text{expected error}}\right)^2 \tag{5.3}$$

In this section we concentrate on the proton-proton opening angle θ_{12} and relative energy ϵ. The χ^2 minimum is determined by fitting different amounts of the sequential and ^{2}He models to the data. This has been carried out for the two sequential models, namely isotropic and anisotropic. From these the level of ^{2}He contribution is estimated.

The best χ^2-fits for the isotropic and anisotropic emission both give the result that the data is best reproduced with 100% sequential and 0% ^{2}He. These fits are shown in figures 5.27 and 5.28, where the data is shown as the black circles and the fit is the dashed line.

The best overall fit to the data is achieved using 100% anisotropic sequential emission. Figures 5.29 to 5.32 show the effect of adding a ^{2}He contribution to the anisotropic sequential model. This contribution has been overlapped onto the spectra to show its size. These plots clearly show how a ^{2}He enhancement would effect the spectra. The plot which shows a 5% ^{2}He contribution produces a fit which is acceptable within errors. The corresponding fit for a 10% contribution overestimates at low values and underestimates at high values, thus, not producing an acceptable fit. Hence an upper limit of a 5% ^{2}He contribution has been set for the data with a 95% confidence limit.

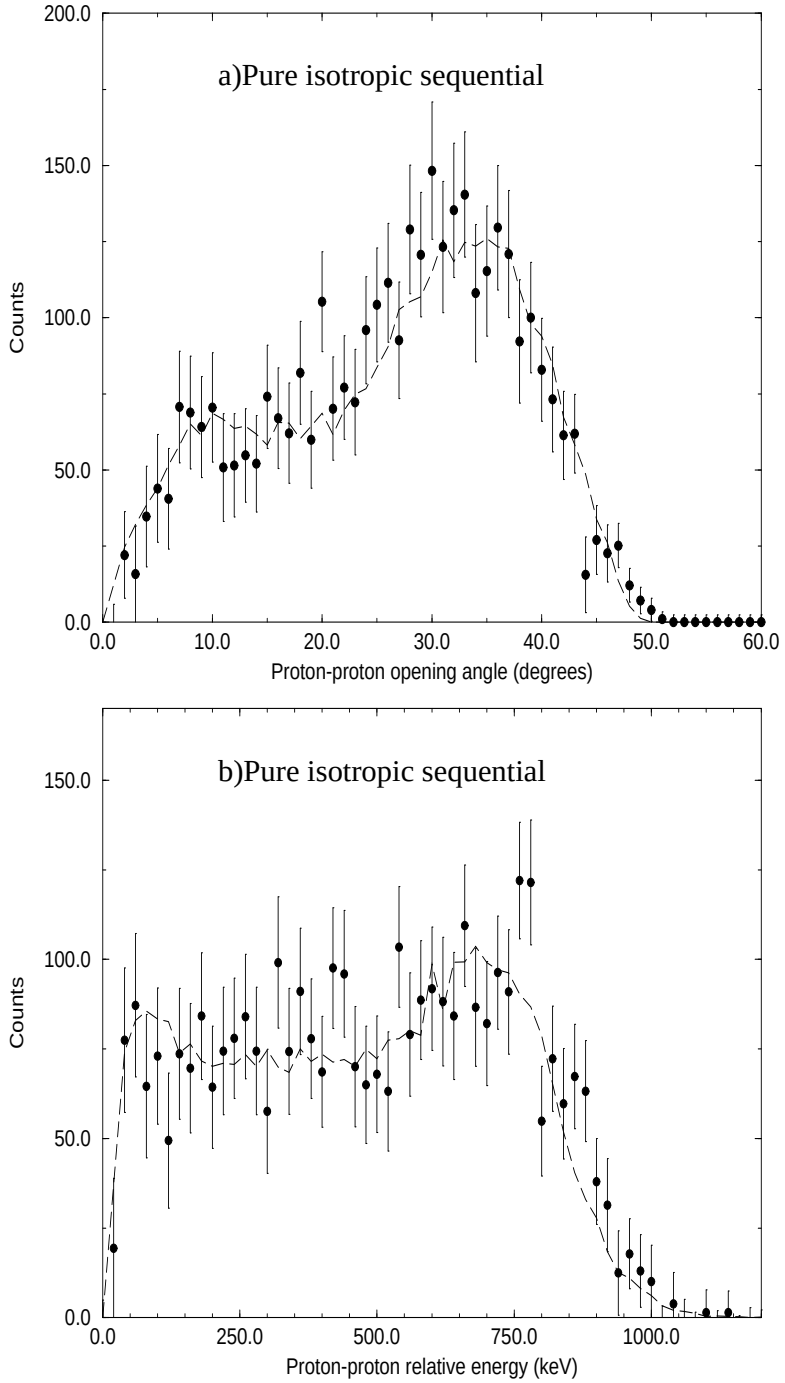

Figure 5.27: *Figure shows best* χ^2*-fits to data using isotropic sequential and* ^2He *emission simulations for* θ_{12} *and* ϵ*. Best fits come from 100% sequential.*

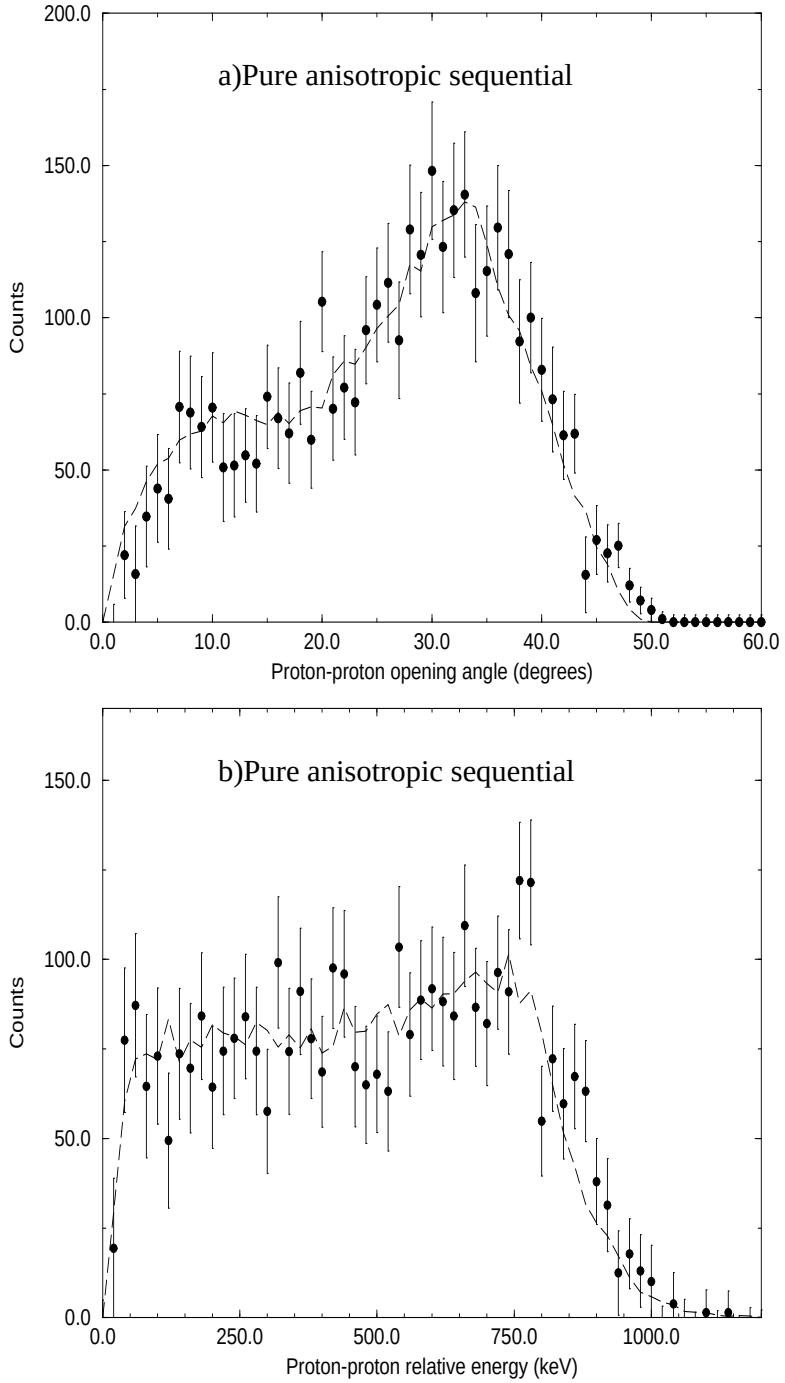

Figure 5.28: *Figure shows best χ^2-fits to data using anisotropic sequential and ^{2}He emission simulations for θ_{12} and ϵ. Best fits come from 100% sequential.*

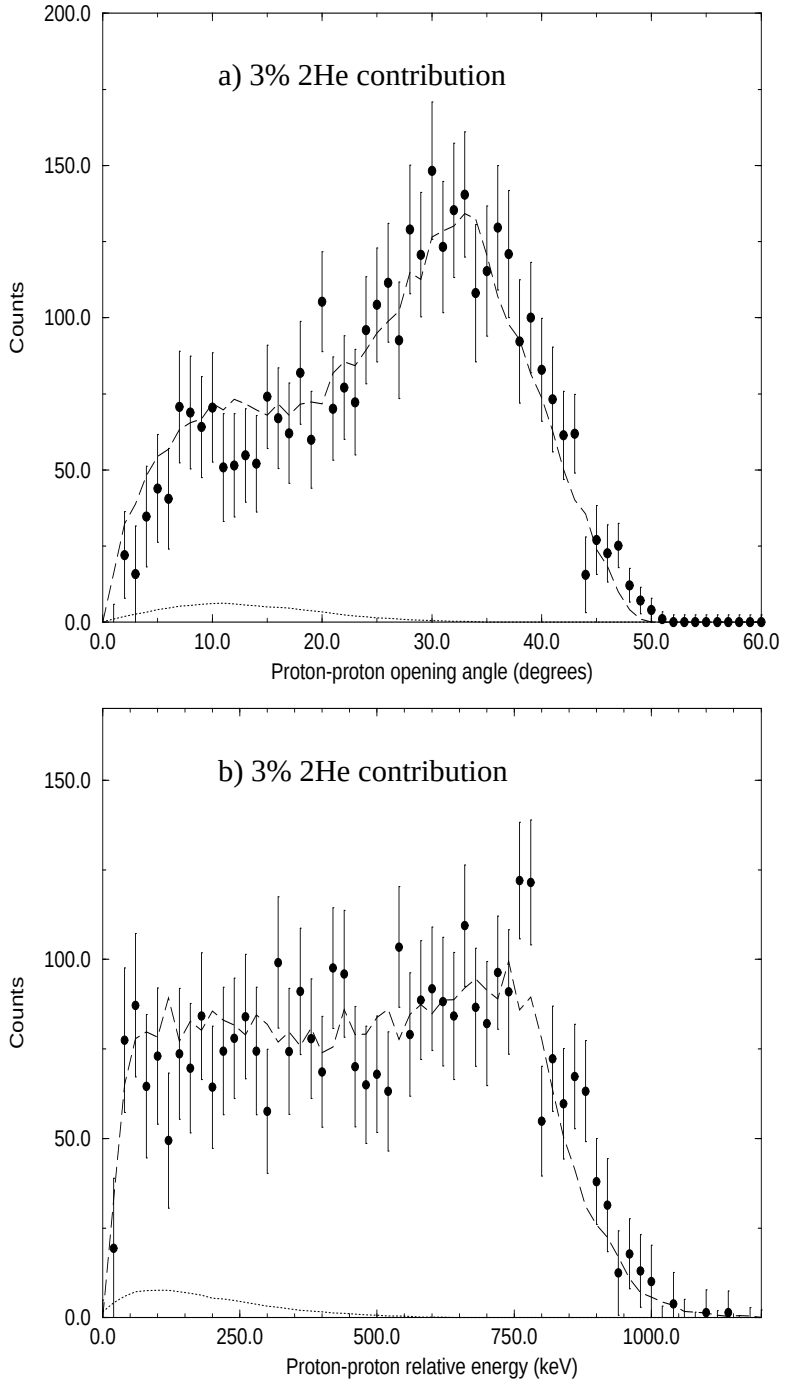

Figure 5.29: *Data shown with a fit made up of 97% anisotropic sequential emission plus a 3% ^{2}He contribution which is also shown separately.*

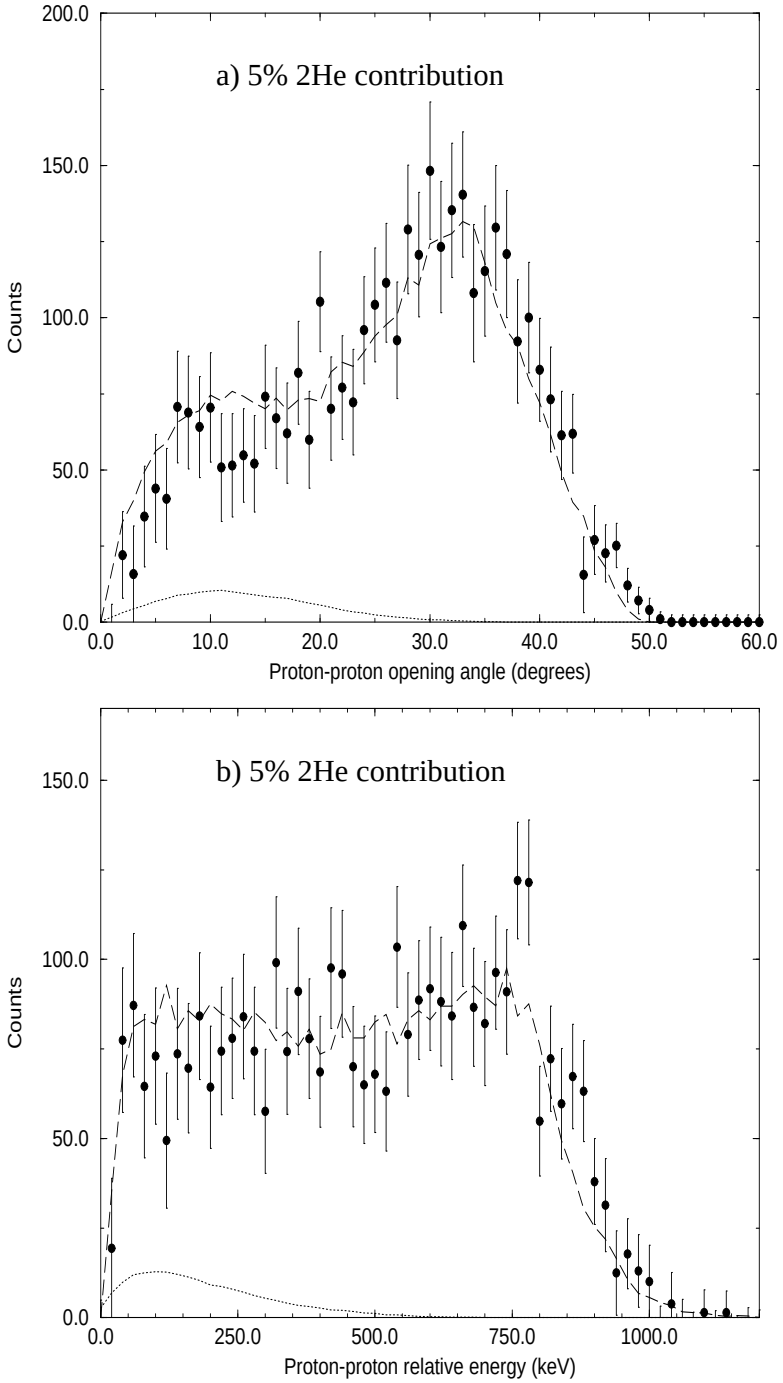

Figure 5.30: *Data shown with a fit made up of 95% anisotropic sequential emission plus a 5% ^{2}He contribution which is also shown separately.*

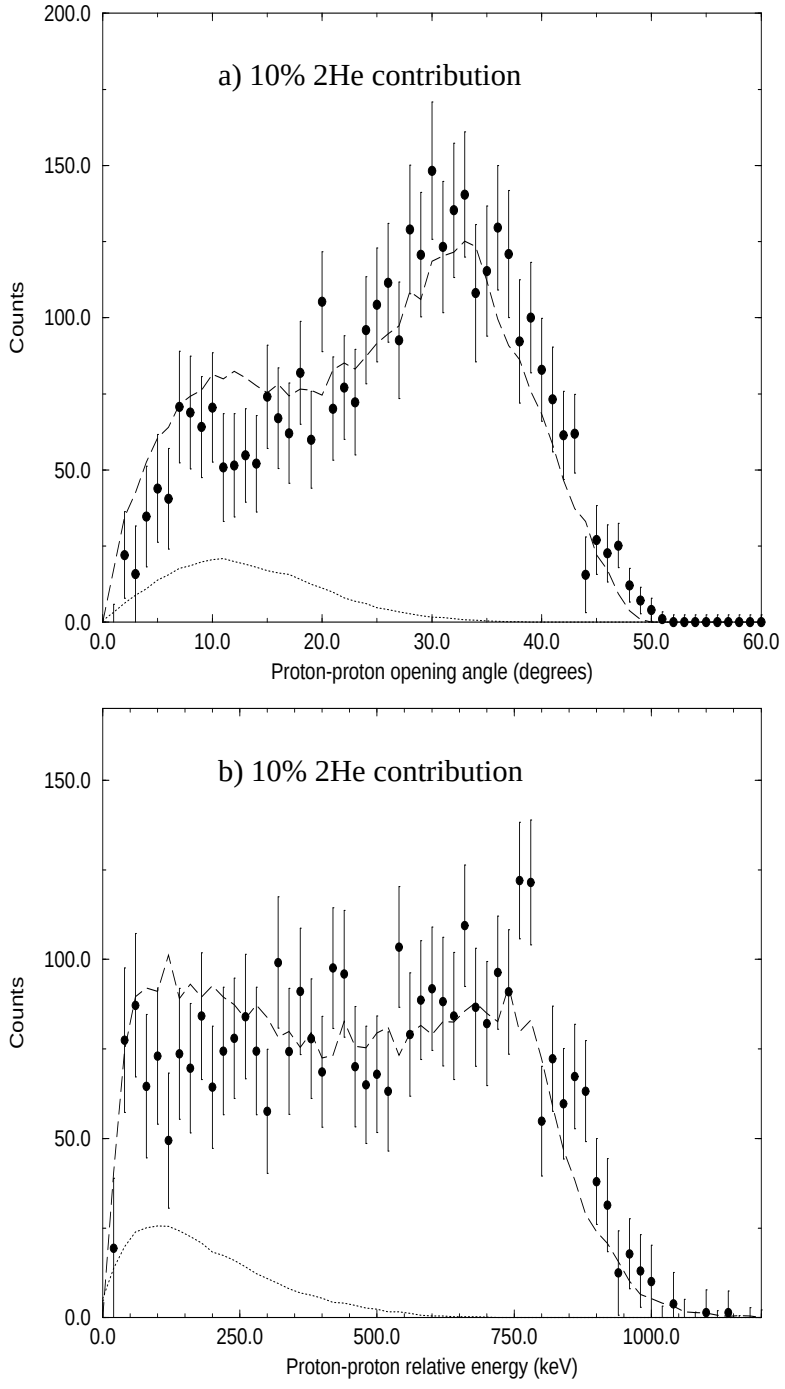

Figure 5.31: *Data shown with a fit made up of 90% anisotropic sequential emission plus a 10% ^{2}He contribution which is also shown separately.*

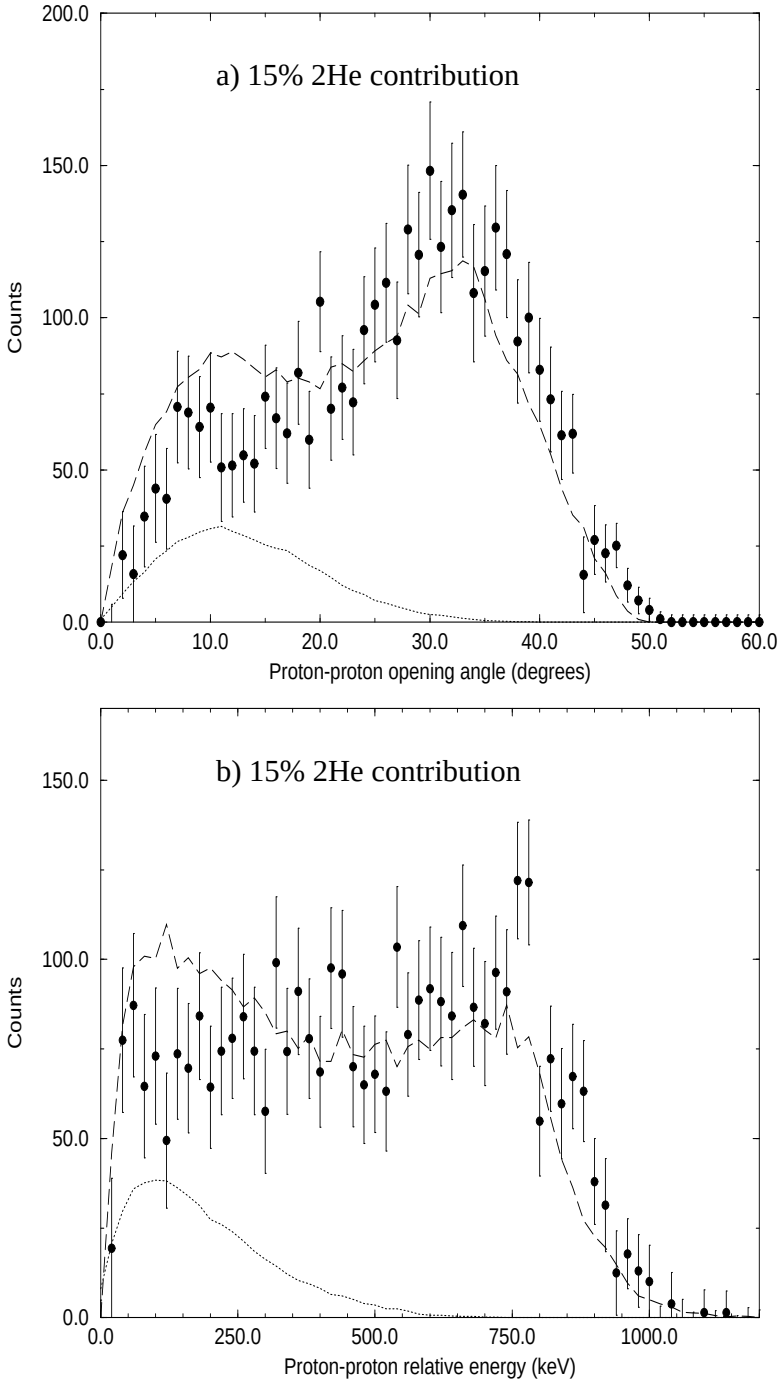

Figure 5.32: *Data shown with a fit made up of 85% anisotropic sequential emission plus a 15% ^{2}He contribution which is also shown separately.*

5.6 Observed two proton width

The observed two proton width is calculated using the following expression, valid for a resonance with a width smaller than the resonance energy, where Y is the reaction yield per incident nucleus [Rol88]

$$Y(E_0) = \frac{\lambda^2}{2\pi}\omega\gamma\frac{m_t + m_p}{m_t}\frac{1}{\epsilon}[\arctan(\frac{E_0 - E_R}{\Gamma/2}) - \arctan(\frac{E_0 - E_R - \Delta}{\Gamma/2})] \quad (5.4)$$

where the following are defined by

λ = $\frac{(m_p+m_t)}{m_t}\frac{h}{\sqrt{(2m_pE_l)}}$, the de Broglie wavelength

γ = $\frac{\Gamma_a\Gamma_b}{\Gamma}$, the strength of the resonance

m_t, m_p = masses of target and projectile

E_0 = incident energy of the projectile

E_R = resonance energy

Γ = total resonance width

Δ = energy loss of projectile in target

ω = $\frac{2J+1}{(2J_1+1)(2J_2+1)}$, the statistical factor

ϵ = $\frac{1}{n}\frac{dE}{dx}$, the stopping cross-section

n = $\frac{\nu_a\rho N_A}{A}$, the number of active nuclei per m^3

To complete the definitions ν_a, ρ, N_A and A are number of active atoms per molecule, density of target, Avogadro's number and molecular weight of the target respectively.

With the resonance corresponding to 43.6 MeV, a beam energy of 45 MeV and a beam energy loss of 2.8 MeV in the CH_2 target the equation(5.4) becomes

$$Y(E_0) = \frac{\lambda^2}{2\pi}\omega\gamma\frac{m_t + m_p}{m_t}\frac{1}{\epsilon}[2.51] \quad (5.5)$$

For a total of T incident beam particles, a two proton detection efficiency of e_{2p}

and $\gamma = \Gamma_{2p}$ then the total yield Y_{TOT} is given by

$$Y_{TOT} = 2.51 e_{2p} T \frac{\lambda^2}{2\pi} \omega \Gamma_{2p} \frac{m_t + m_p}{m_t} \frac{1}{\epsilon} \tag{5.6}$$

With the values $Y_{TOT} = 3830 \pm 400$, $T = 1.401 \times 10^{12}$ and $e_{2p} = 8.08\%$ inserted into equation (5.6) a partial width of $\Gamma_{2p} = 105 \pm 17$ eV is given. When the dead time of 19% is accounted for the observed experimental width increases to 125±20 eV. This represents a branching ratio of 0.16% for emission of a proton to the intermediate state in ^{13}N. The 5% upper limit obtained for a ^{2}He contribution corresponds to a partial width of 6 eV.

The next section discusses the different values which have been predicted for the width using the methods described in chapter 2.

5.7 Predicted widths

5.7.1 Proton widths

The proton widths have been calculated using the model discussed in section 2.5. The predicted width depends on the first proton emitted from the 7.77 MeV state in ^{14}O in the sequential process since the intermediate state in ^{13}N has a proton branching ratio of nearly 100% [Ajz91]. Thus the width is calculated using a proton with energy of 775 keV and angular momentum $l = 2$. The values obtained for the width depend on the nuclear radius R_n. Table 5.1 demonstrates this and gives the calculated widths using a spectroscopic factor of unity.

Calculations which incorporate a model for the nuclear potential give values ranging from 2.0 keV to 4.2 keV depending on the choice of potential [Pag90]. Taking an average of these values and those in table 5.1 gives 3±1 keV.

The experimentally observed width for this decay is 125±20 eV which suggests a spectroscopic factor of $\theta^2 = 0.04 \pm 0.006$.

R_o	Predicted widths for proton emission (keV)
1.2	2.42
1.3	3.23
1.4	4.23

Table 5.1: *Predicted widths for an $l = 2$ proton with energy 775 keV emitted from the 7.77 MeV excited state in ^{14}O.*

5.7.2 ^{2}He widths

For the ^{2}He case as described in section 2.4 two methods can be used for this calculation. The values obtained for both of these methods depend on the value of R_o which appears in the definition for the nuclear radius in equation(2.14), thus, different values have been used for this number varying from 1.2fm to 1.4fm. The two methods are referred to as R-matrix and final state interaction.

The results are summarised in table 5.2 using a spectroscopic factor of unity for the actual case where the angular momentum is $l = 2$ and for the case where $l = 0$ to demonstrate the difference that this makes.

	l =2		l = 0	
	Predicted width, $\Gamma_{\rm dip}$ (eV)		Predicted width, $\Gamma_{\rm dip}$(eV)	
R_o(fm)	R-matrix	FSI	R-matrix	FSI
1.2	295	9.95	12.3×10^3	431
1.3	427	14.43	14.7×10^3	522
1.4	595	20.23	17.6×10^3	627

Table 5.2: *Theoretical predictions for ^{2}He widths, $\Gamma_{\rm dip}$ using both R-matrix and FSI methods. Results are shown for $l = 2$ and $l = 0$ ^{2}He over a different range of nuclear radii.*

These results show that, as reported by Kryger *et al.* [Kry95], that the R-matrix

approach produces a value larger than that for FSI because it treats the ^{2}He as a long lived particle which it is not, thus the FSI values are used.

Using the FSI model we obtain a width of approximately 15±5 eV when a spectroscopic factor of unity is used. A spectroscopic factor of unity therefore corresponds to a 12% ^{2}He contribution which had been discounted in section 5.5 and Thus an upper limit on the spectroscopic factor of $\theta^2 = 0.4$, corresponding to a 5% contribution, is given.

Calculations for this state have been performed by B.A. Brown [Bro95] using the method outlined in [Bro91]. The spectroscopic factor has been estimated using the cluster overlap approximation using a two proton cluster wave function. The calculations for the two lowest 2^+ states in ^{14}O give spectroscopic factors of 0.0067 and 0.64 respectively. The total spectroscopic factor is calculated to be $\theta^2 = 0.44$. If the states are equally mixed the value would be split equally between them giving $\theta^2 = 0.22$ for both. With this value for the spectroscopic factor the calculated decay width for an $l = 2$ ^{2}He emission is $\Gamma_{dip} = 3.3\pm1$ eV. This is within the 5% upper limit obtained from the data.

As a final remark in this section worth pointing out is the effect that the angular momentum has on the width. Predictions for $l = 0$ ^{2}He emission are contained in table 5.2 an average for FSI gives a width of ∼500 eV which is well above the observed sequential width in this experment.

5.8 Concluding discussion

The search for two proton emission from the 7.77 MeV excited state in ^{14}O described in this thesis has been a very rewarding one. The results of the commissioning run identified a small component for two proton emission but it was impossible to identify the mechanism due to the large background from evaporation protons. The use of a veto detector in the follow-up experiment considerably reduced this background. The results from this second experiment have clearly shown that the dominant decay mechanism is the sequential emission of two protons via the 2.37 MeV state in ^{13}N. To reproduce the data it is necessary to have an energy correlation between the two protons which corresponds precisely to that produced by this intermediate level. The sequential process has a proton with angular momentum $l = 2$ emitted first followed by an $l = 0$ proton. The data have been used to improve the simulations by introducing an anisotropic angular distribution for the first proton into the simulations. The data were used because of the complexity involved in the theoretical calculation of the distribution [Sat95, Sto95].

The width for the sequential two proton emission depends on the emission of the first proton since the intermediate level is a ~100% proton emitter. The results of the experiment give a width of 125±20 eV for this decay mode. This corresponds to a partial half-life of 3.6×10^{-18}s and a 0.16% branching ratio. Predictions for this width using the method described in chapter 2 give a value of 3±1 keV which gives a spectroscopic factor of $\theta^2 = 0.04$.

An upper limit for ^{2}He emission has been set at 5% which corresponds to ~6 eV. Predictions using the final state interaction approach described in chapter 2 give a value of 15±5 eV, using a spectroscopic factor of unity. Hence an upper limit for the spectroscopic factor of $\theta^2 = 0.4$ (95% confidence limit) can be set which is above the value of 0.22 predicted by Brown [Bro95].

It is interesting to compare the experiment of Kryger *et al.* (desribed in section 1.2.1) with this experiment because of the similarities. Both used radioactive ion beams and studied an oxygen isotope. Kryger *et al.* studied ground state two proton emission from ^{12}O, an isotope two steps further from stability than ^{14}O. They moved away from stability to make the two protons unbound whereas in this experiment we did so by populating a particular state. Our technique whereby the radioactive ion beam is used to directly populate the state has produced approximately ten times the statistics obtained by Kryger *et al.* as can be seen in figure 1.4. The results from Kryger *et al.* deduced a 7% upper limit for ^{2}He emission from the ground state in ^{12}O. This was dependent on the location of the ground state of ^{11}N. Recent calculations [The95] predict that this may be significantly lower than the value used which led to the 7% ^{2}He upper limit. This would indicate that this may need to be recalculated as well as the conclusions about the decay mode.

Bocharev *et al.* [Boc92] studied two proton emission from ^{6}Be ($\rightarrow \alpha + p + p$). The widths of the states in the transitions were of the same order of magnitude as the transition energies and the decay has been understood using a three-body cluster model. Indeed, it is difficult to imagine that this breakup could be considered as being the emission of a ^{2}He from a host system so it is perhaps not surprising a model which accounted for the interaction between all the final particles was required. Any contribution of this three-body decay in this present experiment would not change the conclusions which have been made since it would be expected to be present isotropically.

The amount of interest which has been shown in this experiment by other physicists is a measure of the general enthusiasm which exists in this field at present. Within the theoretical community I. Thompson is working on a code which will be able to model the three-body cluster decay mechanism for the ^{14}O case [Thp95]. W. Nazarewicz *et al.* have calculated the diproton partial half-lives in the mass region around doubly-magic ^{48}Ni [Naz95]. Their conclusions are that the main

factor in determining the hal-life is Q_{2p}. In the energy range $0.5 \leq Q_{2p} < 2.0$ MeV the half-life vary by more than 22 orders of magnitude and, thus, the energy window for the experimental observation of diproton emitters is very small. The calculations predict the two proton drip-line to lie between ^{42}Cr and ^{44}Cr, ^{44}Fe and ^{46}Fe and ^{48}Ni and ^{50}Ni.

As yet ^{2}He emission remains undetected but more and more experiments have been planned and are being carried out. One of these recently attempted at Louvain-la-Neuve was the study of the decay mechanism from ^{17}Ne [Woo94b]. The low lying states are two proton unbound with the ground state in ^{15}O. The protons can be emitted by a sequential decay mechanism via a number of states in ^{16}F or by ^{2}He emission. The first excited state in ^{17}Ne is bound to proton emission and unbound to two proton emission. However for this case $Q_{2p} \simeq 0.38$ MeV and the ^{2}He would carry two units of angular momentum which suggests that this may be an extremely weak channel.

My final concluding remarks are that this has been a fulfilling area of research to be involved in and the experimental results presented here have produced a significant step in the search for ^{2}He emission. This has been the first time that sequential emission has been observed in an experiment which does not use β-decay to feed the resonance. In comparison to these experiments we have obtained a considerable increase in statistics (see section 1.2.2 and for example figure 1.5). This experiment is an excellent example of the new and interesting physics which can be explored using radioactive ion beams.

Appendix A

ECU technical details

The detailed schematic diagram in figure A.1 shows the ECU bottom board. There are 4 sets of 34-way inputs (A, B, C, D) which correspond to four LEDA sectors. A second board situated on top instruments the other four sectors with the two boards connected by a short 34-way cable. Input A corresponds to the 16 signals from a LEDA sector with channel 0 denoting the outermost strip and channel 15 the innermost. The diagram shows the paths that lead to the OR of the rings.

The inputs are the ECL logic outputs from the amplifiers and these are converted into a single logic pulse using MC10H115 quad receiver chips. All signals which correspond to a certain ring are OR'd and converted back into ECL logic using MC10H101P chips. A full component list is given in table A.1.

Power is supplied by standard CAMAC power supply consisting of 86 gold plated connectors which slot into the CAMAC crate. Schematic of the power supply circuit is shown in figure A.2. The board is earth referenced with connectors 43R and 43L and the chips are powered by -6V from the 38R line. For testing the boards separately the diode, IN4139, was kept in place in the power supply line. For full board operation under experimental conditions the diode was replaced by a wire in order to increase the chip operating voltage from -4.95 V to -5.4 V. Total

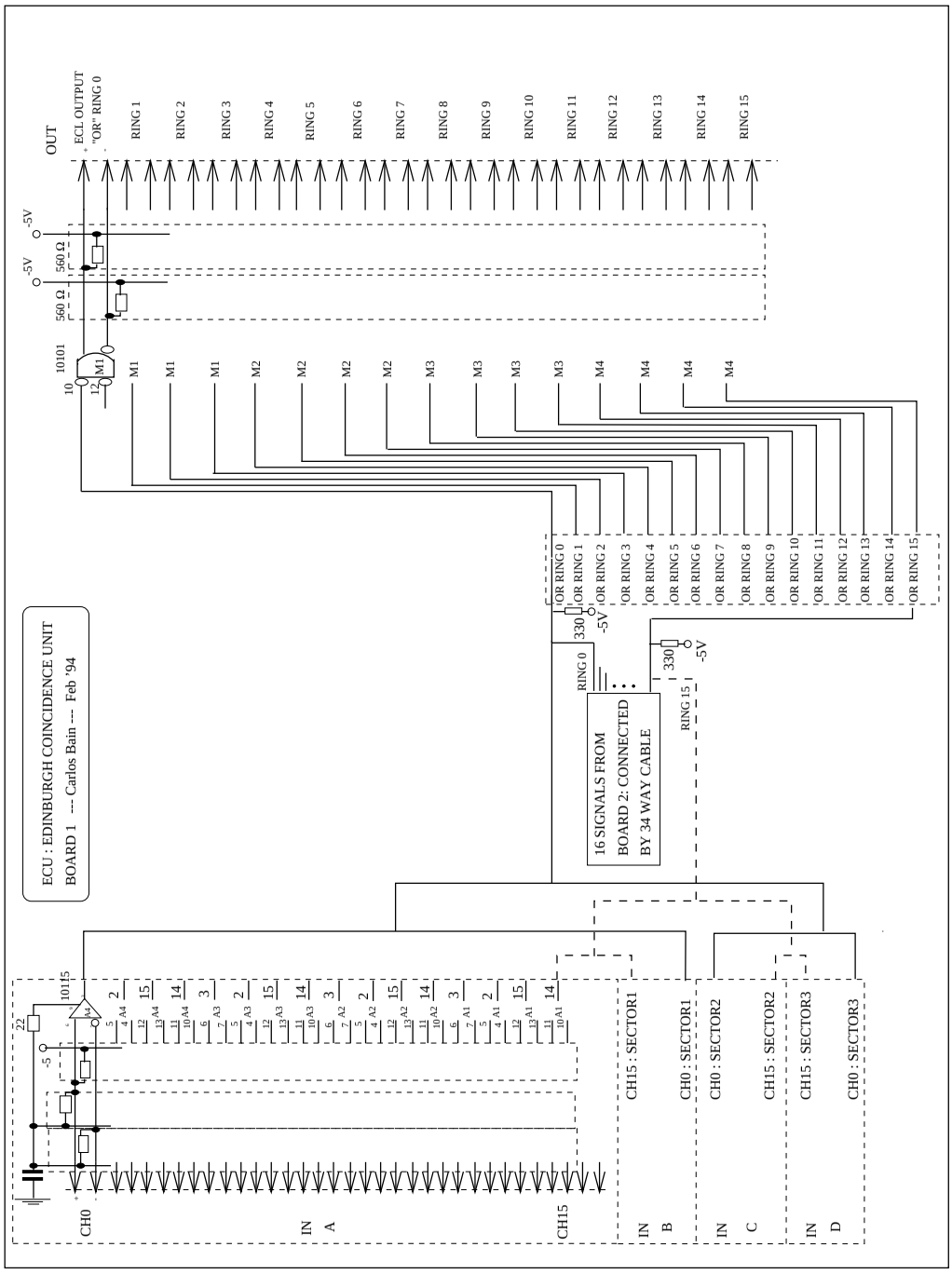

Figure A.1: *Full circuit diagram of the bottom board of the Edinburgh Coincidence Unit.*

current drawn by the ECU is 1.1A. A 3A fuse protects the module from power surges.

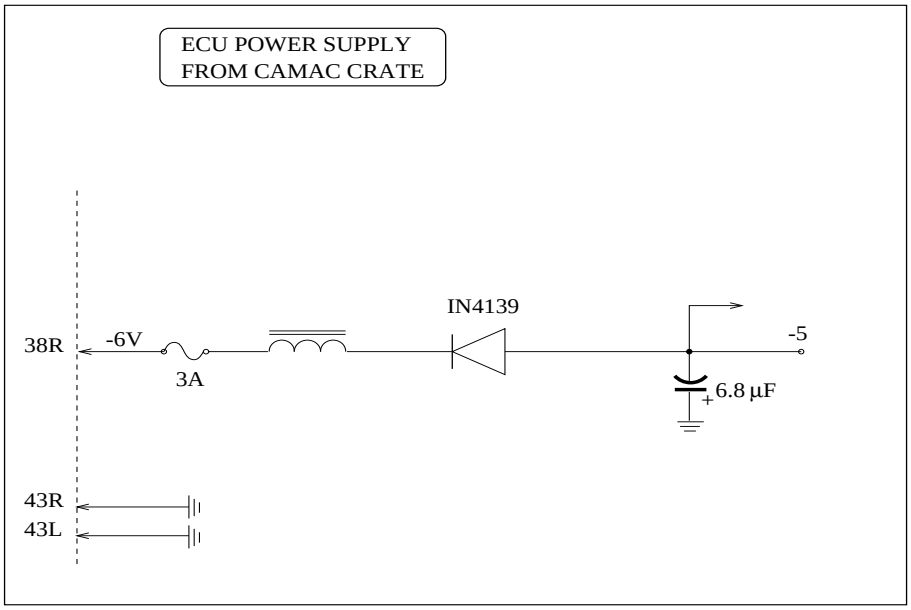

Figure A.2: *ECU power supply designed to be used in CAMAC crate. The 43 gold plated connectors on both sides of PCB are designated 'L' -left and 'R' - right. '43R' and '43L' are earth reference and '38R' provides the voltage for the chips.*

The MC10H115 quad differential amplifier (receiver) designed for use in sensing differential signals over long lines. An operating voltage of -5.2 V±5% is supplied to pin 9 as shown in figure A.3.

The MC10H101 is a quad input OR/NOR (driver). An operating voltage of -5.2 V±5% is supplied to pin 9 as shown in figure A.4 with one input from each gate common to pin 12.

In both chips pins denoted by V_{CC1} and V_{CC2} are earthed.

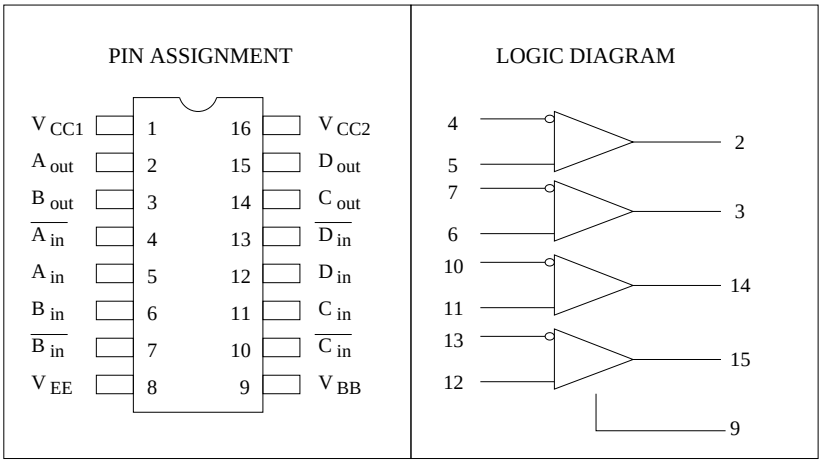

Figure A.3: *Pin assignment and logic diagrams for the Motorola MC10H115 chip.*

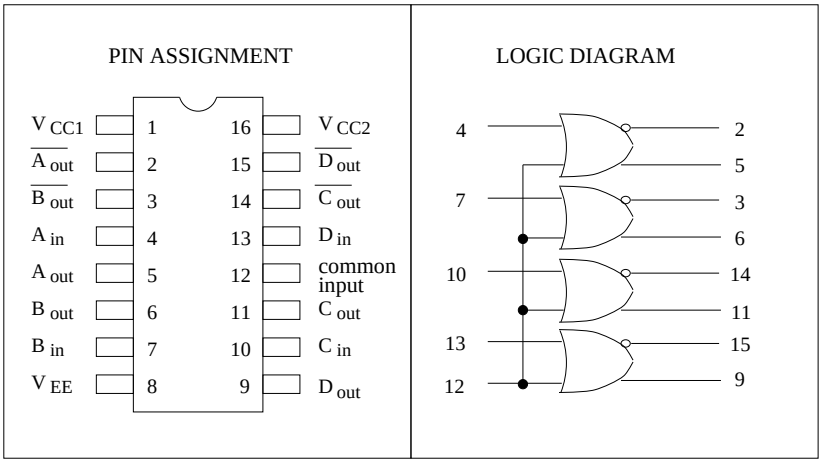

Figure A.4: *Pin assignment and logic diagrams for the Motorola MC10H101 chip.*

Part description	quantity
IC MC10H115PDL	32
IC MC10H101PDL	4
22 Ω resistors	16
330 Ω resistors	16
Resistor network 10pin 9 res 2.2kΩ	8
Resistor network 8pin 7 res 2.2kΩ	8
Resistor network 10pin 9 res 56Ω	16
Resistor network 8pin 7 res 56Ω	16
Resistor network 10pin 9 res 560Ω	2
Resistor network 8pin 7 res 560KΩ	2
Capacitors 50V 0.01μF	48
Capacitor tantilum 6.8μF	1
34-way right angle connectors	9
34-way right angle cased	2
3-amp fuse	1
IN5401 3A,100V diode rectifier	1
Inductor 4.7μH	1

Table A.1: *ECU component list.*

Appendix B

Target profiling

This appendix shows how inverse kinematics can be used to probe a target and extract its hydrogen profile. The technique has previously been used at Louvain-la-Neuve to study resonances in ^{20}Na by scattering radioactive ^{19}Ne beams off thick polyethene targets [Cos94].

The data taken during a LEDA test run prior to the follow-up run using the setup described in 3.4 is presented here. It has not been analysed rigorously but is meant to give an idea of the technique and the conclusions that can be drawn about the hydrogen content and distribution of a given target. The test run used a stable 20.5 MeV ^{19}F beam to bombard a number of targets and used the LEDA detector (LEDA 1 - see chapter 3) to record the events. An aluminium foil of 3.5mg/cm^2 thickness was placed midway between target and detector to reduce risk of radiation damage from the heavy ions.

The first part of this appendix looks at the profiles for different CH_2 targets. The second part describes the hydrogenation process and illustrates the target profiles obtained from the metal hydrides.

B.1 CH_2 targets

In inverse kinematics the heavy ion loses a considerable fraction of its initial energy in the $[CH_2]_n$. The protons recoiling into the forward hemisphere of the lab frame provide a precise probe of the hydrogen distribution in the target. Their low energy loss means that the information is not seriously distorted by straggling.

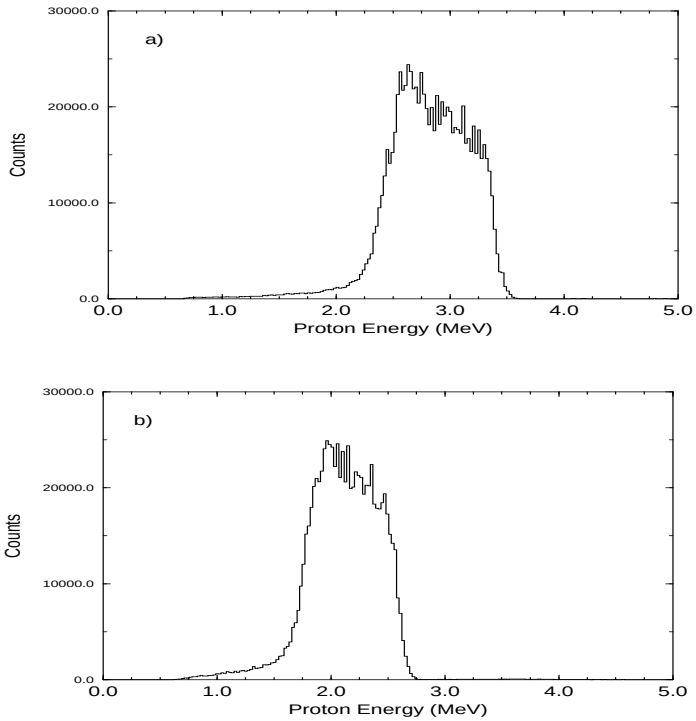

Figure B.1: *Figure shows scattered protons from a 420$\mu g/cm^2$ CH_2 target for sum of all strips at two angles. (a) is the sum of all strips at the inner most angle referred to as strip 15 and (b) the sum of all strips at the outer most angle referred to as strip 0.*

Figure B.1(a) and (b) show the spectra of the sum of all strips in innermost ring and in outermost ring respectively for a 420μgcm^2 CH_2 target. The high energy proton edge corresponds to protons scattered from the front end of the target when the beam has lost no energy and varies with angle as expected from elastic scattering. The low energy end corresponds to the second extreme were the ^{19}F beam loses a large fraction of its energy in the target and scatters with a proton towards the back end of the target.

In the experiment of Coszach *et al.* the energy calibration was based on the well known resonances in $^{19}F + p$ scattering [Cos94]. These resonances are at $E_{c.m.} =$ 637, 801, 829, and 888 keV with the first two being the strongest. The proton lab energy T_{proton} is given by

$$T_{proton} = E_{c.m.} \frac{4A}{A+1} \cos^2 \theta_{lab} \tag{B.1}$$

where A is the mass number of the beam.

For the 637 keV resonance the proton lab energy at the innermost angle is 2.290 MeV which becomes 1.898 MeV when energy loss through the foil is taken into account. The 801, 829, 888 keV would be seen at lab energies of 2.555, 2.664 and 2.893 MeV respectively. These energies have been highlighted in figure B.2a which shows the profile for a 830μg/cm^2 CH_2 target. It clearly shows that the two lowest have been populated with lower statistics for the other two.

The following spectra B.2(b)-(f) clearly show how the profile changes for different CH_2 target thicknesses. The resonant features disappear for thinner targets but the high energy proton edge remains. The CH_2 targets were made by P. Demaret at Universite Catholiqué Louvain (UCL) and are summarised in table B.1. The final spectra shown in figure B.2 is for a 375μg/cm^2 CD_2 target. It shows the deuteron group present at higher energies and the hydrogen group with approximately a quarter the number of counts.

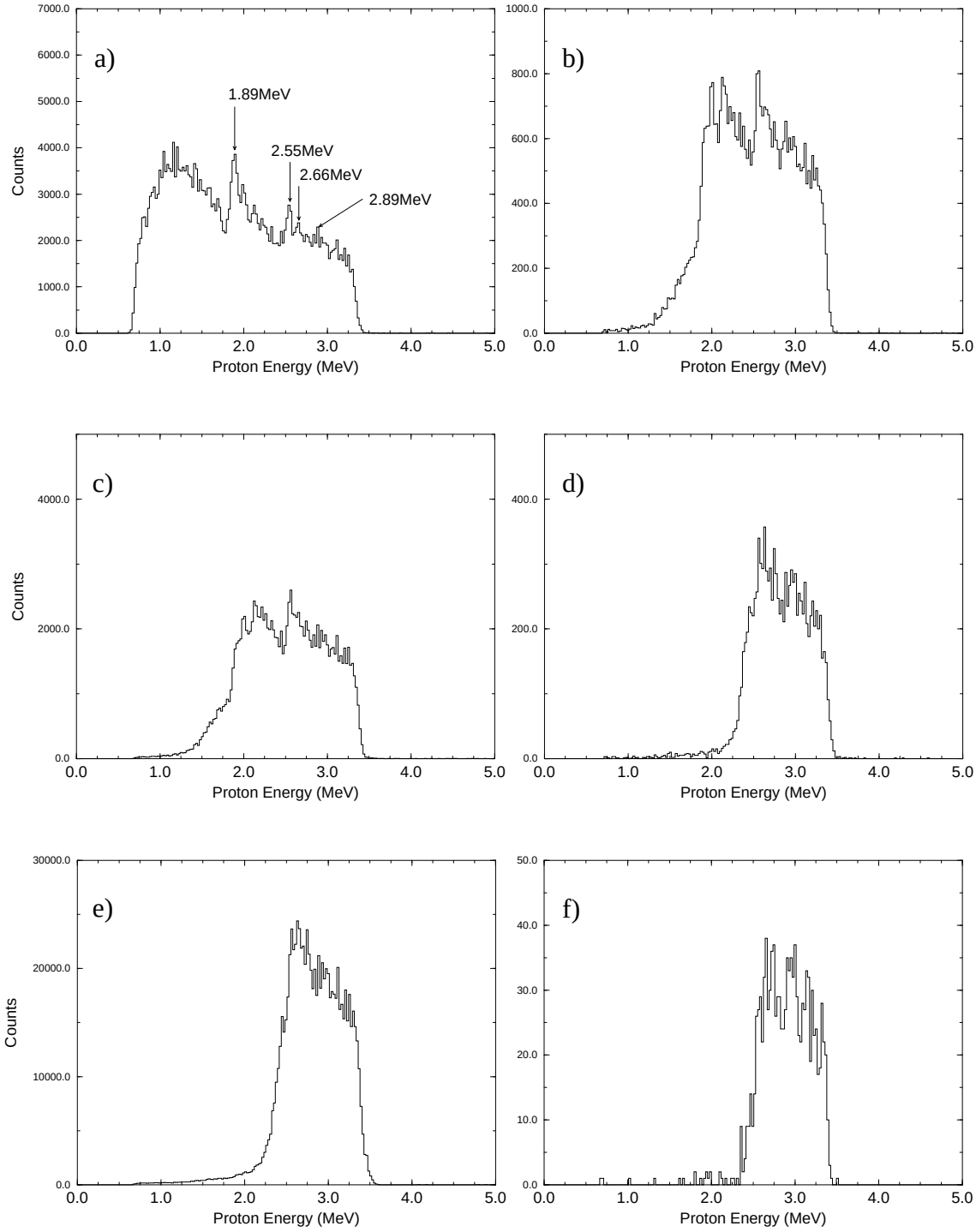

Figure B.2: *(a)-(f) Sum of ring 15 for for different CH_2 target thicknesses summarised in table B.1.*

CH_2 target thickness	Figure
$830\mu g/cm^2$	fig.B.2a
$660\mu g/cm^2$	fig.B.2b
$600\mu g/cm^2$	fig.B.2c
$500\mu g/cm^2$	fig.B.2d
$420\mu g/cm^2$	fig.B.2e
$300\mu g/cm^2$	fig.B.2f
CD_2 target thickness	Figure
$375\mu g/cm^2$	fig.B.3

Table B.1: *Table summarising CH_2 targets used in test run.*

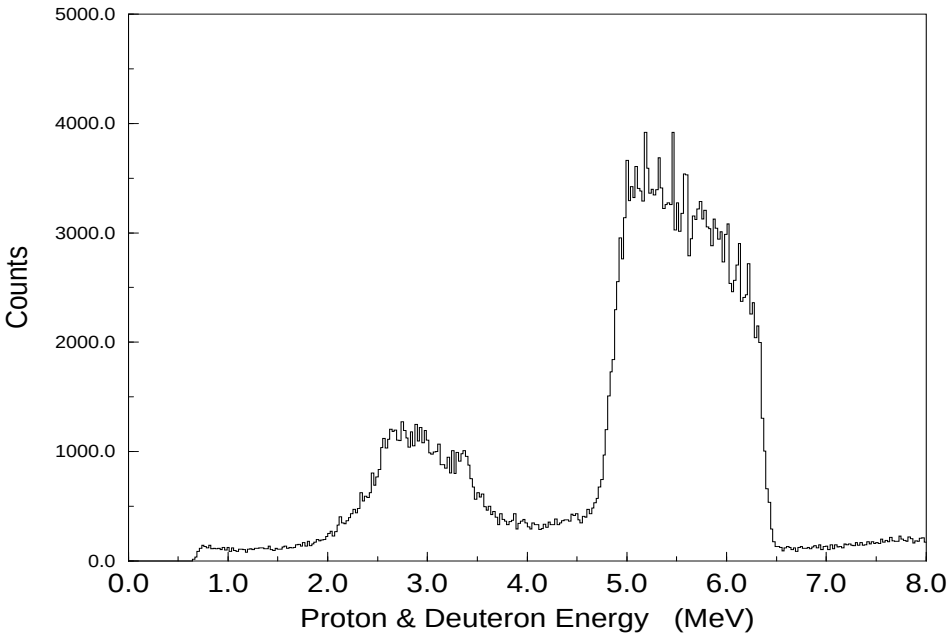

Figure B.3: *Sum of ring 15 for $375\mu g/cm^2$ CD_2 target.*

B.2 Hydrogenation Process

What follows is a brief description of the hydrogenation process used at Salford University.

The Salford Group use an Intelligent Gravimetric Analyser (IGA). This is made up of a main rig where the sample is held, a furnace, pumps and a personal computer which controls everything and displays temperature, pressure, mass changes etc. The sample is held in place on the end of a quartz hanger. For the IGA to work at its optimum the sample must be less than 0.5g in mass. The sample is carefully balanced by a counterweight which must be of a similar density to avoid errors due to buoyancy once that gas is pumped in. A display on the PC tells the operator when a satisfactory degree of accuracy has been obtained. The entire chamber is evacuated at first then gradually heated over several hours to around 800^{o}C. At this stage research grade hydrogen is slowly fed in at 1 atmosphere. As the sample takes in hydrogen its mass increases and tips the balance to one side. The shift of the balance is corrected by the computer and the mass increase is displayed on the screen. The mass increase will quickly reach a maximum and at that stage the furnace is removed and the tube holding the foil is immersed in liquid nitrogen. The metal to hydrogen ratio can be then be calculated from the change in target mass.

A total of 3 small TiH, 2 small ZrH, 1 large TiH and 1 large ZrH were made using titanium and zirconium foils purchased from Goodfellow [Goo]. Experimental difficulties meant that the hydrogen content was not known. This was due to the targets becoming very brittle, with slivers falling off during the process, which disrupted the delicate balance required for accurate measurement of mass changes [Poy94].

Results of the target profiling technique for the Salford metal hydrides are shown in figures B.4(a)-(f) and for a titanium hydride foil borrowed from the Birmingham

Nuclear Physics group in figure B.5. In all cases the sum of strips in the innermost ring is shown. The targets are summarised in table B.2 with a description of the corresponding spectrum.

Target	Figure	Description
Nat. titanium 1mg/cm^2 large	fig.B.4a	Two peaks correspond to hydrogen present on the surfaces - possibly water vapour
Nat. zirconium 1mg/cm^2 large	fig.B.4b	Single peak indicates hydrogen present on single surface - this may be a result of foil production
TiH † 1mg/cm^2 large	fig.B.4c	Good hydrogen distribution
TiH † 1mg/cm^2 small	fig.B.4d	Hydrogen concentrated in centre of target
ZrH † 1mg/cm^2 large	fig.B.4e	Reasonable distribution but high energy proton edge missing
ZrH † 1mg/cm^2 small	fig.B.4f	Very poor distribution
TiH $^\bullet$ 1mg/cm^2	fig.B.5	Good distribution, target looks thicker and resonant peaks can be seen

Table B.2: *Table summarising metal hydride targets used.*

† *Salford targets.*

$^\bullet$ *Birmingham target.*

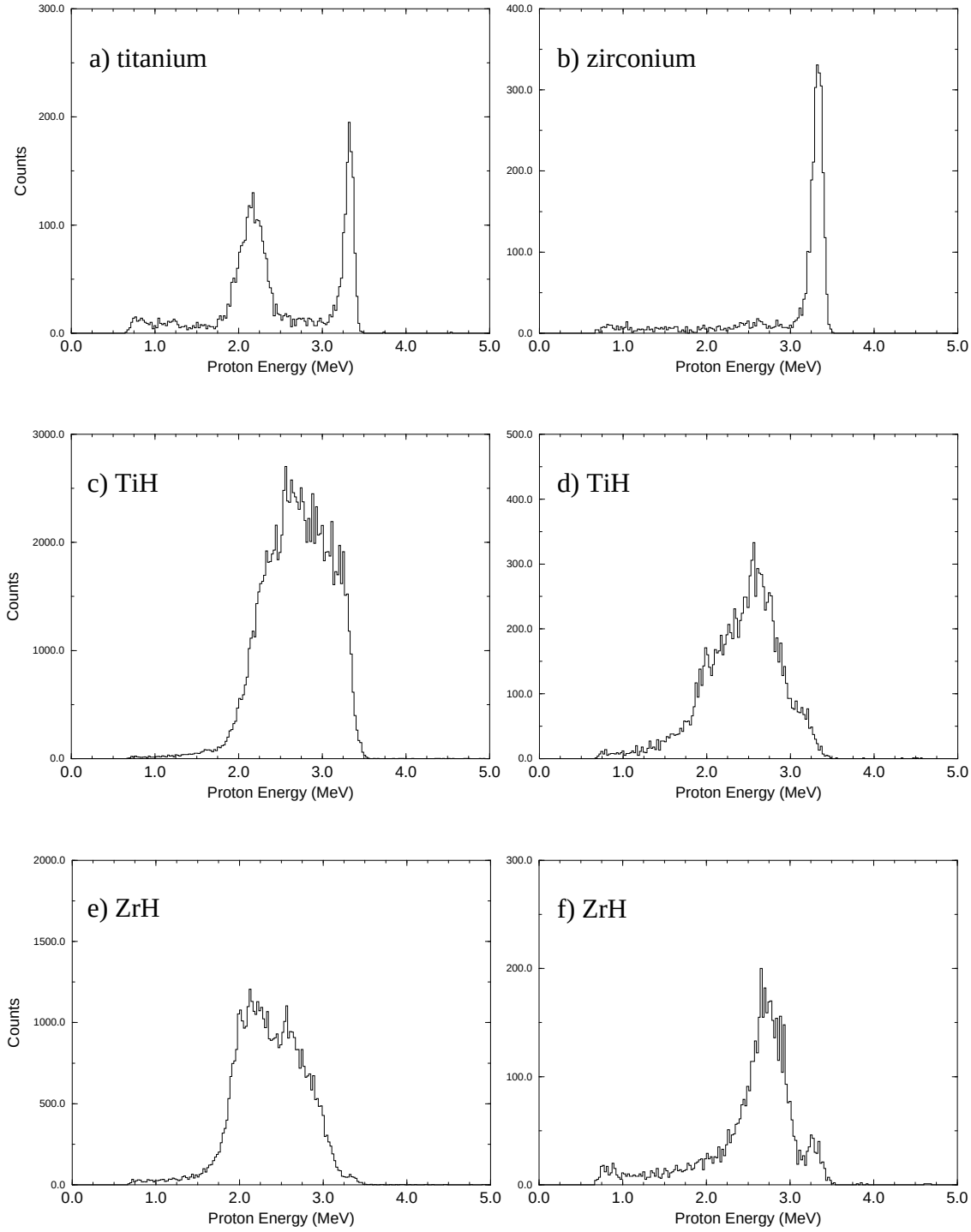

Figure B.4: *(a)-(f) Sum of ring 15 for for different metal targets summarised in table B.2.*

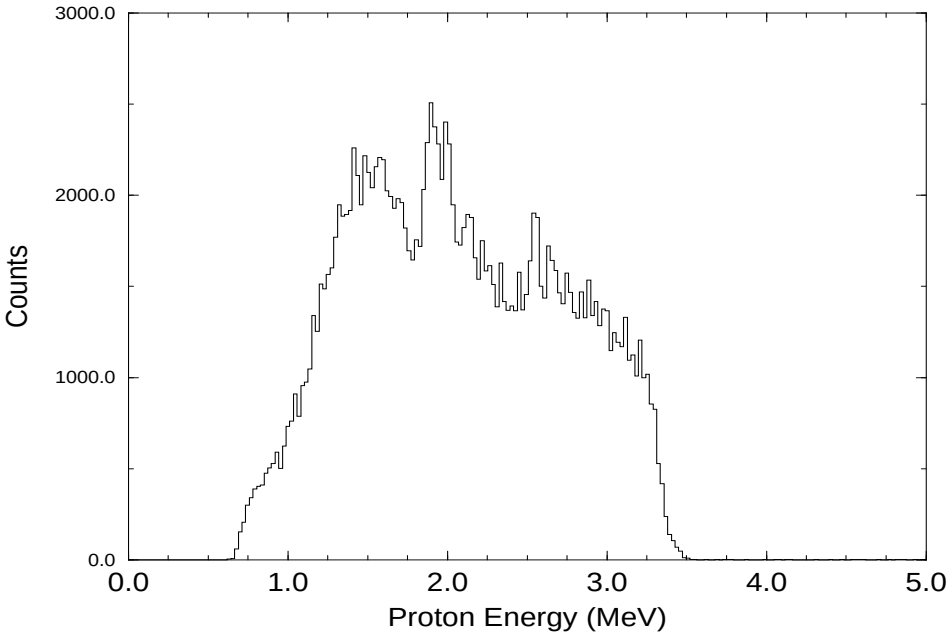

Figure B.5: *Small TiH target borrowed from Birmingham Nuclear Physics group.*

Bibliography

[Arm73] Armstrong and Chandler, *Oak Ridge National Laboratory* **4869** (1973).

[Ajz91] F. Ajzenberg-Selove, *Nucl. Phys.* **A523** (1991) 1.

[Äys85] J. Äystö, D.M. Moltz, X.J. Xu, J.E. Reiff and Joseph Cerny, *Phys. Rev. Lett.* **55** (1985) 1384.

[Bal67] G.C. Ball and J. Cerny, *Phys. Rev.* **155** (1967) 1170.

[Bal69] G.C. Ball and J. Cerny, *Phys. Rev.* **177** (1969) 1466.

[Bar] Roger Barlow *Statistics - A Guide to the Use of Statistical Methods in the Physical Sciences,* John Wiley & Sons.

[Baz92] D. Bazin, R. Anne, P. Bricault, C. Détraz, R. Del Moral, J.P. Dufour, A. Fleury, D. Guillemaud-Mueller, F. Hubert, J.C. Jacmart, M. Lewitowicz, A.C. Mueller, F. Pougheon, M.S. Pravikoff, A. Richard and Y. Zheng, *Phys. Rev.* **C45** (1992) 69.

[Bec90] F.D. Becchetti *et al.*, *Phys. Rev.* **C42** (1990) R801.

[Ber84] M.A. Bernstein, W.A. Friedman and W.G. Lynch, *Phys. Rev.* **C29** (1984) 132.

[Bie60] L.C. Bierdenharn, *Nuclear Spectroscopy Part B (Academic Press, New York, 1960)*

[Bim85] R. Bimbot *et al.*, *Z. Phys.* **A322** (1985) 443-456.

[Boc84] O.V. Bochkarev, A.A. Korsheninnikov, E.A. Kuz'min, I.G. Mukha, A. Oglobin, L.V. Chulkov and G.B. Yan'kov, *JETP Lett.* **40** (1984) 969.

[Boc87] O.V. Bochkarev *et al*, *Sov. J. Nucl. Phys.* **46** (1987) 7.

[Boc89] O.V. Bochkarev *et al*, *Nucl. Phys.* **A505** (1989) 215-240.

[Boc92] O.V. Bochkarev *et al*, *Sov. J. Nucl. Phys.* **55** (1992) 955.

[Bog90] M.J.G. Borge, H. Gabelmann, L. Johannsen, B. Jonson, G. Nyman, K. Riisager and O.Tengblad, *Nucl. Phys.* **A515** (1990) 21-30.

[Bor87] V. Borrel, J.C. Jacmart, F. Pougheon, A. Richard, R. Anne, D. Bazin, H. Delagrange, C. Détraz, D. Guillemaud-Muelleur, A.C. Mueller, E. Roeckl, M.G. Saint-Laurent, J.P. Dufour, F. Hubert and M.S. Pravikoff, *Nucl. Phys.* **A473** (1987) 331-341.

[Bor91] V. Borrel, R. Anne, D. Bazin, R. Del Moral, C. Détraz, J.P. Dufour, D. Guillemaud-Mueller, F. Hubert, J.C. Jacmart, A.C. Mueller, F. Pougheon, M.S. Pravikoff and E. Roeckl, *Nucl. Phys.* **A531** (1991) 353-369.

[Bor92] V. Borrel, R. Anne, D. Bazin, C. Borcea, G.G. Chubarian, R. Del Moral, C. Détraz, S. Dogny, J.P. Dufour, L. Faux, A. Fleury, L.K. Fifield, D. Guillemaud-Mueller, F. Hubert, E. Kashy, M. Lewitowicz, C. Marchand, A.C. Mueller, F. Pougheon, M.S. Pravikoff, M.G. Saint-Laurent and O. Sorlin, *Z. Phys* **A344** (1992) 135-144.

[Boy94] R.N. Boyd, *Int. Journal of Mod. Phys* **E3** (1994) 249-334.

[Bro91] B.Alex. Brown, *Phys. Rev.* **C43** (1991) R1513.

[Bro95] B.Alex. Brown, *Private Communication*

[Cab82] M.D. Cable, J. Honkanen, R.F. Parry, H.M. Thierens J.M. Wouters, Z.Y. Zhou and Joseph Cerny, *Phys. Rev.* **C26** (1982) 1778.

[Cab83] M.D. Cable, J. Honkanen, R.F. Parry, S.H. Zhou, Z.Y. Zhou and Joseph Cerny, *Phys. Lett.* **B123** (1983) 25.

[Cab83b] M.D. Cable, J. Honkanen, R.F. Parry, S.H. Zhou, Z.Y. Zhou and Joseph Cerny, *Phys. Rev. Lett.* **50** (1983) 404.

[Cab84] M.D. Cable, J. Honkanen, E.C. Schloemer, M. Ahmed, J.E. Reiff, Z.Y. Zhou and J. Cerny, *Phys. Rev.* **C30** (1984) 1276.

[Cog80] T.V. Congedo, I.S. lee-Fan and B.L. Cohen, *Phys. Rev.* **C22** (1980) 985.

[Con64] H.E. Conzett, E. Shield, R.J. Slobodrian, and S. Yamabe, *Phys. Rev. Lett.* **13** (1964) 625.

[Cos94] R. Coszach, C. Bain, F.C. Barker, D.Baye, F. Binon, T. Davinson, P. Decrock, Th. Delbar, P.Descouvemont, P. Duhamel, W. Galster, P. Leleux, I. Licot, E.Liénard, P. Lipnik, C. Michotte, M. Huyse, A. Ninane, R.D. Page, A.C. Shotter, P. Van Duppen, J. Vanhorenbeeck, M. Vincke, J. Vervier and P.J. Woods, *Phys. Rev.* **C50** (1994) 1695.

[Dan93] B.V. Danilin and M.V. Zhukov, *Phys. At. Nucl.* **56** (1993) 460.

[Dad95] C.N. Davids *et al.*, *Argonne National Laboratory,* PHY-8175-HI-95 (1995).

[Dar90] D. Darquennes *et al.*, *Phys. Rev.* **C42** (1990) R804.

[Dai73] J.C. Davis, J.D. Anderson, S.M. Grimes and C. Wong, *Phys. Rev.* **C8** (1973) 863.

[Dav90] T. Davinson, A.C. Shotter, E.W. Macdonald, S.V. Springham, P. Jobanputra, A.J. Stephens and S.L. Thomas, *Nucl. Instr. Meth. Phys. Res.* **A288** (1990) 245.

[Dec91] P. Decrock *et al.*, *Nucl. Instr. Meth. Phys. Res.* **B58** (1991) 252-259.

[Dec92] P. Decrock *et al.*, *Nucl. Instr. Meth. Phys. Res.* **B70** (1992) 182-185.

[Dec93] P. Decrock *et al.*, *Phys. Rev.* **C48** (1993) 2057.

[Dét89] C. Détraz and D.J. Vieira, *Ann. Rev. Nucl. Sc* **39** (1989) 407.

[Dét90] C. Détraz *et al.*, *Nucl. Phys.* **A519** (1990) 529-547.

[Dri80] J. van Driel, R. Kamermans, R.J. de Meijer and A.E.L. Dieperink, *Nucl. Phys.* **A342** (1980) 1-22.

[Fen78] D.H. Feng, K.N. Geller and N. Klein, *Phys. Rev.* **C18** (1978) 33.

[Gal95] Wilfried Galster, *Private Communication.*

[Gam28] G. Gamow, *Z. Phys.* **51** (1928) 204.

[Gee77] D.F. Geesaman, R.L. McGrath, P.M.S. Lesser, P.P. Urone, and B. Ver-West, *Phys. Rev.* **C15** (1977) 1835.

[Gil92] R.S. Gilmore, *Single Particle Detection and Measurement,* Taylor and Francis, London Washington 1992.

[Gol60] V.I. Goldansky, *Nucl. Phys.* **19** (1960) 482-495.

[Gol80] V.I. Goldansky, *JETP Lett.* **32** (1980) 554.

[Goo] GoodFellow Cambridge Limited, Cambridge CB4 4DJ, England.

[Hal94] G. Hall, *Rep. Prog. Phys.* **57** (1994) 481.

[Han89] P.G. Hansen and B. Jonson, *'Particle Emission from Nuclei',* Vol. III:157-201 Eds. M. Ivascu, D.N. Poenaru, CRC Press, Boca Raton, Florida USA (1989).

[Hof89] S. Hofmann, *'Particle Emission from Nuclei',* Vol. II:25-72, Eds. M. Ivascu, D.N. Poenaru, CRC Press, Boca Raton, Florida USA (1989).

[Hon83] J. Honkanen, M.D. Cable, R.F. Parry, S.H. Zhou, Z.Y. Zhou and Joseph Cerny, *Phys. Lett.* **B133** (1983) 146.

[Jac50] J.D. Jackson and J.M. Blatt, *Reviews of Mod. Phys* **22** (1950) 77.

[Jah78] R. Jahn, D.P. Stahel, G.J. Wozniak, R.J. de Meijer and Joseph Cerny, *Phys. Rev* **C18** (1978) 9.

[Jah85] R. Jahn, R.L. McGrath, D.M. Moltz, J.E. Reiff, X.J. Xu, J. Äystö and Joseph Cerny, *Phys. Rev.* **C31** (1985) 1576.

[Jän65] Joachim Jänecke, *Nucl. Phys.* **61** (1965) 326-341.

[Jon89] Y. Jonget *et al.*, *IEEE trans. Nucl. Sci.* **36** (1989) 1620.

[Kek78] G.J. KeKelis, M.S. Zisman, D.K. Scott, R. Jahn, D.J. Vieira, F. Ajzenberg-Selove and Joseph Cerny, *Phys. Rev.* **C17** (1978) 1929.

[Kel66] I. Kelson and G.T. Garvey, *Phys. Lett.* **23** (1966) 689.

[Kem80] J. Kemmer and R. Hofmann, *Nucl. Instr. Meth. Phys. Res.* **176** (1980) 543.

[Kry95] R.A. Kryger *et al.*, *Phys. Rev. Lett.* **74** (1995) 860.

[Kry95b] Robert Kryger, *Private Communication.*

[Lan58] A.M. Lane and R.G. Thomas, *Rev. Mod. Phys.* **30** (1958) 257.

[Liv93] K. Livingston, PhD thesis, University of Edinburgh, 1993.

[Mac] UNIMONTE : all purpose Monte Carlo break up code written by Euan MacDonald.

[Mfr60] M.H. Macfarlane and J.B. French, *Rev. Mod. Phys.* **32** (1960) 567.

[Mol89] D.M. Moltz and Joseph Cerny, *'Particle Emission from Nuclei'* Vol III, CRC Press (1989) 133.

[Mol92] D.M. Moltz, J.C. Batchelder, T.F. Lang, T.J. Ognibene, Joseph Cerny, P.E. Haustein, and P.L. Reeder, *Z. Phys.* **A342** (1992) 273-276.

[Mic] Micron Semiconductor Ltd, Lancing, England.

[Mig55] A.B. Migdal, *Sov. Phys. JETP.* **1** (1955) 2.

[Mue93] A.C. Mueller and B.M. Sherrill, *Annu. Rev. Nucl. Part. Sci* **43** (1993) 529-583.

[Naz95] W. Nazarewicz *et al.*, *Private Communication.*

[Nup93] Report by NuPECC Study Group, *European Radioactive Beam Facilities* 1993.

[Ohl65] G.G. Ohlsen, *Nucl. Inst. Meth. Phys. Res.* **37** (1965) 240-248

[Ohn93] H. Ohnuma *et al.*, *Phys. Rev* **C47** (1993) 648.

[Pag90] R.D. Page, PhD thesis, University of Birmingham, 1990.

[Pag94] R.D. Page, G. Vancraeynest, A.C. Shotter, M. Huyse, C. Bain, F. Binon, R. Coszach, T. Davinson, P. Decrock, Th. Delbar, P. Duhamel, M. Gaelens, W. Galster, P. Leleux, I. Licot, E. Lienhard, P. Lipnik, C. Michotte, A. Ninane, P.J. Sellin, Cs. Sükösd, P. Van Duppen, J. Vanhorenbeeck, J. Vervier, M. Wiescher and P.J. Woods, *Phys. Rev. Lett.* **73** (1994) 3066.

[Phi64] R.J.N. Phillips, *Nucl. Phys.* **53** (1964) 650-656.

[Php60] G.C. Phillips, T.A. Griffy and L.C. Biedenharn, *Nucl. Phys.* **21** (1960) 327-339.

[Poy94] Martin Poyser, *Private Communication.*

[Rei89] J.E. Reiff, M.A.C. Hotchkis, D.M. Moltz, T.F. Lang, J.D. Robertson and Joseph Cerny, *Nucl. Inst. Meth. Phys. Res.* **A276** (1989) 228-232.

[Rol88] Claus E. Rolfs and William S. Rodney, *'Cauldrons in the Cosmos',* University of Chicago Press 1988 Chicago and London

[Sat83] G.R. Satchler, *Direct Nuclear Reactions,* Clarendon Press 1983.

[Sat95] G.R. Satchler, *Private Communication.*

[Sel92] P.J. Sellin, PhD thesis, University of Edinburgh, 1992.

[Sie84] A.J. Sierk and A. Gavron, Los Alamos National Laboratory, Group T-9, *pace2 - projection angular-momentum coupled evaporation*

[Slo68] R.J. Slobodrian, H.E. Conzett and F.G. Resmini, *Phys. Lett.* **B27** (1968) 405.

[Sta79] D.P. Stahel, R. Jahn, G.J. Wozniak and Joseph Cerny, *Phys. Rev.* **C20** (1979) 1680.

[Sto95] Irena Stone, *Private Communication.*

[Str90] D.W. Stracener *et al.*, *Nucl. Instr. Meth. Phys. Res.* **A294** (1990) 485.

[The95] M. Thoennessen *et al*, *Invited Talk Presented at the International Conference on Exotic Nuclei and Atomic Masses,* Arles, France, June 1995.

[Tho90] S.L. Thomas, T. Davinson and A.C. Shotter, *Nucl. Instr. Meth. Phys. Res.* **A288** (1990) 212.

[Thp95] Ian Thompson, *Private Communication.*

[Wap85] Wapstra *et al.*, *Nucl. Phys.* **A432** (1985) 1.

[Wat52] K.M. Watson, *Phys. Rev* **88** (1952) 1163.

[Woo93] P.J. Woods *et al.*, Proposal for experiment at CYCLONE, *'A Search for 2p Emission from* ^{14}O*'*

[Woo94] P.J. Woods *et al.*, Proposal for experiment at CYCLONE, *'The Mechanism for 2p Emission from* ^{14}O*'*

[Woo94b] P.J. Woods *et al.*, Proposal for experiment at CYCLONE, *'Two nucleon transfer to the proton halo nucleus in* ^{17}Ne*'*

[Zot] Zot Engineering Ltd., Inveresk Industrial Estate, Musselburgh, East Lothian.